Title

Total-Body PET Kinetic Modeling and Parametric Imaging with Applications to Lung Disease and Beyond

Author

Wang, Yiran

Publication Date

2023

Total-Body PET Kinetic Modeling and Parametric Imaging with Applications to Lung Disease and Beyond

By

YIRAN WANG
DISSERTATION

Submitted in partial satisfaction of the requirements for the degree of

DOCTOR OF PHILOSOPHY

in

Biomedical Engineering

in the

OFFICE OF GRADUATE STUDIES

of the

UNIVERSITY OF CALIFORNIA

DAVIS

Approved:

Guobao Wang, Chair

Simon R. Cherry

Jinyi Qi

Committee in Charge

2023

Abstract

Dynamic positron emission tomography (PET) imaging captures a series of PET images over time and monitors the spatiotemporal distribution of the radiotracer administered to the body. Tracer kinetic modeling and parametric imaging (i.e., voxel-wise kinetic modeling) are a technique for dynamic PET imaging. It enables the quantification of kinetic parameters via the mathematical modeling of the time-varying tracer distribution. The quantified parameters represent the tracer kinetics and can potentially serve as biomarkers for various diseases. However, the development and application of kinetic modeling are largely limited by the short axial field-of-view (AFOV) (15-30 cm) of conventional PET scanners. This short AFOV not only restricts the anatomical coverage of the body but also confines the temporal resolution of dynamic scans to typically 10-40s/frame due to the low detection sensitivity.

The introduction of total-body PET systems, such as the 194-cm long uEXPLORER, enables the total-body field of view and significantly increases the detection sensitivity. Propelled by these advancements, we developed kinetic modeling with total-body PET in multiple aspects, emphasizing applications to lung disease but also broadly encompassing systemic disease. First, we investigated the high temporal resolution (HTR) kinetic modeling by leveraging HTR dynamic imaging (e.g., 1s/frame) with the total-body PET scanner. Second, multi-organ kinetic modeling was studied, taking advantage of the simultaneous imaging of the entire body. Third, deep learning was explored to pursue efficient approaches for total-body parametric imaging.

The investigation of HTR kinetic modeling in this study focuses on the lung, an organ unique for its dual blood supplies from the right ventricle and the left ventricle. The HTR dynamic imaging enables the capture of the rapid-changing early kinetics of the lung and its two blood supplies. However, existing kinetic models are insufficient for modeling the acquired HTR data. Hence, we first studied necessary corrections to the right ventricle input function, which is the dominant blood supply to the normal lung tissue. Corrections of time delay and dispersion were demonstrated to largely improve model fitting and impact the lung kinetic parameter quantification, leading to more reasonable estimates of fractional blood volume v_{b} (~0.14) and the detected aging effect of v_{b}, both within physiological expectations. Second, considering that lung tumors can have altered blood supplies compared with normal lung tissue, we proposed the dual-blood input function (DBIF) for lung kinetic modeling. The DBIF further improved the fitting quality, especially for lung tumors. In addition, the left ventricle supply fraction f that is uniquely quantified by the DBIF model was significantly higher in lung tumors (~0.3) than in normal lung tissue (~0.04).

Besides the HTR, total-body dynamic PET also permits the kinetic quantification of multiple organs and multiple parameters, which is promising for the evaluation of systemic diseases. In this work, we applied multi-organ kinetic modeling to evaluate metabolic changes in coronavirus disease 2019 (COVID-19) recovery. A higher lung ^{18}F-fluorodeoxyglucose (FDG) net influx rate K_{i} and a higher bone marrow FDG delivery K_1 were detected in recovering COVID-19 subjects compared to healthy subjects with statistical significance. These multiparametric findings may be associated with continued

inflammation during the COVID-19 recovery and will be otherwise missed if only assessed with the standardized uptake value (SUV) using whole-body static PET imaging.

While conventional kinetic modeling methods can be time-consuming for total-body parametric imaging owing to the large data amount to process, deep learning is promising for providing more efficient approaches. Hence, our study investigated the application of deep learning for total-body parametric imaging. The first study focused on total-body kinetic model selection, which aims to identify the appropriate kinetic model for body voxels and suppress artifacts in parametric images. We proposed a single-subject deep learning strategy to avoid the need for a population database for model training, and our preliminary tests showed the proposed method achieved better efficiency than the commonly used model selection method. In the second study, we explored deep learning for total-body voxel-wise parameter quantification. We proposed the Deep Patlak, a deep neural network method for the estimation of net influx rate K_i with its architectural design inspired by the conventional Patlak plot. The proposed Deep Patlak decreased the time cost for total-body parametric imaging of K_i than the conventional model-fitting-based method, while it is also more interpretable as compared to alternative neural network models. The parametric image by Deep Patlak showed good potential in imaging lung metastases.

In summary, this dissertation investigated tracer kinetic modeling and parametric imaging with total-body PET and its applications to lung disease and beyond from different angles, including high temporal resolution kinetic modeling, multi-organ kinetic modeling, and deep learning for total-body parametric imaging. We demonstrated the feasibility of high temporal resolution kinetic modeling and the potential for disease evaluation utilizing

the rapid-changing early kinetics. The multi-organ kinetic modeling enables a multiparametric quantification and assessment of the tracer kinetics in the entire body. The deep learning studies contribute to enhancing the effectiveness and efficiency of total-body parametric imaging. Our investigations highlight the combination of tracer kinetic modeling and total-body dynamic PET imaging in various contexts, demonstrating it as a sensitive tool to evaluate the human body, in both health and disease.

Acknowledgments

I sincerely appreciate my graduate advisors Prof. Guobao Wang and Prof. Simon R. Cherry. Thanks to their advice, help, and encouragement during the years. I have learned a lot from them.

I acknowledge Prof. Jinyi Qi, Prof. Ramsey D. Badawi, Prof. Audrey P. Fan, Prof. Terry Jones, Prof. Lorenzo Nardo, and Prof. Abhijit J. Chaudhari for their advice.

Thanks to Dr. Benjamin A. Spencer, Dr. Yasser J. Abdelhafez, Dr. Elizabeth J. Li, Dr. Siqi Li, Dr. Yansong Zhu, Dr. Yang Zuo, and Dr. Negar Omidvari for their help, as well as to other members in the MIPET/PEMI group and the EMIC group.

Thanks to my family for supporting me, and thanks to Jun.

Table of Contents

Acronym List

Acronym	Definition	Acronym	Definition
^{18}F-FDG, or FDG	^{18}F-fluorodeoxyglucose	HTR	High-temporal resolution
^{18}F-FDG-6P, or FDG-6P	^{18}F-fluorodeoxyglucose-6-phosphate	IDIF	Image-derived input function
1T	One-tissue compartmental model	LLM	Large language model
2T	Two-tissue compartmental model	LOR	Line of response
2Ti	Two-tissue irreversible compartmental model	LTR	Low temporal resolution
3D	Three-dimensional	LV	Left ventricle
4D	Four-dimensional	LVIF	Left ventricle input function
AFOV	Axial field of view	MIP	Maximum intensity projection
AI	Artificial intelligence	MRI	Magnetic resonance imaging
AIC	Akaike information criterion	OSEM	Ordered subset expectation maximization
BMI	Body mass index	PBIF	Population-based input function
BN	Batch-normalization	PBPK	Physiologically based pharmacokinetic
CM	Compartmental modeling	PET	Positron emission tomography
CNN	Convolutional neural network	PMT	Photomultiplier tube
COVID-19	Coronavirus disease 2019	RMSE	Root mean squared error
CT	Computed tomography	ROI	Region of interest
DBIF	Dual-blood input function	RV	Right ventricle
DL	Deep learning	RVIF	Right ventricle input function
DP	Deep Patlak	SiPM	Silicon photomultiplier
uEXPLORER	uEXPLORER total-body PET/CT system	SUV	Standardized uptake value
FOV	Field of view	SUVR	Standardized uptake value ratio
GLUT	Glucose transporter	TAC	Time-activity curve
GPT	Generative pre-trained transformer	TOF	Time of flight
GPU	Graphics processing unit	WRSS	Weighted residual sum of squares

Chapter 1. Introduction

1.1. Purpose of Positron Emission Tomography Imaging

Positron emission tomography (PET) imaging is a nuclear imaging technology (*1*) that involves the administration of a small amount of radiolabeled pharmaceutical (also referred to as a tracer) to human or animal bodies and the monitoring of the tracer distribution with a PET scanner. Driven by biochemical properties, a tracer can transport, bind, or metabolize in the body, and its fate can vary with different health conditions (*2*). The isotope labeling the tracer undergoes radioactive decay and leads to the emission of annihilation photons (*3*), which can be captured by the PET scanner (*4*). Combined with image reconstruction (*5*), the biodistribution of the tracer can be recovered from the PET-recorded data. Consequently, PET imaging evaluates physiological and pathological information and is an effective tool for a spectrum of applications, including diagnosis (e.g., (*6*,*7*)), prognosis (e.g., (*8*,*9*)), treatment planning (e.g., (*10*,*11*)), and treatment monitoring (e.g., (*12*,*13*)).

PET imaging stands out among various imaging approaches for its unique advantages. It provides a noninvasive and *in vivo* method to assess health and disease compared with those more invasive ones, such as endoscopy (*14*,*15*) and histopathology (*16–18*). The high sensitivity and specificity (*19*) of PET imaging further contribute to its significance in the realm of medical imaging. Over decades, numerous tracers have been carefully designed to reflect specific types of biochemical processes, creating high-sensitivity probes for the examination of molecular-level changes in the body (*20*). Hence, PET imaging is also referred to as a functional imaging method (*21*,*22*), in contrast with structural imaging approaches that mainly reflect anatomical information, such as magnetic resonance imaging (MRI), computed tomography (CT), or ultrasound imaging. Due to the potential of molecular changes to occur earlier than observable structural changes, PET also shows noticeable benefits in the detection and characterization of diseases at their early stages (*23*,*24*). Propelled by these advantages, PET imaging has extensive applications in oncology (*24*), cardiology (*25*), and neurology (*26*).

1.2. Principle of PET Physics

A PET tracer is usually a molecule labeled with an isotope with β+ decay (*3*). For example, the tracer ^{18}F-fluorodeoxyglucose (also noted as ^{18}F-FDG or FDG) is an analog molecule of glucose with one hydroxyl group (-OH) substituted by an ^{18}F isotope atom (*27*). The β+ decay is a type of nuclear decay during which a positron, the anti-matter of an electron, is emitted from the nucleus. As an example, the decay of ^{18}F by β+ emission can be described as:

$$^{18}\mathrm{F} \rightarrow {}^{18}\mathrm{O} + \mathrm{e}^{+} + \nu_{\mathrm{e}}, \qquad \text{Eq. 1.1}$$

in which e^{+} represents the positron, and ν_{e} denotes the electron neutrino that is also emitted in the β+ decay. The β+ decay follows an exponential formula (*28*). For a certain amount of isotope with the initial activity of A_0,

$$A(t) = A_0 \exp(-\lambda t), \qquad \text{Eq. 1.2}$$

in which t is the elapsed time from the initial time, $A(t)$ is the activity at time t, $\lambda = \ln(2)/T_{1/2}$ is the decay constant, and $T_{1/2}$ is the half-life. For ^{18}F, $T_{1/2} = 109.8$ min.

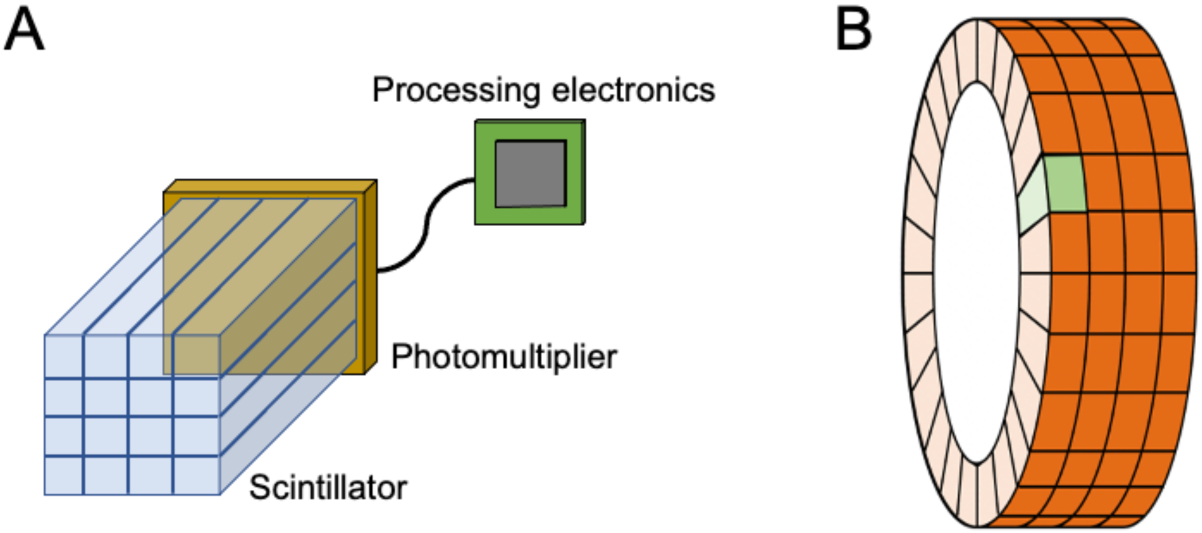

Figure 1.1. A. Components of a PET detector. B. The cylindrical alignment of PET detector modules. One detector module among them is colored green.

The emitted positron by the β+ decay travels a short distance (for example, typically <1mm for ^{18}F in soft tissue (*1*)) and then undergoes annihilation with an electron in the tissue (*3*). Consequently, a pair of annihilation photons are emitted simultaneously and travel in opposite directions, each with an energy of 511 keV. The overall direction of the annihilation pair emission has an isotropic probability distribution in the 3D space.

The PET imaging system, or PET scanner, is designed to detect the annihilation photon pairs to image the tracer biodistribution. The fundamental element of a PET scanner is the scintillation detector, which is composed of scintillators, photomultipliers, and processing electronics (Figure 1.1A) (*29*,*30*). Scintillators can capture gamma photons and are commonly made of bismuth germanate (BGO) (*31*), lutetium oxyorthosilicate (LSO) (*32*), or lutetium-yttrium oxyorthosilicate (LYSO) (*33*). The captured gamma photon

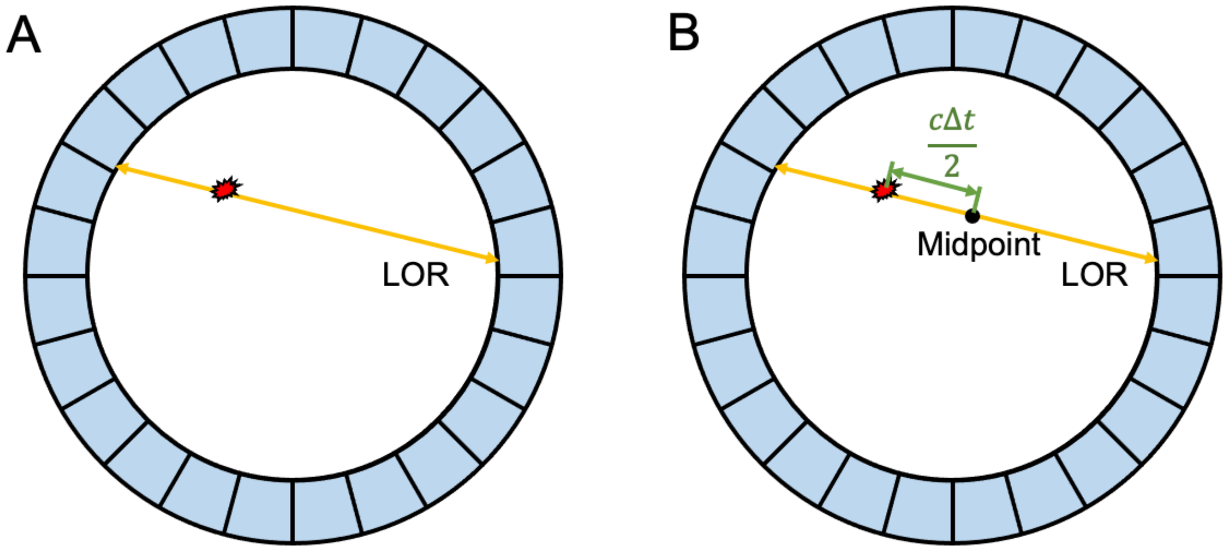

Figure 1.2. A. The detection of the emitted gamma photon pair and the created line of response (LOR). B The time-of-flight (TOF) technology helps to further locate the annihilation site: the distance from the midpoint of the LOR to the annihilation site is $\frac{c\Delta t}{2}$.

deposits energy in the scintillator and generates visible light (*34*), mainly through the photoelectric effect (*35*) or the Compton scatter effect (*36*). The visible photons then travel to the scintillator-coupled photomultiplier, usually a photomultiplier tube (PMT) or a silicon photomultiplier (SiPM) (*37*). The photomultiplier converts the visible light into electric signals, which are then sent to electronics (*30*) for subsequent processing and recording.

In a PET scanner, numerous detector modules described above are usually arranged in a cylindrical arrangement (Figure 1.1B) and work cohesively to localize the site of annihilation photon emission. When a pair of annihilation photons emitted by an annihilation reaches a pair of detectors, their arrival times are fairly close (usually 6-12 nanoseconds) (*1*) and can be recorded as a coincident pair by the processing electronics.

The recorded information is commonly referred to as list-mode data *(38)* and contains the detection site, detection time, and energy deposition of the annihilation photon pairs. With the detection sites of the photons, a line of response (LOR) *(39)* is created between the detection sites of the photons, which represents the possible photon annihilation site (Figure 1.2A). Further, as the pair of photons arrive at detectors at different times, time-of-flight (TOF) differences can be utilized to approximately locate the emission site on the LOR *(40)*. Suppose the detection time difference between the two photons is Δt; then, the distance between the emission site and the middle point of LOR is

$$\Delta x = \frac{c\Delta t}{2}, \qquad \text{Eq. 1.3}$$

in which $c = 3 \times 10^8 \mathrm{m/s}$ is the light speed, and the emission site is closer to the first detected photon of the pair (Figure 1.2B).

Based on the detection principle of the annihilation photon pair, it is evident that the field of view (FOV) of a PET scanner is the cylindrical space within the cylindrical arrangement of the detectors (Figure 1.3A). In addition, the axial field of view (AFOV) of a PET scanner is limited by the physical dimension of the detector arrangement in the axial direction. Annihilation sites within the FOV of the PET scanner can be detected, while those outside the FOV cannot, as shown by the illustrative examples in Figure 1.3B. It is also worth mentioning that only a portion of photon pairs emitted from the annihilation site can be detected. That is because the emission is isotropic, and only the annihilation pairs

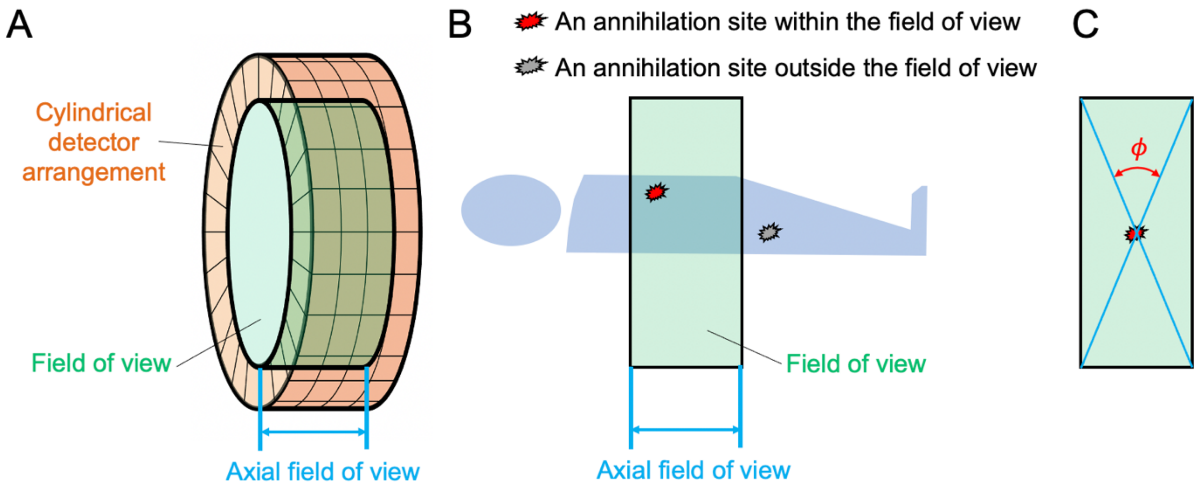

Figure 1.3. A. Illustration of the cylindrical detector arrangement (orange), field of view (FOV) (green), and axial field of view (AFOV) (blue) of a PET scanner. B. Illustrative examples of an annihilation site within the FOV and an annihilation site outside the FOV. C. For the annihilation site at the center of the cylindrical FOV, only annihilation pairs emitted within the angle ϕ can be detected.

emitted with directions within the geometrical coverage of the detector array can be captured. One example of this principle is shown in Figure 1.3C.

With the PET data acquired, the PET images can be reconstructed using image reconstruction algorithms. Common algorithms include analytical methods, e.g., the filtered back projection algorithm (*41*), and iterative methods, e.g., the maximum-likelihood expectation-maximization algorithm (*42*) and its variants (*43*).

1.3. PET Tracers and the Measurement of Tracer Biodistribution

The purpose of a PET tracer is to evaluate one or several specific physiological or biological processes. For example, among the numerous tracers developed over decades, the most widely used tracer in clinical practice is ^{18}F-FDG (*44*). ^{18}F-FDG is an analog of glucose, and its uptake reflects glucose metabolism in tissues (*1*). According to the

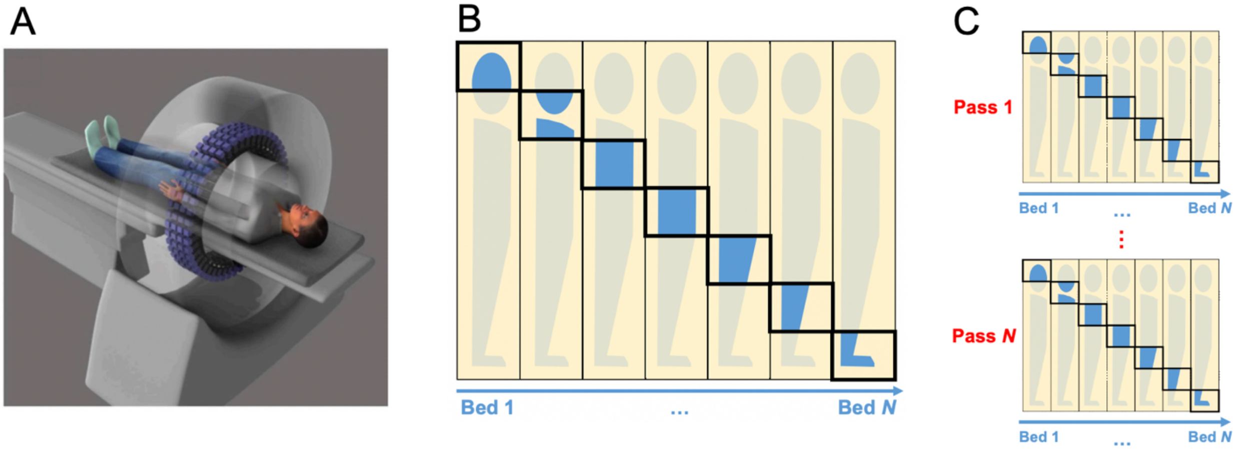

Figure 1.4. A. A conventional PET scanner commonly has an axial field of view of 15-30 cm and can only acquire a small fraction of the body each time. The scan of multiple bed positions is required for a static whole-body PET with this scanner (B), and multiple passes of multiple bed positions are further needed for a dynamic whole-body PET scan (C). Figure A courtesy of Dr. Simon R. Cherry.

Warburg hypothesis *(45)*, most types of cancer cells utilize glucose in an inefficient way, resulting in elevated glucose metabolism *(46)*. Hence, these cancer cells also uptake more ^{18}F-FDG than the surrounding normal tissue, leading to a contrast in the ^{18}F-FDG-PET image. In addition to oncology, ^{18}F-FDG has also been studied to assess various diseases, such as Alzheimer's disease *(7,47)*, cardiac diseases *(48,49)*, infectious diseases *(50)* and arthritis *(51)*, hypothesizing that these diseases may also influence glucose metabolism.

The administration of the PET tracer to the subject is usually through intravenous injection. To record the distribution of the administered tracer, there are broadly two scan strategies: static *(52)* and dynamic *(53)*. A static scan is designated to image the tracer distribution at a specific time. For instance, a subject can be scanned 50-60 min after the ^{18}F-FDG injection *(54,55)*. The specific timing is chosen as the ^{18}F-FDG distribution during this period can reflect the glucose metabolism well and offer crucial information for disease detection and characterization. As the AFOV of a conventional scanner is 15-30 cm (Figure 1.4A), the scanner can only image a small fraction of the body at a certain time. To acquire a whole-body static image, the scan bed needs to move across multiple bed positions (Figure 1.4B) (*52*).

In contrast with static imaging, dynamic imaging aims to acquire the spatiotemporal distribution of the tracer. It usually starts right before the tracer injection and extends over a period, e.g., 60 min. During the dynamic scan, the AFOV of the scanner can fix on one bed position to study a specific organ (e.g., (*56,57*)). However, to collect the dynamic data of the entire body, the scan bed has to move for multiple passes of multiple positions during the scan period (Figure 1.4C) (*58,59*).

The acquired data from a static scan can be reconstructed into a 3D image, while data from a dynamic scan are usually reconstructed into a series of 3D images with different time points, i.e., a spatiotemporal 4D image (*53*). The unit of the original image is commonly Bq/mL, representing the tracer activity per volume. With the aim of a better indication of the physiological condition, the image is usually converted into the standardized uptake value (SUV) (*60*):

$$\mathrm{SUV}\ [\mathrm{g/mL}] = \frac{\text{Activity concentration [Bq/mL]}}{\text{Administered dose [Bq]/Subject body mass [g]}}. \qquad \text{Eq. 1.4}$$

SUV can be deemed a normalization over the administered dose and subject weight, and the mean value of SUV is ~1 in the entire body by definition. SUV facilitates the comparison of tracer concentration both within the same subject and between different subjects and is widely used in the clinical practice of PET. Despite its utility, SUV is a

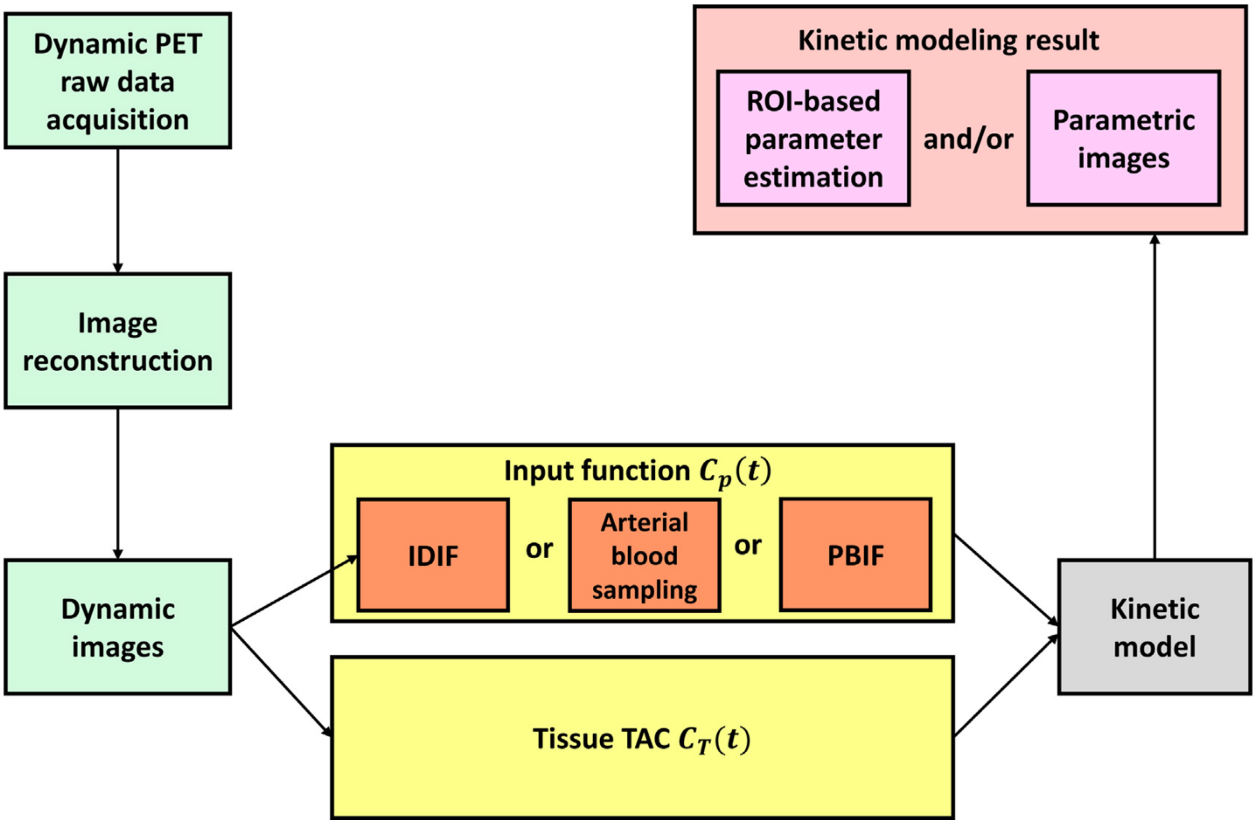

Figure 1.5. Flowchart of PET kinetic modeling.

semi-quantitative measurement and can be affected by various confounding factors (*61*). One mitigation is to further convert SUV values into standardized uptake value ratio (SUVR),

$$\mathrm{SUVR} = \frac{\text{SUV of the region of interest}}{\text{SUV of the reference region}}; \qquad \text{Eq. 1.5}$$

Previous studies have indicated that SUVR can be a better metric of tracer metabolism than SUV (*62*). However, SUV and SUVR are still semi-quantitative metrics and have limited ability to describe the tracer kinetics, with their values also being dependent on the time of measurement (*61,63–65*).

1.4. Tracer Kinetic Modeling

Tracer kinetic modeling is a technique for dynamic PET (*2*,*53*). It models the temporal changes of tracer concentration and aims to quantify parameters that reflect the physiological conditions and can potentially serve as biomarkers for disease evaluation. The flowchart of kinetic modeling is shown in Figure 1.5. First, the dynamic image is obtained from the dynamic scan and image reconstruction. Then, the time-activity curve (TAC) of a tissue region of interest (ROI), noted as $C_{\mathrm{T}}(t)$, is extracted from the dynamic image. Meanwhile, the blood input function $C_{\mathrm{p}}(t)$ can be acquired by the TAC extraction from a blood pool (such as the left ventricle or aorta) in the dynamic image. The input function obtained in this manner is referred to as the image-derived input function (IDIF) (*66*). Corrections, such as the metabolite correction (*67*,*68*) and the time delay correction (*69*)), may be applied to the IDIF. Alternatively, $C_{\mathrm{p}}(t)$ can be measured with arterial blood sampling (*70*) or obtained through a population-based input function (PBIF) (*71*). $C_{\mathrm{T}}(t)$ and $C_{\mathrm{p}}(t)$ are then sent to the kinetic model to estimate the kinetic parameters of the ROI. Kinetic modeling can also be performed on a voxel-by-voxel basis (i.e., with $C_{\mathrm{p}}(t)$ and the voxel $C_{\mathrm{T}}(t)$) to get the parametric image, in which the voxel values represent the calculated kinetic parameter (*2*,*38*).

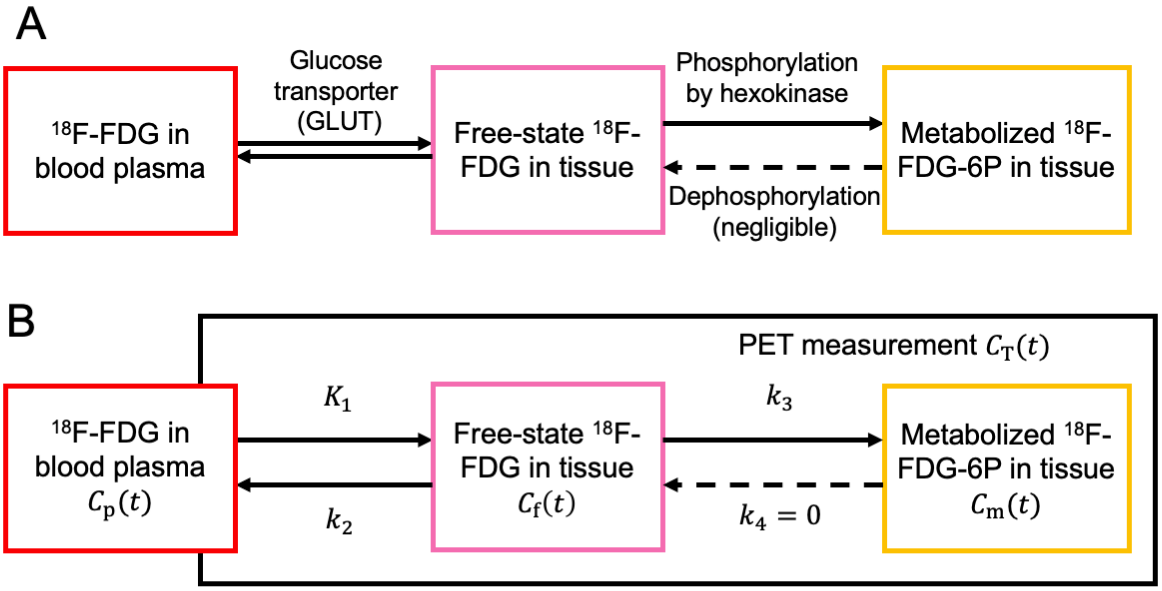

Figure 1.6. The tracer kinetics of ^{18}F-FDG (A) and the corresponding compartmental model (B).

The kinetic model is vital in kinetic modeling and should be carefully designed to accurately describe the kinetics of the modeled tracer. In addition, the model should not be over-complicated to avoid poor robustness in the kinetic quantification, especially considering the noise in the measured data. Hence, a feasible kinetic model should be well-balanced between accuracy and complexity. For example, the tracer kinetics of ^{18}F-FDG are illustrated in Figure 1.6A and can be described with a two-tissue compartmental model shown in Figure 1.6B (*72*). ^{18}F-FDG can transport between the blood plasma and tissue with the help of glucose transporters (GLUTs) (*73*). Once transported in the tissue, ^{18}F-FDG can be phosphorylated into ^{18}F-FDG-6P by hexokinase (*74*). The inverse chemical process, i.e., the dephosphorylation from ^{18}F-FDG-6P to ^{18}F-FDG, is quite slow and is usually negligible. Based on the tracer kinetics, the compartmental model contains three compartments representing the blood input function $C_p(t)$, the free-state ^{18}F-FDG in tissue

$C_\mathrm{f}(t)$, and the metabolized ^{18}F-FDG-6P in tissue $C_\mathrm{m}(t)$. The model supposes that the rate of tracer transport between the compartments is the product of tracer concentration and the rate constant. The rate constants K_1, k_2, k_3, and k_4 represent the rates of blood-to-tissue transport, tissue-to-blood transport, phosphorylation, and dephosphorylation, respectively, and are commonly referred to as micro parameters. k_4 is usually set to zero due to the negligible dephosphorylation. As a result, the tracer concentration in different compartments can be described as the following ordinary differential equation set:

$$\frac{\mathrm{d}}{\mathrm{d}t}\begin{bmatrix} C_\mathrm{f}(t) \\ C_\mathrm{m}(t) \end{bmatrix} = \begin{bmatrix} -k_2 - k_3 & 0 \\ k_3 & 0 \end{bmatrix}\begin{bmatrix} C_\mathrm{f}(t) \\ C_\mathrm{m}(t) \end{bmatrix} + \begin{bmatrix} K_1 \\ 0 \end{bmatrix} C_\mathrm{p}(t). \qquad \text{Eq. 1.6}$$

The ^{18}F-FDG concentration in the extravascular tissue, $C_\mathrm{t}(t)$, is the summation of the free and the phosphorylated ^{18}F-FDG,

$$C_\mathrm{t}(t) = C_\mathrm{f}(t) + C_\mathrm{m}(t) = H(t;\boldsymbol{\kappa}) \otimes C_\mathrm{p}(t), \qquad \text{Eq. 1.7}$$

where $\boldsymbol{\kappa} = [K_1, k_2, k_3]^\mathrm{T}$, $\otimes$ denotes the convolution operation, and $H(t;\boldsymbol{\kappa})$ is the impulse response function of the 2Ti model:

$$H(t;\boldsymbol{\kappa}) = \frac{K_1}{k_2+k_3}\left(k_3 + k_2 \mathrm{e}^{-(k_2+k_3)t}\right). \qquad \text{Eq. 1.8}$$

The measured ROI TAC $\check{C}_\mathrm{T}(t)$ by PET is modeled as $C_\mathrm{T}(t)$, which is as a mixture of compartments:

$$C_\mathrm{T}(t) = (1 - v_\mathrm{b})\big(C_\mathrm{f}(t) + C_\mathrm{m}(t)\big) + v_\mathrm{b} C_\mathrm{wb}(t), \qquad \text{Eq. 1.9}$$

where v_b is the blood volume fraction, and $C_\mathrm{wb}(t)$ is the whole-blood activity. $C_\mathrm{wb}(t)$ is usually obtained through TAC extraction from the blood pool or blood sampling. The ^{18}F-FDG net influx rate K_i can be derived from micro kinetic parameters K_1, k_2, and k_3:

$$K_{\mathrm{i}} = \frac{K_1 k_3}{k_2 + k_3}. \qquad \text{Eq. 1.10}$$

K_{i} is proportional to the overall metabolic rate of glucose and is a macro parameter of interest.

The kinetic parameters collectedly noted as $\boldsymbol{\theta} = [v_{\mathrm{b}}, K_1, k_2, k_3]^{\mathrm{T}}$ can be estimated through the nonlinear least-square fitting of the measured $\check{C}_{\mathrm{T}}(t_m)$ with the modeled $C_{\mathrm{T}}(t_m)$:

$$\widehat{\boldsymbol{\theta}} = \arg\min_{\boldsymbol{\theta}} WRSS(\boldsymbol{\theta}), WRSS(\boldsymbol{\theta}) = \sum_{m=1}^{M} w_m \left[\check{C}_{\mathrm{T}}(t_m) - C_{\mathrm{T}}(t_m)\right]^2 \quad \text{Eq. 1.11}$$

where $WRSS(\boldsymbol{\theta})$ denotes the weighted residual sum of squares of the curve fitting. t_m is the time of the m-th frame in a total of M frames of the dynamic data, and w_m is the weight for frame m.

The nonlinear least-square fitting can be implemented through the Levenberg–Marquardt algorithm (75,76). It is worth noting that this iterative fitting can be computationally expensive for parametric imaging.

As an alternative to compartmental modeling, graphical plot methods can estimate certain kinetic parameters. For example, the Patlak plot (77) can approximate K_{i} using the linear slope of the graphical plot of $C_{\mathrm{p}}(t)$ and $C_{\mathrm{T}}(t)$:

$$\frac{C_{\mathrm{T}}(t)}{C_{\mathrm{p}}(t)} = K_{\mathrm{i}} \frac{\int_0^t C_{\mathrm{p}}(\tau)\mathrm{d}\tau}{C_{\mathrm{p}}(t)} + V, t > t^*, \qquad \text{Eq. 1.12}$$

in which t^* represents the steady-state time, and V is the intercept. An illustrative example of the Patlak plot is shown in Figure 1.7. Graphical plot methods have the advantages of computational efficiency and noise robustness for parametric imaging but exclusively estimate a subset of kinetic parameters.

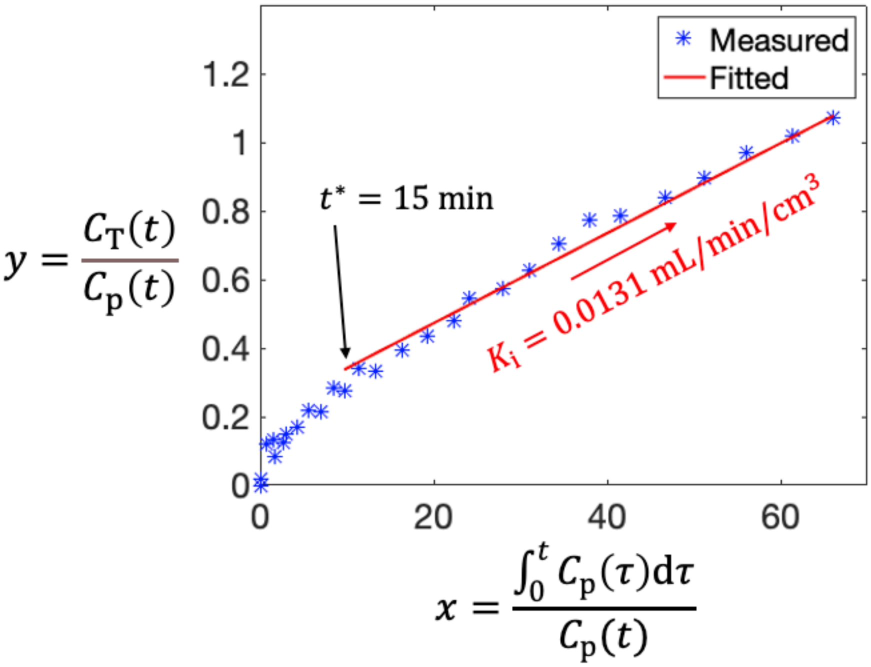

Figure 1.7. An illustrative example of the Patlak plot.

1.5. Limitations of Dynamic Imaging on Conventional PET Scanners

Conventional PET scanners have a short AFOV, typically 15 to 30 cm (Figure 1.4A). Owing to the isotropic nature of the annihilation photon emission, the detection sensitivity within the short AFOV is low, leading to a high noise level in dynamic images. Besides, there are more challenges for whole-body dynamic imaging with a short AFOV scanner. As the scanner must use multiple bed positions and multiple passes for dynamic whole-body imaging (Figure 1.4C) (*58,59*), the early-phase data (e.g., 0 - 5 min) that have unique information, such as about blood flow and blood volume, are only available for limited imaged regions. In addition, large temporal gaps exist in the whole-body dynamic frames at any given scanned location, which can further weaken the robustness of parameter quantifications.

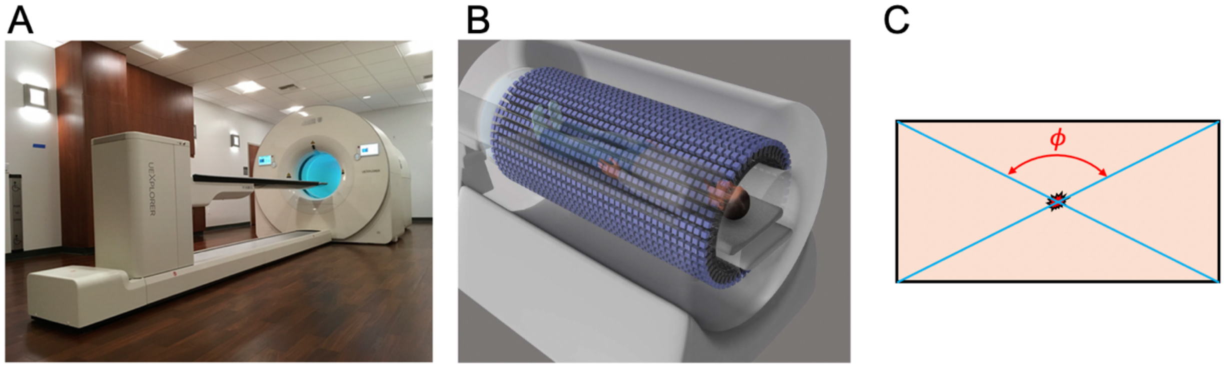

Figure 1.8. A. The total-body PET system uEXPLORER installed in Explorer Molecular Imaging Center at University California Davis Medical Center. It allows the simultaneous imaging of the total body (B) and permits a larger angle for the detection of an annihilation photon pair (C) as compared with a conventional short AFOV PET scanner (refer to Figure 1.3C). Figure A courtesy of Dr. Benjamin A. Spencer. Figure B courtesy of Dr. Simon R. Cherry.

Apart from the above difficulties associated with the $C_{\mathrm{T}}(t)$ measurement, the acquisition of an input function $C_{\mathrm{p}}(t)$ with short AFOV PET scanners is also challenging. If the IDIF is to be acquired, the location of the first bed position may need to be shifted away from the main organ of interest (e.g., the brain) to a location covering a blood pool such as the aorta, losing valuable early information in the organ of interest. In this case, the obtained dynamic data may not be sufficient for the compartmental model to provide reliable parameter estimation.

1.6. The Advancement of Total-Body PET

The development of the uEXPLORER total-body PET/CT system (*78*,*79*), with a 194 cm AFOV (Figure 1.8A), is an important step in addressing several limitations of conventional short AFOV PET scanners. It allows simultaneous imaging of the entire body (Figure 1.8B), which eliminates the large temporal gaps in conventional dynamic whole-

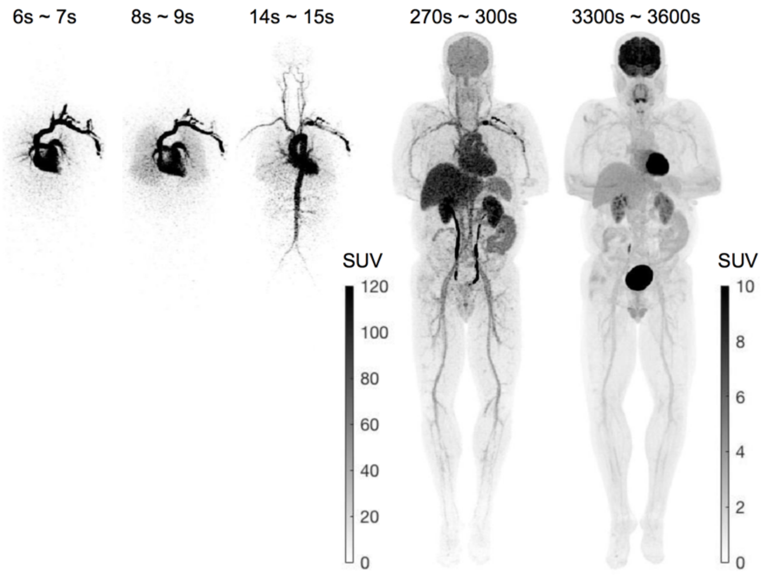

Figure 1.9. High temporal resolution total-body dynamic images acquired using the uEXPLORER PET/CT system.

body imaging. Besides, the total-body axial coverage brings a larger solid angle for annihilation photon pair detection (Figure 1.8C). As a result, the uEXPLORER achieves a >40-fold improvement in the effective detection sensitivity and a 5- to 6-fold increase in the image signal-to-noise ratio for total-body static PET imaging compared with the whole-body imaging with short AFOV scanners *(78)*. The giant increase in sensitivity enables various novel applications in image acquisition. For example, the low-dose imaging with uEXPLORER can be performed with a 40-fold lower dose while maintaining the image quality for clinical use, and the delayed imaging is accommodated with about five times the half-life longer. The increased detection sensitivity by total-body PET systems also benefits dynamic imaging. It permits dynamic imaging with much higher temporal resolution (HTR), such as 1 s per time frame or even 0.1 s per frame *(80)* compared to the 10 - 40 s per frame protocols of short AFOV scanners. An example set of HTR total-body dynamic images is shown in Figure 1.9. These advantages are very promising for novel clinical applications.

1.7. Research Opportunities of Kinetic Modeling with Total-Body PET

Total-body PET brings unprecedented change to PET imaging and provides a lot of new research opportunities in kinetic modeling. This work aims to study these research opportunities and their potential clinical impact. Our studies underscore applications to lung disease and beyond for the unique dual-blood supplies of the lung (*81–85*) and the total-body effect of lung diseases such as the coronavirus disease 2019 (COVID-19) (*86*).

1.7.1. High-Temporal Resolution Kinetic Modeling

The ability of uEXPLORER for HTR imaging (e.g., 1s per frame), combined with the total-body field of view, allows a better temporal sampling of tissue TACs from the entire body and the extraction of various IDIFs. These measurements help with a more accurate evaluation of fast tracer kinetics and provide associated research opportunities for HTR kinetic modeling. Examples include the multiphase Patlak plot that investigates additional approximately linear phases in the early phase data (*87*) and the separation of blood flow and tracer-specific transport from the overall tracer delivery rate through the time-varying kinetic modeling (*88*).

Our studies of the HTR kinetic modeling in this work focus on the lung. The lung has unique tracer kinetics as it has dual blood supplies from the pulmonary artery (*81*,*82*) and the bronchial artery (*83–85*). While the blood supply of normal lung tissue is usually dominated by the pulmonary artery, the supply fraction from the bronchial artery can increase in lung tumors (*89–91*). With total-body dynamic PET, it becomes feasible to

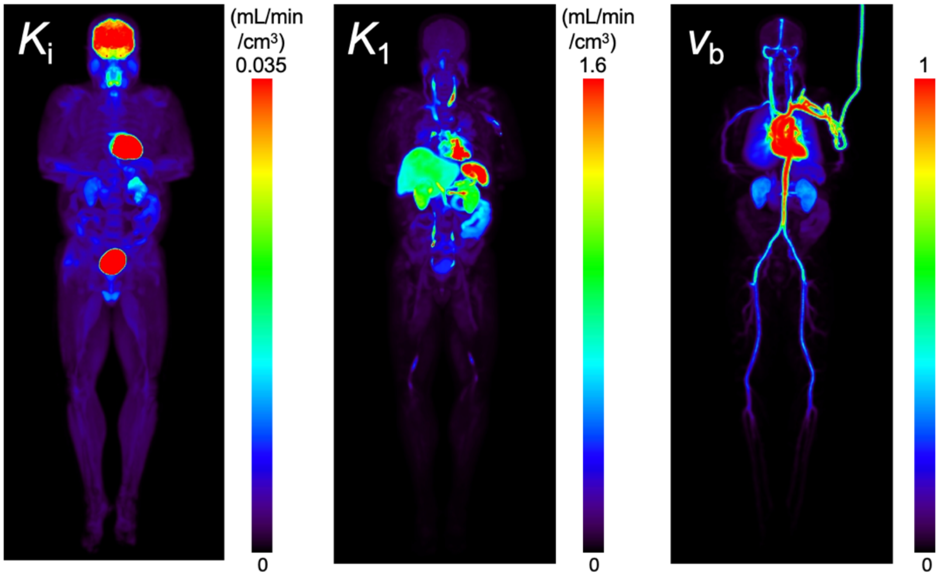

Figure 1.10. Multiparametric images of ^{18}F-FDG net influx rate K_{i}, ^{18}F-FDG delivery rate K_1, and fractional blood volume v_{b}. The images are maximum intensity projections.

measure lung TACs with high temporal resolution and derive the individual input functions of the bronchial artery and the pulmonary artery through the IDIF extraction from the left ventricle and the right ventricle, respectively. However, we found the existing compartmental model insufficient for modeling the acquired HTR. Hence, corrections to the input function were explored in Chapter 2, and we improved the HTR kinetic modeling of normal lung tissue with the RV input function. Further, we proposed the dual-blood input function (DBIF) to model the dual-blood supply of lung tumors in Chapter 3. Combined with the corrections in Chapter 2, we evaluated the impact of the DBIF on the kinetic modeling with HTR dynamic data and demonstrated the altered blood supply in lung tumors.

1.7.2. Total-Body Multiparametric Imaging

Limited by the short AFOV, conventional PET scanners cannot simultaneously capture the total-body kinetics, especially in the early phase of radiotracer bolus distribution. Thus, the full potential of compartmental modeling that allows quantification of microkinetic parameters (e.g., the tracer delivery rate K_1 and fractional blood volume v_b) is difficult to explore. For example, a whole-body K_i image can be obtained with conventional scanners with the Patlak plot, whereas a whole-body K_1 image cannot.

Total-body dynamic imaging with the uEXPLORER system has the potential to address this shortcoming and enable high-quality total-body kinetic modeling and parametric imaging of microkinetic parameters. Figure 1.10 shows an example of parametric imaging of ^{18}F-FDG uptake rate K_i, fractional blood volume v_b, and ^{18}F-FDG delivery rate K_1 from a uEXPLORER scan. K_1 is of particular clinical interest among the parameters because of its connection to blood flow and the ability to provide complementary information besides the most commonly used K_i. Previous investigations of K_1 include the evaluation of perfusion-metabolism mismatch for myocardial viability (*92*) and the assessment of liver inflammation (*93*). In addition to K_1, the total-body parametric imaging of the fractional blood volume v_b may also add useful physiological and pathological information. For example, v_b may reveal the local blood supply and microenvironment of a tumor and thus may benefit tumor diagnosis and characterization (*69*).

Total-body multiparametric imaging enables a multiorgan evaluation of tracer kinetics, which is promising for investigating systematic diseases. In Chapter 4, we applied this multiorgan analysis of ^{18}F-FDG delivery and metabolism to recovering COVID-19 subjects as compared to a group of healthy subjects. An increase in the lung ^{18}F-FDG metabolism was detected in the COVID-19 group, as represented by K_i. Furthermore, we observed an increase in the bone marrow K_1 of the COVID-19 group. The results may reflect a continued immune response and may be otherwise missed if only evaluated with K_i or SUV.

1.7.3 Applications of Deep Learning

Deep learning has attracted broad attention for its huge potential in almost every field, including PET (*94*). One major advantage of deep learning is its high efficiency. Once a model is trained, its prediction can be fast compared to conventional algorithms of kinetic modeling. The high efficiency feature of deep learning makes it promising for total-body parametric imaging because the latter has millions of voxel-wise dynamic data to process and there is an imperative need for efficient approaches. In addition, the quality of total-body parametric imaging may be improved by deep learning, as leveraged by its capability in noise reduction (*95*).

Given the potential advantages of deep learning, we investigated its implementation for total-body parametric imaging in Chapter 5. We first studied total-body kinetic model selection, which selects the appropriate kinetic model for each voxel in the body. The

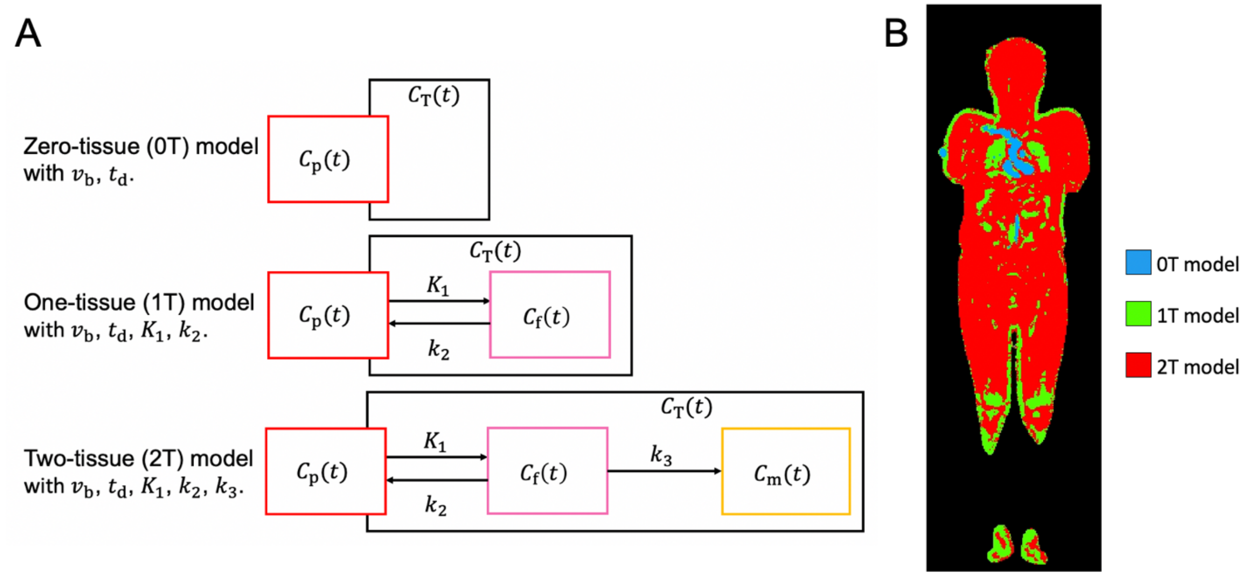

Figure 1.11. A. Three different candidate kinetic models for total-body parametric imaging. K_1 and k_2 are blood-to-tissue and tissue-to-blood ^{18}F-FDG delivery rates, respectively. k_3 is the ^{18}F-FDG phosphorylation rate. v_b is the fractional blood volume. t_d is the time delay of blood input function. B. Total-body model selection map generated with the Akaike information criterion (AIC) method.

model selection helps with artifact suppression of parametric images *(69)*, but traditional approaches for model selection, such as the Akaike information criterion (AIC) (as illustrated in Figure 1.11) *(96)*, can be time-consuming. We applied deep learning for total-body model selection and proposed a single-subject deep learning strategy to avoid the need for population-based training data. This strategy takes the training data from a small fraction of the voxels of a subject and predicts the kinetic model for the remaining voxels of the same subject. Our preliminary test showed good model selection accuracy and high efficiency.

Further, we studied deep learning for total-body voxel-wise kinetic parameter quantification. We proposed the Deep Patlak, a deep neural network inspired by the Patlak plot method and more interpretable than a direct application of common deep learning or machine learning methods *(97–102)*. The proposed Deep Patlak achieved good parametric image quality and was more efficient than the traditional curve-fitting-based method.

1.8. Summary

This chapter first covers basic concepts of PET imaging and tracer kinetic modeling. We then introduce the advancement of total-body PET, which enables total-body dynamic scans with high image quality and permits lots of opportunities for kinetic modeling. Based on these research opportunities, the following chapters will study different topics of kinetic modeling and parametric imaging with total-body PET, including HTR kinetic modeling (Chapter 2 and Chapter 3), total-body multiparametric imaging (Chapter 4), and associated deep learning applications (Chapter 5). Finally, the studies are discussed and summarized in Chapter 6.

Chapter 2. High-Temporal Resolution Lung Kinetic Modeling Using Total-Body Dynamic PET with Time Delay and Dispersion Corrections

2.1. Introduction

Positron emission tomography (PET) with ^{18}F-fluorodeoxyglucose (^{18}F-FDG) or other radiotracers is a promising method for studying a variety of lung diseases, including lung cancer (*103*), acute lung injury (*104,105*), asthma (*106*), lung fibrosis (*107*), and recently coronavirus disease 2019 (*108*). The standardized uptake value (SUV) is a traditional semi-quantitative measure for evaluating lung ^{18}F-FDG uptake (*62,109*), while kinetic analysis through compartment modeling (*72*) has shown the potential to provide more quantitative tracer kinetics, e.g., the ^{18}F-FDG delivery rate K_1 (*110*), net influx rate K_i (*111–115*) and fractional blood volume v_b (*113,116,117*), to better characterize lung diseases in previous human and animal studies. However, conventional PET scanners have a relatively poor sensitivity and limited temporal resolution (e.g., 10-40s/frame) for dynamic imaging, which in turn affects the performance of lung kinetic quantification.

The advent of the uEXPLORER total-body PET and other long axial field-of-view (FOV) scanners (*78,118,119*) has brought new opportunities to improve lung kinetic modeling by offering a large axial FOV to cover the entire lungs with improved detection efficiency, allowing high temporal resolution (HTR) imaging, e.g., 1 s or even sub-second per frame (*120,121*). The HTR ability is especially useful for capturing the rapidly-changing early phase of tracer uptake in lung tissues. Meanwhile, image-derived blood input functions (IDIFs) can also be extracted with HTR from major blood pools (e.g., ventricles and large blood vessels) for kinetic modeling (*121*,*122*). In this chapter, we investigate the use of HTR data for lung kinetic quantification with total-body PET, expecting improvement especially for those parameters that are sensitive to the early kinetics, such as ^{18}F-FDG delivery rate K_1 and fractional blood volume v_b.

One challenge with using HTR data is the potential need of additional corrections for the IDIF. Recent work on total-body PET kinetic modeling has considered time delay correction to account for the difference between the tracer arrival time in a tissue and the arrival in the blood pool where the IDIF is extracted (*69*,*121*,*122*). However, dispersion (*123*,*124*) may also occur when the tracer travels from the location at which the IDIF is determined to the capillaries of the lungs. The correction for either time delay or dispersion has only rarely been investigated in previous studies of lung kinetic modeling and is usually omitted (*104*,*125–127*), partly due to the limited temporal resolution (e.g., 10s/frame) of conventional dynamic PET. Here we hypothesize that a simultaneous correction for both the time delay and dispersion effects is essential for accurate kinetic modeling in HTR dynamic PET imaging of the lungs.

2.2. Materials and Methods

2.2.1. HTR Dynamic Data Acquisition on uEXPLORER

Thirteen healthy human subjects (age ± SD, 49 ± 15 y, weight ± SD, 82 ± 18 kg, six males, seven females) signed written informed consent and were scanned on the uEXPLORER total-body PET/CT system (*128*,*129*). The study was approved by the

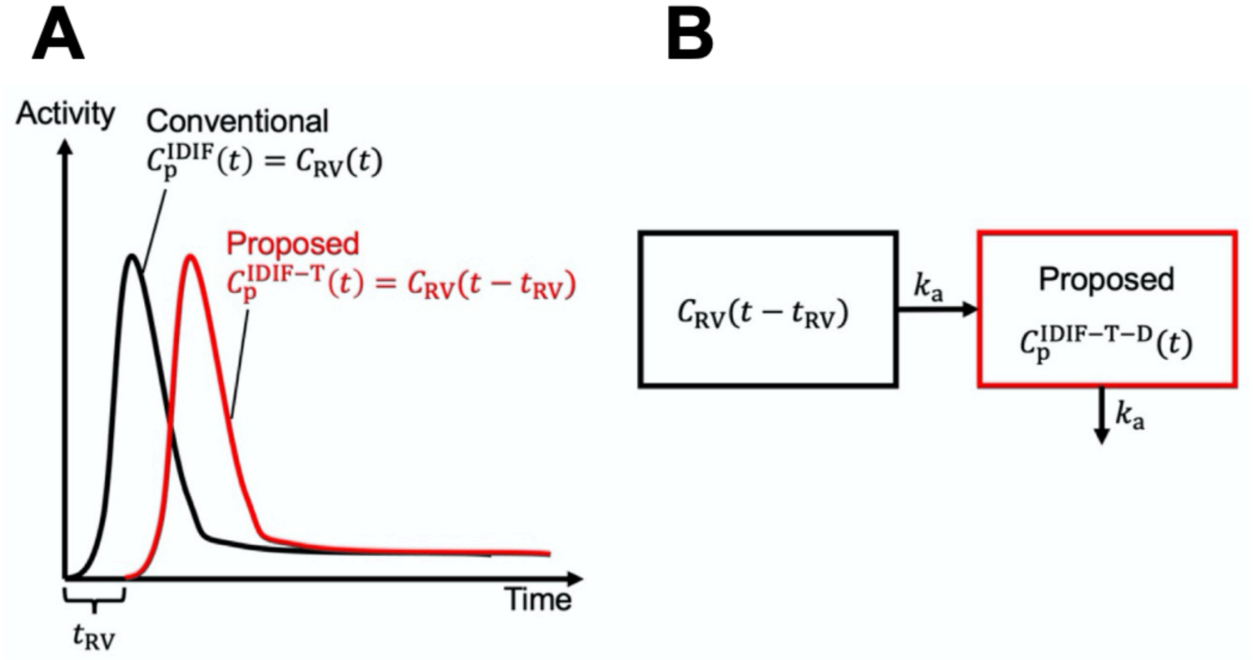

Figure 2.1. (A) Proposed IDIF-T model with the correction of time delay in the input function. (B) The proposed IDIF-T-D model with both time delay and dispersion corrections included.

Institutional Review Board at the University of California, Davis. After an ultralow-dose CT scan (140 kVp, 5 mAs), each participant underwent a dynamic ^{18}F-FDG-PET scan with intravenous bolus administration of a dose of ~370 MBq. Total-body PET imaging was performed for 60 minutes starting immediately before the injection. The resulting list mode data were reconstructed into dynamic images using the vendor-supplied time-of-flight ordered subset expectation maximization (TOF-OSEM) algorithm with four iterations and 20 subsets and a voxel size of $4 \times 4 \times 4$ mm^3. The dynamic framing protocol contains 120 frames over 60 minutes: $60 \times 1\ \mathrm{s}, 30 \times 2\ \mathrm{s}, 6 \times 10\ \mathrm{s}, 6 \times 30\ \mathrm{s}, 12 \times 120\ \mathrm{s}, 6 \times 300\ \mathrm{s}$ with HTR frames (1-2 s per frame) over the first 2 minutes. For each subject, a region of interest (ROI) was placed in the right ventricle (RV) to extract an IDIF $C_{\mathrm{RV}}(t)$ to represent the pulmonary blood supply, the dominant blood input to the lungs (*81,84*). Five ROIs were placed in the left and right lungs, one in each of the five lung lobes, to extract lung time-activity curves (TACs) from the dynamic images with diminished effects of motion and spill-over. The five lung-ROI TACs were averaged to generate a global lung TAC $\check{C}_{\mathrm{T}}(t)$ for each of the thirteen subjects. An additional ROI was also placed in the left ventricle (LV) to extract the TAC $C_{\mathrm{LV}}(t)$ for the purpose of comparison. In addition to the HTR TACs, TACs of low temporal resolution (LTR) were also generated by using 10-s/frame for the first three minutes for all the ROIs.

2.2.2. Compartmental Modeling

^{18}F-FDG kinetics in the extravascular lung is described by a two-tissue irreversible (2Ti) compartmental model (*2*), and is illustrated in Figure 1.6B. The compartmental model is described in Section 1.4 and follows as Eqs. 1.6-1.9.

Following previous studies (*104*,*130*,*131*), the right ventricle IDIF can be used for the blood input,

$$C_{\mathrm{p}}^{\mathrm{IDIF}}(t) = C_{\mathrm{RV}}(t), \qquad \text{Eq. 2.1}$$

based on the fact that the pulmonary circulation accounts for most of the total blood input to the lung (*84*).

The measured lung TAC $\check{C}_{\mathrm{T}}(t)$ was fitted with the model TAC $C_{\mathrm{T}}(t)$ using a non-linear least-square formulation as Eq. 1.11. The weight for the m^{th} frame w_m considers the time length and nuclear decay (*132*):

$$w_m = \Delta t_{\mathrm{m}} \exp(-\lambda t_m). \qquad \text{Eq. 2.2}$$

Here Δt_m is the length of the m-th frame, $\lambda = \frac{\ln(2)}{T_{1/2}}$ is the decay constant, and the half-life

$T_{1/2} = 109.8$ min for ^{18}F-FDG. This time-varying weight was selected based on our initial studies of model fitting (not shown).

2.2.3. Modeling of Time Delay Effect

Corrections for time delay were seldom considered in previous studies of lung kinetic modeling (*104,125–127*) because the delay was usually only several seconds and tended to be blurred out by conventional dynamic imaging of limited temporal resolution (e.g., 10s/frame). However, the time delay effect will be no longer concealed with the HTR measurement (e.g., 1s/frame) and is likely to affect parameter quantification if not accounted for.

To model the time delay effect of the IDIF extracted from the right ventricle, we include a time delay parameter t_{RV} (s) in the input function (Figure 2.1A):

$$C_{\mathrm{p}}^{\mathrm{IDIF-T}}(t) = C_{\mathrm{RV}}(t - t_{\mathrm{RV}}). \qquad \text{Eq. 2.3}$$

The proposed input function model with time delay correction is noted as IDIF-T. The time delay parameter t_{RV} is included in $\boldsymbol{\theta}$ and will be jointly estimated with other kinetic parameters during TAC fitting.

2.2.4. Simultaneous Correction for Dispersion

Dispersion may occur when the tracer travels from the right ventricle to the lung capillaries. Here we model the actual lung blood input as the convolution of the measured IDIF with a parameterized dispersion function following Iida's mono-exponential form (*93,123*),

$$C_{\mathrm{p}}^{\mathrm{IDIF-T-D}}(t) = C_{\mathrm{p}}^{\mathrm{IDIF-T}}(t) \otimes k_{\mathrm{a}} \exp(-k_{\mathrm{a}} t) = C_{\mathrm{RV}}(t - t_{\mathrm{RV}}) \otimes k_{\mathrm{a}} \exp(-k_{\mathrm{a}} t). \qquad \text{Eq. 2.4}$$

This input function model is denoted as IDIF-T-D (Figure 2.1B), in which both the dispersion parameter k_{a} (/min) and time delay t_{RV} (s) are included in $\boldsymbol{\theta}$ for joint parameter estimation.

Note that here the simultaneous dispersion correction is different from those explored for brain PET (*124*). Previous work focused on a "backward" dispersion correction problem (*123*,*124*). The measured input function, e.g., by arterial blood sampling from radial artery, is a dispersed version of the actual input function. Therefore, the dispersion needs to be removed from the measured input function. In comparison, our work here is a "forward" dispersion correction problem. The actual lung input function is a dispersed version of the measured IDIF, to which the dispersion needs to be added.

2.2.5. Evaluation of TAC Fit Quality

The Akaike information criterion (AIC) was used to compare the statistical fit quality of different models (*133*,*134*),

$$\mathrm{AIC} = M \ln\left(\frac{WRSS}{M}\right) + 2N + \frac{2N^2+2N}{M-N-1}, \qquad \text{Eq. 2.5}$$

where N is the number of unknown parameters to be optimized in $\boldsymbol{\theta}$ and M is the number of dynamic frames. AIC reflects the trade-off between the goodness of fit and the simplicity of the model, and thus accounts for the difference in the number of parameters that need to be estimated. A lower AIC value indicates better fitting quality.

2.2.6. Evaluation of the Impact on Kinetic Quantification

We evaluated the impact of the corrections on the quantification of three kinetic parameters of interest: ^{18}F-FDG delivery rate K_1, net influx rate K_i (calculated with Eq. 1.10), and fractional blood volume v_b.

The change in each kinetic parameter by a given model was reported relative to the parameter estimate by the standard IDIF model, and the reason for the quantification changes was studied by analyzing the TAC fittings of different models.

2.2.7. Identifiability Analysis of Kinetic Parameter Estimates

As the proposed models have more parameters to estimate than the standard 2Ti model with the uncorrected IDIF, their kinetic parameter identifiability may be a concern. That is because a more complex model is more likely to be sensitive to random noise and may have reduced parameter stability. To evaluate the parameter identifiability, a noisy lung tissue TAC $\tilde{C}_\mathrm{T}(t_m)$ was simulated using a time-varying Gaussian model (*135–137*):

$$\tilde{C}_\mathrm{T}(t_m) \sim N\left(\bar{C}_{\mathrm{T},m}, S_\mathrm{c}\delta_m\right). \qquad \text{Eq. 2.6}$$

where $\bar{C}_{\mathrm{T},m}$ is the m-th frame of the noise-free TAC generated by the curve fitting of the tested model. S_c is the scaling factor controlling the noise level and δ_m is the unscaled standard deviation given by:

$$\delta_m = \sqrt{\frac{\bar{C}_{\mathrm{T},m} \exp\left(\lambda t_m\right)}{\Delta t_m}} \qquad \text{Eq. 2.7}$$

S_c was estimated using the residual error between the measured $\check{C}_\mathrm{T}(t)$ and the modeled $C_\mathrm{T}(t)$ using the model that demonstrated the best fitting by assuming the fitting error of that model comes mostly from random noise. We simulated 500 noisy lung tissue TAC realizations for each $\tilde{C}_{\mathrm{T}}(t)$ and analyzed the bias and noise standard deviation of each parameter estimate. The analysis was conducted for the three models (i.e., the IDIF, IDIF-T, and IDIF-T-D) using the HTR data. By summing the corresponding HTR frames together, the IDIF model using a more conventional low temporal resolution (10 s per frame in the first three minutes) was also included for comparison.

2.2.8. Correlation of Lung ^{18}F-FDG Kinetics with Age

Aging effects are evident in healthy lungs. Previous human studies have observed an inverse relationship between age and pulmonary blood volume (*138*,*139*). Therefore, we hypothesize the fractional blood volume v_{b} in the lungs tends to decrease with aging. Although we do not have longitudinal data of individuals in this study, we aim to explore any association between the ^{18}F-FDG kinetic parameters and age using the available healthy subject cohort. We performed the Pearson regression analysis between age and kinetic parameters. Body mass index (BMI) was also included in the regression to consider potential confounding factors.

2.2.9. Demonstration of Total-Lung Parametric Imaging

In addition to the ROI-based kinetic analysis, we also implemented the proposed kinetic modeling approach voxel-by-voxel. Parametric images of different kinetic parameters (e.g., K_1, K_{i}, and v_{b}) were then generated for the entire lung. Kernel smoothing was applied to both the dynamic images and parametric images for noise reduction (*69*).

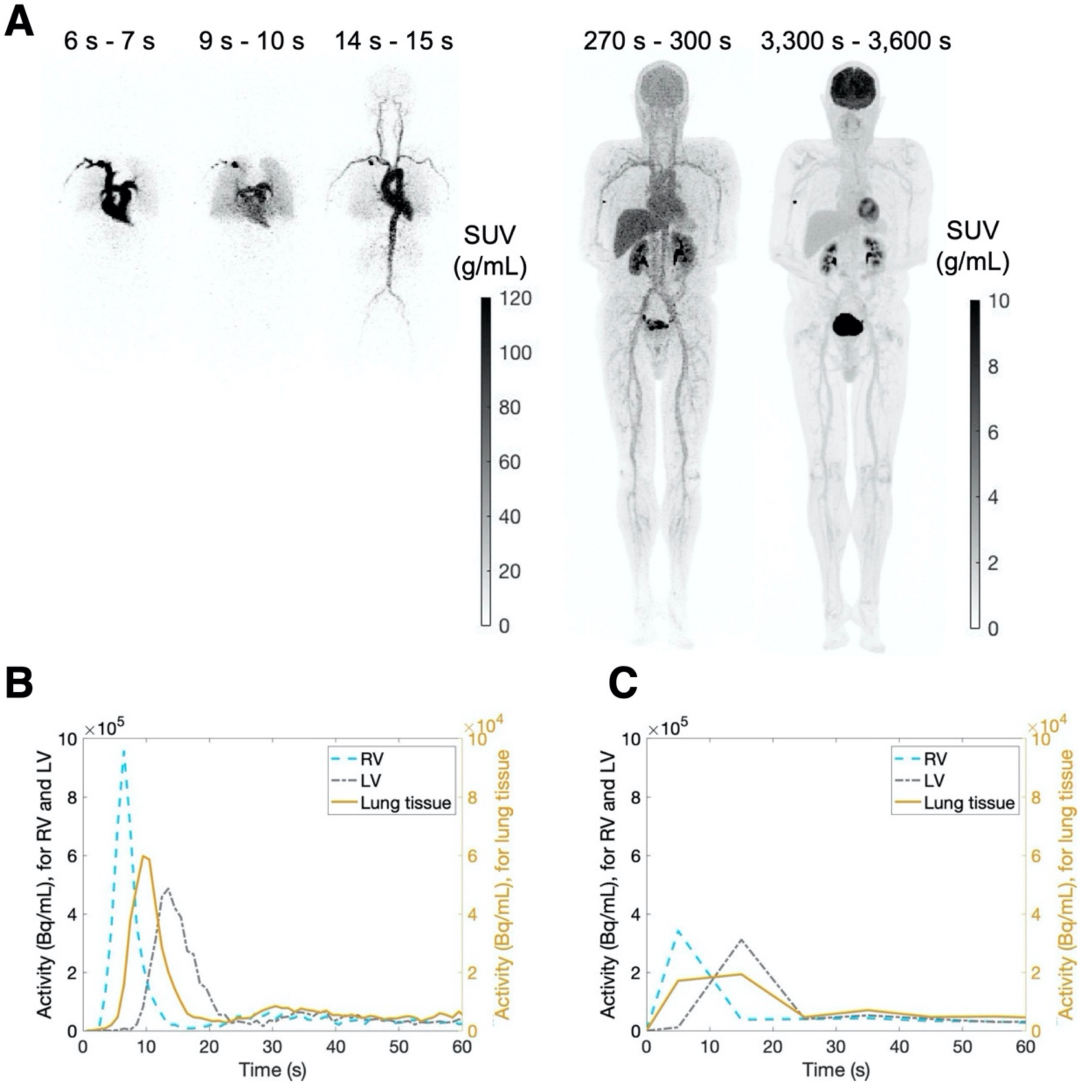

Figure 2.2. (A) High temporal resolution (1 s per frame) total-body ^{18}F-FDG dynamic images of an example subject acquired using the uEXPLORER system. (B) Regional TACs extracted from the HTR dynamic images. The *y* axis on the left is for the TACs of the right ventricle (RV) and the left ventricle (LV), while the *y* axis on the right is for the TAC of lung tissue which has a factor of 10 lower range. (C) Conventional low temporal resolution (10 s per frame) regional TACs.

2.3. Results

2.3.1. Example of HTR Dynamic Images and TACs

Figure 2.2 shows the acquired HTR total-body dynamic data for one representative subject. The ^{18}F-FDG dynamics in the very early phases post-injection were captured by the high temporal resolution, as illustrated by the total-body maximum-intensity projections (MIPs) of the SUV image in the coronal direction (Figure 2.2A) and the HTR TACs (Figure 2.2B). To begin with, the tracer was injected into a vein in the right arm before traveling to the right ventricle through the vena cava (Figure 2.2A, 6 s – 7 s of the scan time). The tracer next traveled through the pulmonary circulation by flowing into the lungs via the pulmonary artery (Figure 2.2A, 9 s - 10 s) and flowing out of the lungs to the left ventricle through the pulmonary veins (Figure 2.2A, 14 s -15 s).

As a comparison, TACs with the conventional temporal resolution are shown in Figure 2.2C. With a 10-s temporal resolution, the TACs have lost much of the information about the early-phase ^{18}F-FDG kinetics. Both the shape and amplitude of the TACs were distorted and inaccurate due to the poor temporal resolution.

2.3.2. Model Fitting of Lung TAC

The proposed approaches for modeling the input function can clearly impact the TAC fitting, as shown by the fitting results for one example subject in Figure 2.3A along with the residual fitting errors in Figure 2.3B. These figures focus on the early dynamic phase, given that the late phase is similar among different models. Without the time delay

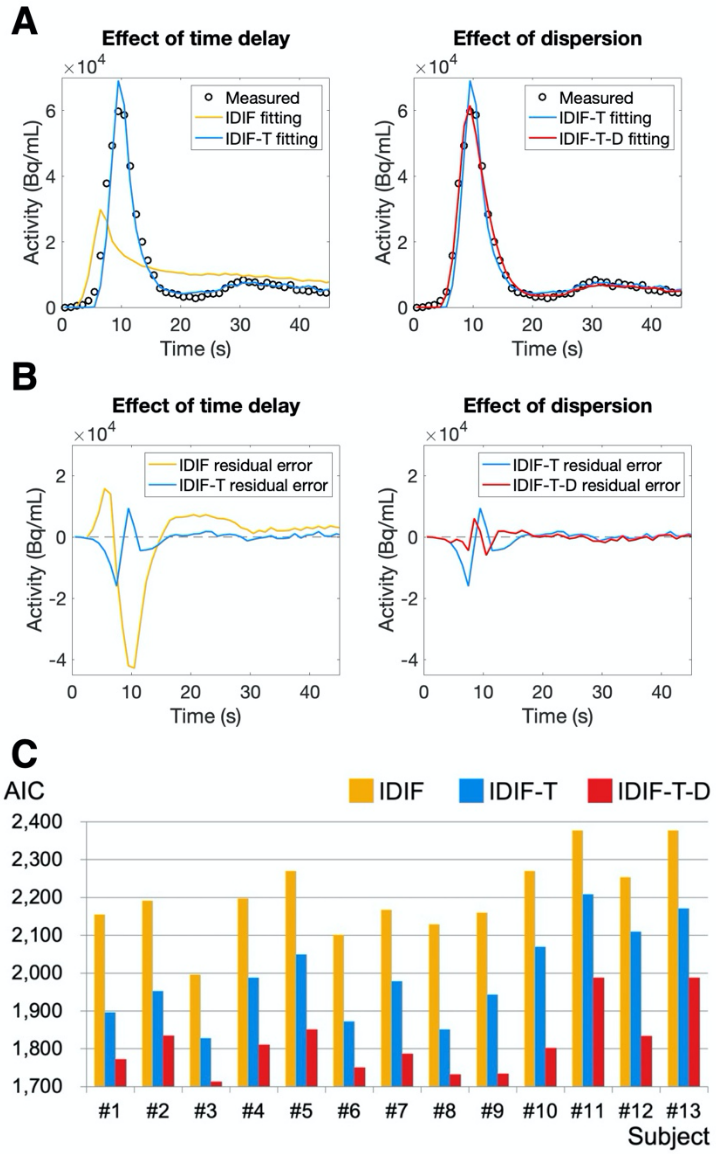

Figure 2.3. (A) Effects of modeling time delay and dispersion on fitting of a measured lung TAC. (B) Effects on the residual error of TAC fitting. (C) AIC of different models in thirteen subjects. IDIF: the traditional model with the uncorrected image-derived input function; IDIF-T: the model with time delay correction only; IDIF-T-D: the model with both time delay and dispersion corrections.

correction, the conventional IDIF model failed to fit the early phase data even though the time delay is ~3 seconds (Figure 2.4A). The dispersion correction in the IDIF-T-D model further improved the fitting of the first peak because it accounts for the deformation of the

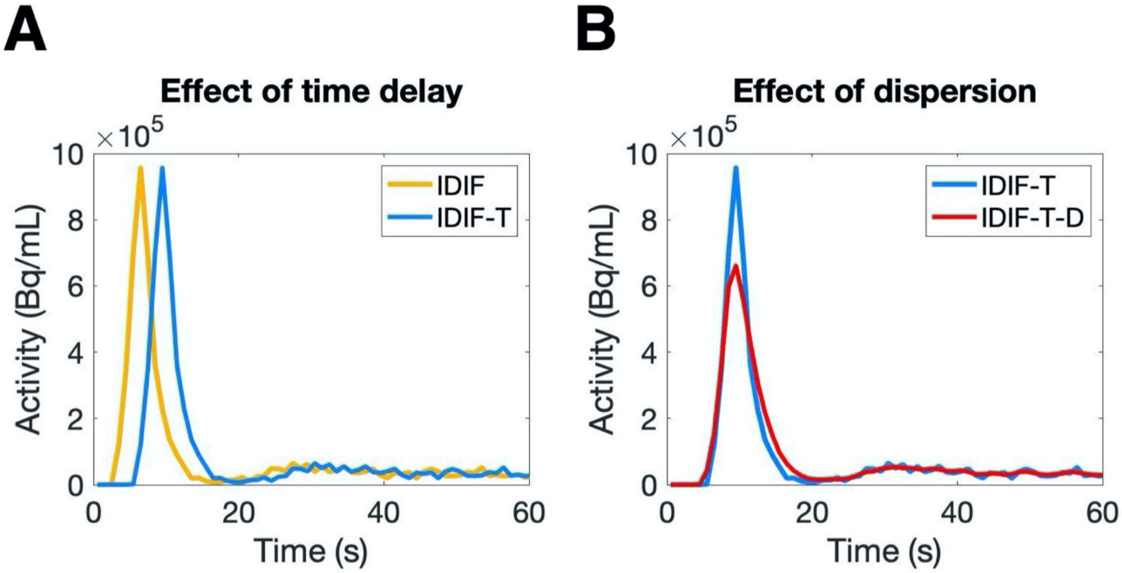

Figure 2.4. Effects of time delay correction (A) and dispersion correction (B) on the blood input function.

input function caused by the tracer dispersion effect (Figure 2.4B). The improved fitting by the proposed models (IDIF-T and IDIF-T-D) is further demonstrated by the decreased AIC (Figure 2.3C and Table 2.1). The IDIF-T-D model achieved the best average AIC across all subjects.

2.3.3. Kinetic Parameter Estimation

The mean and standard deviation values of lung kinetic parameters are reported in Table 2.2. Figure 2.5 shows the resulting impact on the quantification of K_1, K_i, and v_b.

Using the IDIF model without time delay or dispersion correction, the K_1 value of 0.350 ± 0.092 mL/min/cm^3 seems unreasonable and is due to the poor fitting. This further

Table 2.1. AIC Values of Different Kinetic Models Averaged from the Thirteen Subjects

Model	AIC
IDIF	2203.2 ± 106.6
IDIF-T	1993.6 ± 121.3
IDIF-T-D	1815.2 ± 87.9

Table 2.2. Lung ^{18}F-FDG Kinetic Quantification of K_1, v_b, K_i, t_RV and k_a Using Different Models

Model	IDIF	IDIF-T	IDIF-T-D
$K_1(\mathrm{mL/min/cm^3})$	0.350 ± 0.092	0.190 ± 0.066	0.056 ± 0.033
v_b	0.042 ± 0.022	0.107 ± 0.024	0.144 ± 0.030
$K_\mathrm{i}(\mathrm{mL/min/cm^3})$	0.00034 ± 0.00032	0.00072 ± 0.00039	0.00060 ± 0.00033
$t_\mathrm{RV}(\mathrm{s})$	/	3.2 ± 0.5	2.1 ± 0.4
$k_\mathrm{a}(\mathrm{/min})$	/	/	25.8 ± 7.1

supports that the direct application of the IDIF without corrections is not appropriate for the HTR data. The model IDIF-T was also likely to overestimate K_1 given the poor early-phase fitting. The IDIF-T-D estimates of K_1 are 0.056 ± 0.033 mL/min/cm^3, with an ~85% decrease compared with the conventional IDIF model. The IDIF-T-D model estimated v_b to be 0.144 ± 0.030, much higher than that obtained with the IDIF (0.042 ± 0.022) and IDIF-T (0.107 ± 0.024) models. A previous study showed a blood fraction of 0.16 in the normal human lungs (*113*). Thus, the v_b estimates by IDIF and IDIF-T are likely biased, whereas the estimates by IDIF-T-D are more consistent with the expected v_b values. For K_i quantification, the proposed IDIF-T-D had an average increase of ~75% compared with the conventional IDIF model.

To understand the observed changes in parameter estimation, we analyzed the predicted activity of individual compartments (Figure 2.6). The vascular component $v_\mathrm{b}C_\mathrm{p}(t)$ was much increased in the IDIF-T-D model as compared to the IDIF due to the increased v_b estimate. Therefore, the total extravascular component $C_\mathrm{t}(t)$ was decreased

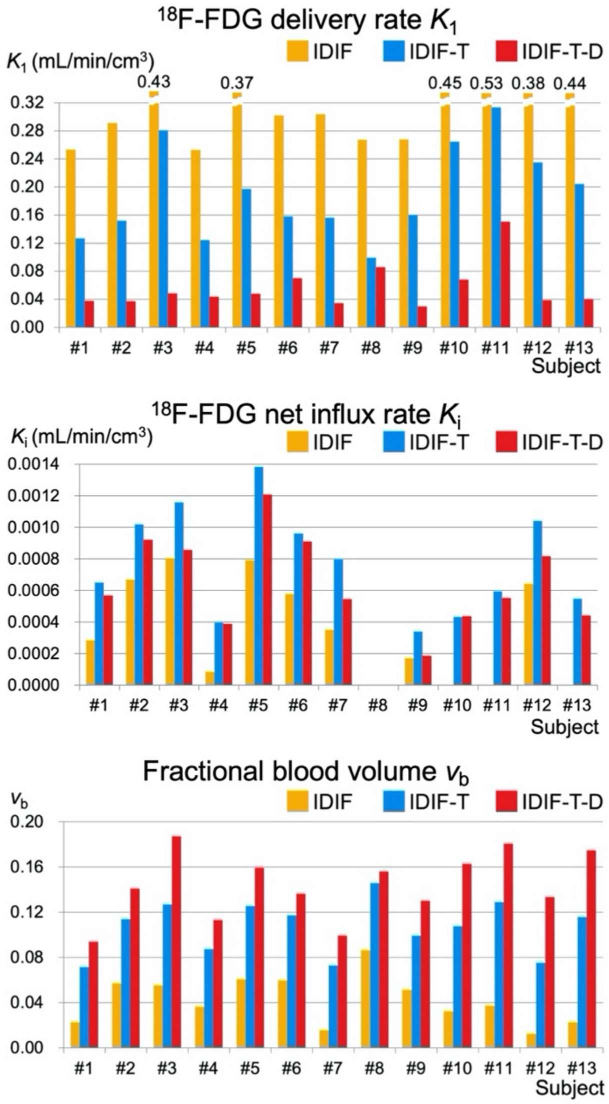

Figure 2.5. Kinetic parameter estimates by different lung kinetic models (IDIF, IDIF-T and IDIF-T-D): ^{18}F-FDG delivery rate K_1 (top), ^{18}F-FDG net influx rate K_i (middle), and fractional blood volume v_b (bottom).

(Eqs. 1.7 and 1.9, and Figure 2.6C) and K_1 became smaller accordingly (Eq. 1.8). In addition, K_i was higher in IDIF-T-D than the IDIF model due to the increased $C_\mathrm{m}(t)$ (Figure 2.6D), which was associated with decreased K_1, k_2 but increased k_3 (results not shown).

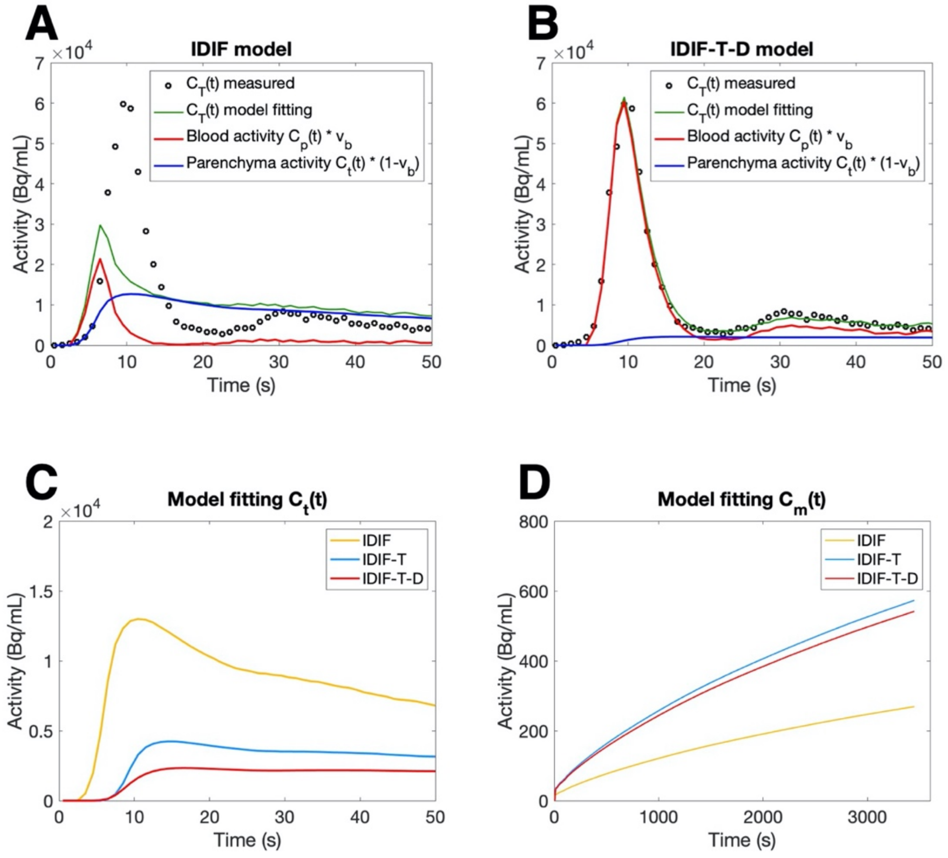

Figure 2.6. (A-B): the model fit of total activity $C_\mathrm{T}(t)$ is separated into the vascular component $v_\mathrm{b}(t)C_\mathrm{p}(t)$ and parenchyma component $(1-v_\mathrm{b})C_\mathrm{t}(t)$ for the conventional IDIF model (A) and the proposed IDIF-T-D model (B). (C-D): comparison of the predicted parenchyma TAC $C_\mathrm{t}(t)$ (C) and metabolized ^{18}F-FDG-6P TAC $C_\mathrm{m}(t)$ (D) by different models.

2.3.4. Identifiability of Kinetic Parameters

Table 2.3 shows the absolute value of relative bias and standard deviation of kinetic parameter estimates by different models. To clarify, this analysis is to study the robustness of models against random noise, while the systematic bias introduced by model oversimplification (e.g., neglecting the time delay effect) is not involved. The HTR IDIF model had a lower bias and standard deviation for K_1 and v_b along with worse K_i estimation than the LTR IDIF. Among the HTR cases, both IDIF-T-D and IDIF models

Table 2.3. Relative Bias (Absolute Value) and Standard Deviation of Kinetic Parameters in the Identifiability Study

Parameter	Kinetic model							
	IDIF, LTR		IDIF, HTR		IDIF-T, HTR		IDIF-T-D, HTR	
	Bias (%)	Std (%)	Bias (%)	Std (%)	Bias (%)	Std (%)	Bias (%)	Std (%)
K_1	4.0	9.3	1.3	2.4	6.2	6.4	1.4	13.6
v_b	0.8	6.3	0.5	4.8	1.6	2.7	0.1	2.3
K_i	0.9	4.9	2.4	8.6	4.9	5.4	0.4	6.2
t_RV	/	/	/	/	4.5	0.1	0.4	2.8
k_a	/	/	/	/	/	/	1.2	7.2

have a small bias (<2%) for K_1 quantification, while the standard deviation level of the IDIF-T-D (13.6%) was higher than the HTR IDIF model (2.4%). The proposed IDIF-T-D model achieved a low bias (<1%) and a low standard deviation (<3%) for quantifying v_b. For K_i, the IDIF-T-D had the bias (0.4%) and standard deviation (6.2%) levels that are comparable to the HTR IDIF model. The time delay and dispersion parameters t_RV and k_a had good identifiability.

2.3.5. Correlation with Age

Figure 2.7 shows the correlation plots between age and v_b estimated by different approaches. For comparison, the result by a traditional low temporal resolution protocol (10s/frame) is also included. Neither the v_b estimates by the low temporal resolution approach or by the HTR approaches without time delay and/or dispersion correction showed a statistically significant correlation with age (all P>0.1). In comparison, the v_b by the proposed IDIF-T-D model correlated with age with a statistical significance ($r^2 = 0.45$, and $P = 0.01$). The observed age-v_b relationship is consistent with the result

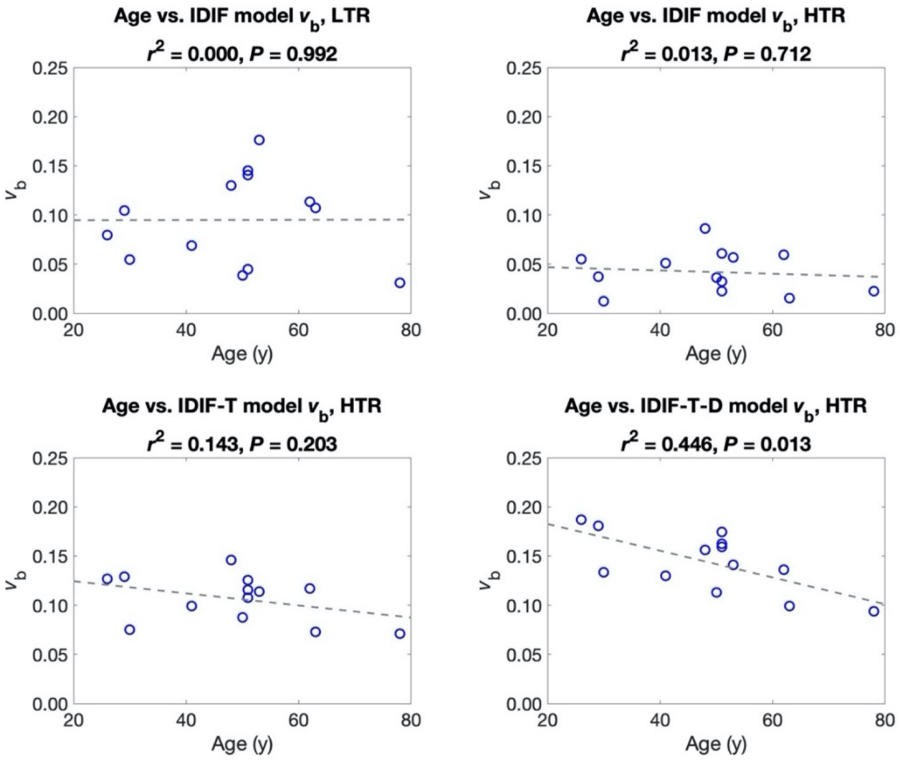

Figure 2.7. Correlation between subject age and v_{b} using the standard IDIF model with the 10s/frame low temporal resolution (LTR) (top left), the IDIF model with the 1s/frame high temporal resolution (HTR) (top right), the IDIF-T model with the HTR (bottom left), and the proposed model IDIF-T-D with the HTR (bottom right).

reported in previous studies (*138*,*139*) that shows aging is associated with decreased pulmonary blood volume. Neither age nor BMI correlated with other kinetic parameters.

2.3.6. Demonstration of Total-Lung Parametric Images

Figure 2.8A shows the total-lung SUV and multiparametric images using the proposed IDIF-T-D model for one subject. These images are overlaid on the corresponding CT image. The different parametric images demonstrate complementary spatial information. Figure 2.8B further shows the parametric images of v_{b} for one young subject (age 26 y) and one old subject (age 78 y). The lung v_{b} was much lower in this old subject, along with the

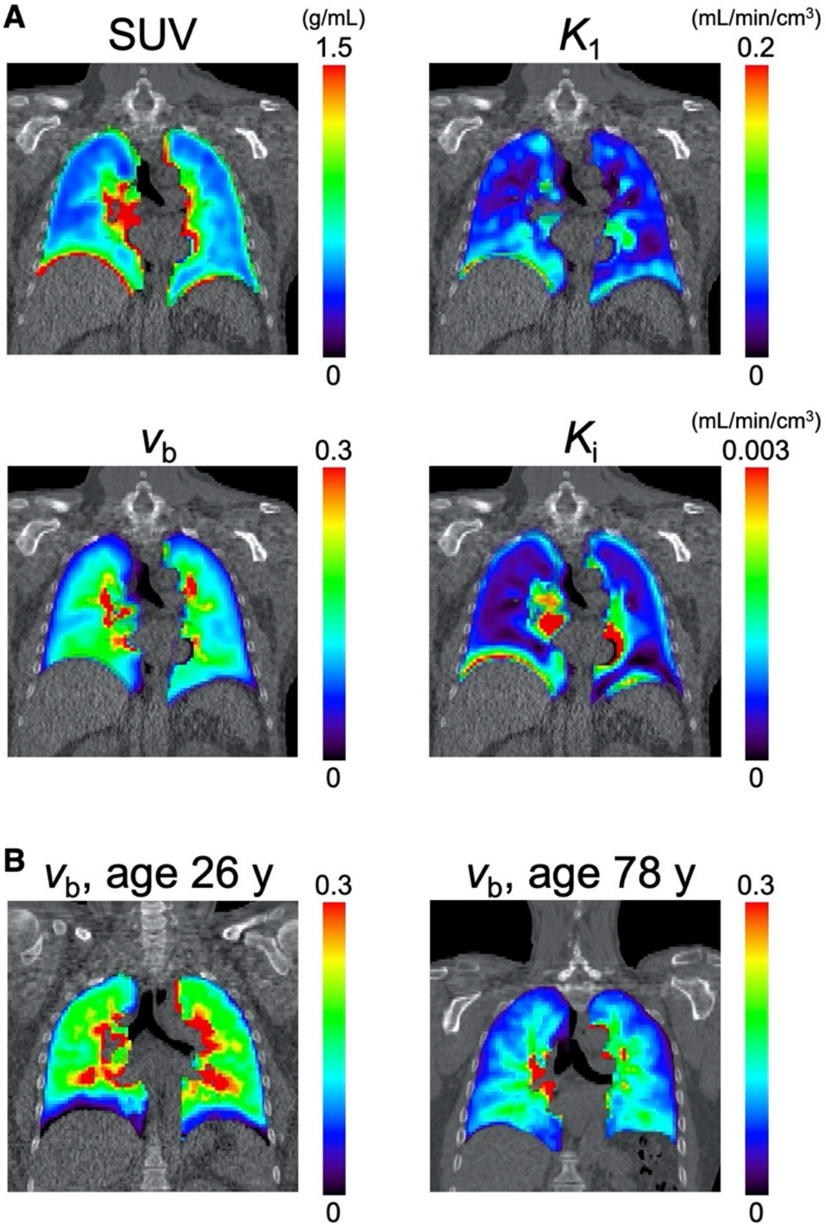

Figure 2.8. (A) ^{18}F-FDG PET images of the segmented lung for an example subject (#4): SUV image of 55-60 min, and multi-parametric images of ^{18}F-FDG delivery rate K_1, fractional blood volume v_b, and net influx rate K_i generated with the IDIF-T-D model. These images are superimposed on the corresponding CT images. (B) v_b images of a young subject (age 26 y, #3) and an old subject (age 78 y, #1).

increased age as compared to the young subject. We also noticed that in the parametric images generated by the IDIF-T-D model, the posterior part of the lungs has higher v_b than

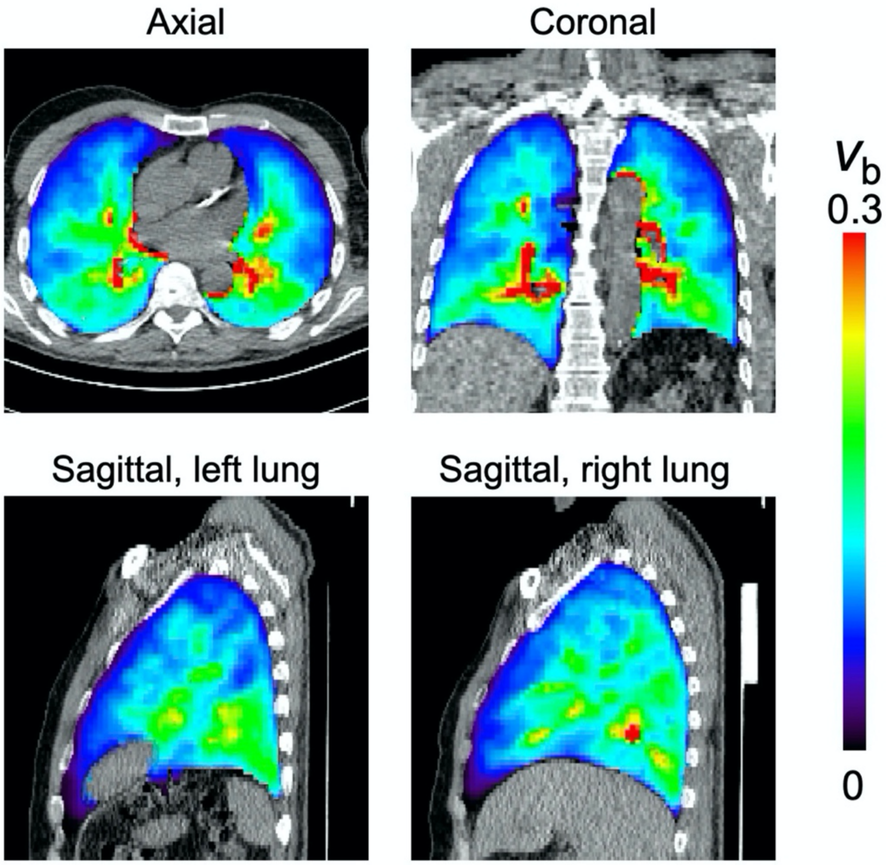

Figure 2.9. Parametric images of the fractional blood volume v_{b} generated with the proposed IDIF-T-D model for the lungs of one example subject. The images are overlaid on corresponding CT images.

the anterior part, and the posterior lung base has higher v_{b} than the apex (Figure 2.9), which are also within expectation (*140*).

2.4. Discussion

In this chapter, we studied the time delay and dispersion corrections to the IDIF for lung kinetic modeling with high temporal resolution. Traditionally, limited by the temporal resolution of dynamic PET imaging, these corrections were not taken into account in most existing studies of pulmonary ^{18}F-FDG kinetics (*104,125,141*) especially when the focus was on ^{18}F-FDG K_{i} (*104,113*), a macro parameter of which the estimation is dominated more by the late-phase dynamic data and is expected to be less sensitive to these corrections. However, a model without these corrections resulted in a poor fitting performance for the HTR data acquired with total-body PET (Figure 2.3A and 2.3C).

The proposed approaches to correcting time delay and dispersion for the IDIF led to much-improved lung TAC fitting (Figure 2.3A and 2.3B) with much lower AIC values (Table 2.1). Along with the improved fitting, the proposed modeling approaches had a significant impact on kinetic parameter quantification, especially for K_1 and v_b (Table 2.2). This can be explained as a result of an improved estimation of the vascular component in the fitted lung TACs (Figure 2.6). We also noted that the time delay t_RV tended to correlate with the inverse of the dispersion parameter k_a ($r = 0.44$, $P = 0.14$) in the proposed model, which is consistent with the expectation that a longer time delay (larger t_RV) is likely to be accompanied by a larger dispersion (smaller k_a). While the proposed model is more complex, the identifiability analysis results suggested the robustness of the proposed model to random noise (Table 2.3).

Although there is no ground truth, the v_b estimates by the proposed model are in general more consistent with the literature-reported pulmonary blood volume values and have led to an improved inverse correlation with age (Figure 2.7). This correlation aligns with previous findings of decreased pulmonary capillary blood volume with aging (*138*,*139*). The same correlation would be otherwise missed if the conventional IDIF models with or without time delay correction were used. Together with the improved TAC fit quality (Figure 2.3), our results here indicate the importance of simultaneous time delay

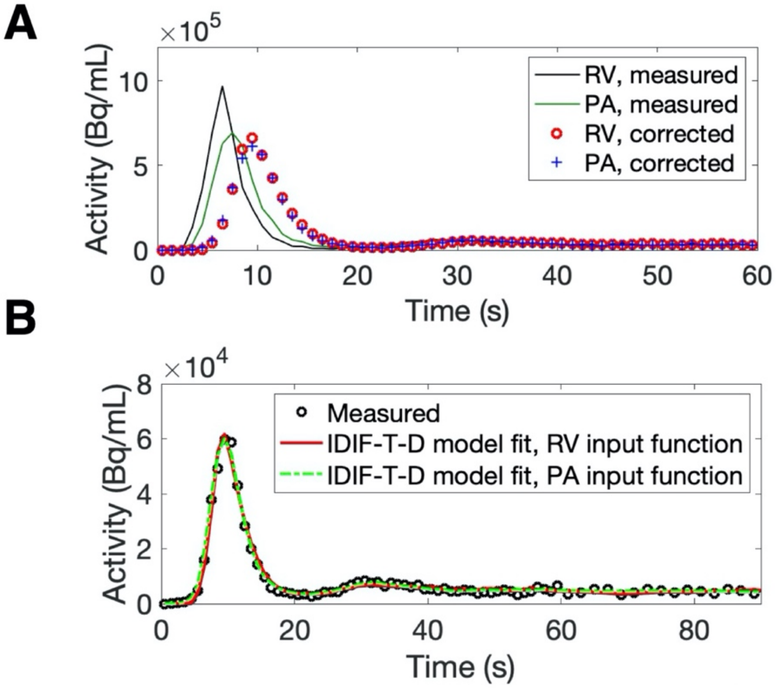

Figure 2.10. (A) The right ventricle (RV) and the pulmonary artery (PA) IDIFs before and after delay and dispersion corrections. The two input functions are similar after applying the corrections. (B) Lung TAC fitting with the IDIF-T-D model using the RV input function and the PA input function. Both input functions can fit the lung TAC well.

and dispersion corrections as compared to no correction or time delay correction only (Figure 2.7).

It is worth noting that a simultaneous correction for time delay and dispersion was explored previously in dynamic brain PET studies (*124*). However, the method cannot be directly applied in our work on lung kinetic modeling. This is because the prior study tackled a backward dispersion correction problem that removes dispersion from the measured input function (e.g., from the radial artery), while this chapter focuses on a forward dispersion correction problem that adds dispersion to the measured IDIF for

Table 2.4 Lung ^{18}F-FDG Kinetic Quantification with the IDIF-T-D Model Using Different Combinations of IDIFs and Lung ROIs

Input function	Tissue TAC	K_1 (mL/min/cm^3)	K_i (mL/min/cm^3)	v_b	t_d (s)	k_a(/min)
RV	total lungs	0.038	0.00057	0.094	2.2	34
PA	total lungs	0.043	0.00052	0.100	1.5	55
LPA	left lung	0.041	0.00059	0.102	1.5	47
RPA	right lung	0.045	0.00048	0.100	1.7	59

t_d is the time delay correction parameter, which functions the same as t_RV for the time-delay correction to the right ventricle (RV) input function. Compared with the RV input function, the use of the pulmonary artery (PA) input function resulted in a smaller extent of the time delay correction (as indicated by the smaller time delay parameter t_d), and a smaller extent of the dispersion correction (as indicated by the larger dispersion parameter k_a), both within expectations. The difference in K_1, v_b, and K_i between RV and PA is acceptable and is likely caused by the partial volume effect of the PA. IDIFs derived from the left pulmonary artery (LPA) and right pulmonary artery (RPA) can be used separately for the kinetic modeling of the individual lungs.

modeling the actual blood input. The latter approach is developed in response to the availability of IDIF in total-body HTR dynamic PET imaging.

In addition to the use of the right ventricle for deriving the IDIF, the region of pulmonary arteries (PA) may be used directly for their closer location to the lung tissues. Similar results were obtained by using the PA as the input function compared with using the RV, including the input function after corrections (Figure 2.10A), lung TAC fitting (Figure 2.10B), and kinetic parameter quantification (Table 2.4), confirming the benefits of time delay and dispersion corrections. The IDIFs from the left pulmonary artery and the right pulmonary artery can also be used for the kinetic modeling of individual lungs (Table 2.4). However, the use of pulmonary arteries for IDIF needs to be more careful because the smaller size may make the ROI placement more challenging to reduce the partial volume effect.

Our study in this chapter has several limitations. First, the sample size is relatively small as the thirteen healthy subjects vary in age and body weight. Second, subject motion can affect the kinetic quantification results (*142*). We made effort to minimize the motion effect by carefully placing the ventricular ROIs to reduce the partial volume effect of the myocardium. We also drew five ROIs in the lung lobes and extracted the global lung TAC to decrease the respiratory motion effect and avoid partial volume effect from the liver. Third, the air fraction in the lungs may affect the absolute quantification of K_1 and K_i (*117*,*126*,*143*) but the correction is not included here. It, however, does not influence the comparison of kinetic models because this tissue-fraction effect only introduces a scaling factor on K_1 and K_i and can be corrected after kinetic modeling.

Our subsequent research will include a larger subject cohort and apply the method to study lung diseases, such as coronavirus disease 2019. The kinetic quantification approach can be also used to assess the lungs in other systemic diseases, e.g., cancer and nonalcoholic fatty liver disease. Motion correction and air fraction correction will be implemented to optimize the HTR kinetic modeling and parameter estimation further. Another direction is to model the dual-blood input function to account for the fraction of tracer delivery from the bronchial circulation (*83*). This dual-input effect may be small in healthy lung tissues but can be significant in lung tumors (*91*), which will be explored in Chapter 3.

2.5. Conclusion

We studied lung kinetic modeling for high temporal resolution dynamic PET imaging on the uEXPLORER total-body PET/CT system. Direct application of the standard IDIF model resulted in poor TAC fitting. We developed an approach to jointly correcting the effects of time delay and dispersion in the IDIF. The proposed model greatly improved TAC fitting and had a large impact on lung kinetic quantification. It also improved the correlation of fractional blood volume with age. Total-body HTR dynamic PET has the potential to be a sensitive tool for studying healthy lungs and lung diseases.

Chapter 3. High-Temporal Resolution Kinetic Modeling of Lung Tumors with Dual-Blood Input Function Using Total-Body Dynamic PET.

3.1. Introduction

The lungs have two blood supplies: the pulmonary arteries that carry deoxygenated blood originating from the right ventricle (RV) (*81*,*82*) and the bronchial arteries that carry oxygenated blood downstream from the left ventricle (LV) (*83–85*). While the blood supply to normal lung tissue is usually dominated by the pulmonary arteries, lung tumors tend to have an increased blood supply fraction from the bronchial arteries (*89–91*). This dual-blood supply effect of lung tumors has been studied with dynamic computed tomography (CT) imaging (*91*,*144–146*), though with a limited axial field of view. However, to our best knowledge, it has never been investigated by dynamic positron emission tomography (PET), partially because the temporal resolution of conventional dynamic PET imaging (*53*,*114*,*130*) was limited (5-30 s/frame), and not able to detect the rapidly-changing early dynamics of the lungs and differentiate the dual blood supplies. As a result, existing lung kinetic modeling approaches for dynamic PET often neglect the effect of dual blood supply and only use a single input function for kinetic modeling (*104*,*125*,*130*,*131*).

Total-body and long axial field-of-view (FOV) PET scanners (*78*,*147*,*148*) greatly improve the detection sensitivity and hence permit high temporal-resolution (HTR) dynamic imaging, opening the door for HTR kinetic modeling for the lungs. For example, the uEXPLORER total-body PET/CT scanner allows HTR dynamic PET imaging with 1 s or less per frame (*120*,*121*). In this study, we exploit the ability of uEXPLORER for HTR dynamic PET imaging to model the dual-blood input function (DBIF) in the lungs and investigate its impact on the kinetic quantification of normal lung tissue and lung tumors.

3.2. Materials and Methods

3.2.1. High-Temporal Resolution Dynamic Data Acquisition on Total-Body PET

This study included thirteen healthy human subjects (age 49 ± 15 y, weight 82 ± 18 kg, six males, seven females) and six cancer patients with lung tumors, which include three primary lung cancer subjects (age 68 ± 3 y, weight 78 ± 8 kg, two males, one female), and three genitourinary cancer subjects with lung metastases (age 64 ± 10 y, weight 79 ± 10 kg, three males). All subjects have been consented with the approval of the Institutional Review Board at the University of California, Davis. The subjects were scanned on the uEXPLORER total-body PET/CT system (United Imaging Healthcare) (*128*) with an ultralow-dose (140 kVp, 5 mAs) or low-dose (140 kVp, 50 mAs) CT scan performed first, followed by a 60-minute total-body dynamic ^{18}F-FDG PET scan with a dose of ~360 MBq through intravenous administration. The acquired list-mode PET data were reconstructed into a total of 120 frames over 60 minutes with HTR frames (1-2 s per frame) in the early phase: $60 \times 1\ \mathrm{s}, 30 \times 2\ \mathrm{s}, 6 \times 10\ \mathrm{s}, 6 \times 30\ \mathrm{s}, 12 \times 120\ \mathrm{s}, 6 \times 300\ \mathrm{s}$ using the vendor-provided ordered subset expectation maximization algorithm (four iterations, and 20 subsets) with $4 \times 4 \times 4\ \mathrm{mm}^3$ voxels. Regions of interest (ROIs) were placed in the LV

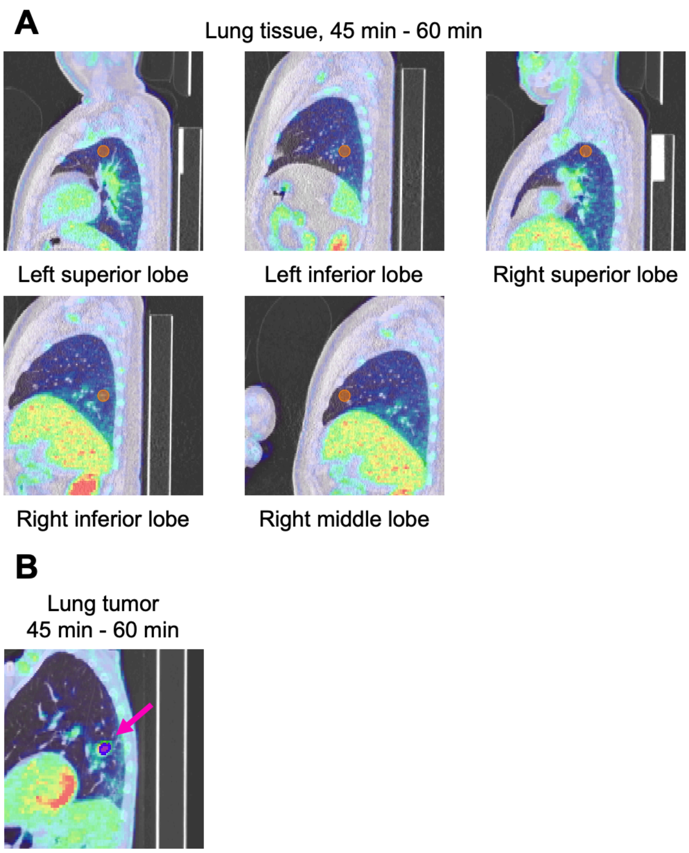

Figure 3.1. Example ROI placement on the lung lobes for normal lung tissue (A) and a lung tumor (B).

cavity and RV cavity for each subject to extract time-activity curves (TACs) for image-derived input functions (IDIFs), $C_{\mathrm{LV}}(t)$ and $C_{\mathrm{RV}}(t)$, which provide the bronchial blood supply and pulmonary blood supply to the lungs, respectively. TACs of normal lung tissue were extracted for each of the thirteen healthy subjects by placing one ROI in each of the five lung lobes (see Figure 3.1A for an illustrative example). These lung TACs were then averaged into a global lung tissue TAC for each subject. A total of eight lung tumors, including three primary lung tumors (from each of the three primary lung cancer subjects) and five lung metastases (three from one genitourinary cancer subject, two from each of the other two genitourinary cancer subjects), were also identified among the six cancer

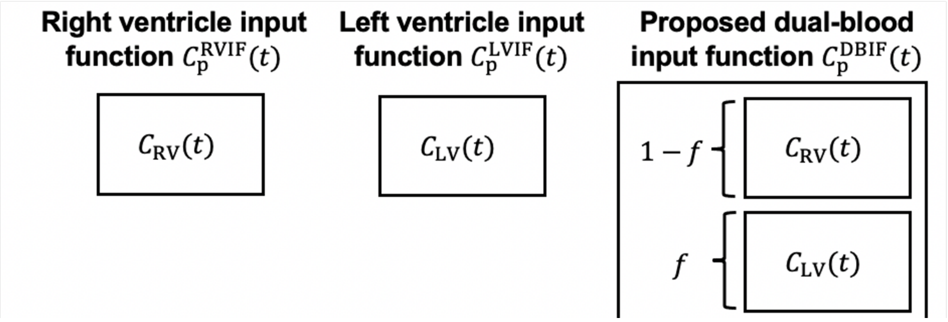

Figure 3.2. Different blood input functions for the high-temporal resolution lung kinetic modeling. Time delay and dispersion corrections are applied to the three input functions.

subjects. ROIs of these lung tumors were placed (Figure 3.1B), and corresponding TACs were extracted.

3.2.2. Compartmental Modeling

We used a two-tissue irreversible (2Ti) compartmental model (*2,113*) to model the ^{18}F-FDG kinetics in the lungs (Figure 1.6B). The model is described in Section 1.4 and follows Eqs. 1.6 - 1.9. All kinetic parameters are jointly estimated using a non-linear least-square TAC fitting as described by Eq. 1.11 (*69*).

3.2.3. Single-input Input Functions

Because the pulmonary input accounts for most of the total blood input to the lung tissue (*84*), previous studies (*104,125,130,131*) commonly used the RV-derived input function (RVIF) (Figure 3.2) for kinetic modeling of lung tissue. In HTR lung kinetic modeling, we have shown in Chapter 2 (published as (*149*)) that it becomes important to include corrections for time delay and dispersion to the IDIF. Hence, the RVIF model in this chapter has a similar format as Eq. 2.4 and is as follows:

$$C_\mathrm{p}^\mathrm{RVIF}(t) = C_\mathrm{RV}(t - t_\mathrm{RV}) \otimes k_\mathrm{d} \exp(-k_\mathrm{d} t), \qquad \text{Eq. 3.1}$$

where the time delay parameter t_{RV} (s) denotes the time delay between the RV where the IDIF is extracted and the arrival of the radiotracer in the tissue of interest. The dispersion parameter k_{d} (min^{-1}) aims to adaptively correct the dispersion effect between the two sites. The parameters t_{RV} and k_{d} are jointly estimated with other kinetic parameters during TAC fitting. $C_{\mathrm{wb}}^{\mathrm{RVIF}}(t)$ is modeled with the same formula as Eq. 3.1.

On the other hand, an LV-derived input function (LVIF) is typically used for modeling lung tumors (*150,116,59*). The model supposes that the bronchial arteries, which are downstream from the left ventricle (LV), are the dominant blood supply of the tissue of interest. Similar to the RVIF model, the LVIF model (Figure 3.2) to be compared in this work is:

$$C_{\mathrm{p}}^{\mathrm{LVIF}}(t) = C_{\mathrm{LV}}(t - t_{\mathrm{LV}}) \otimes k_{\mathrm{d}} \exp{(-k_{\mathrm{d}} t)}, \qquad \text{Eq. 3.2}$$

where t_{LV}(s) denotes the time delay between the LV and the arrival of the radiotracer in the tissue of interest, and k_{d} (min^{-1}) is for the dispersion correction. $C_{\mathrm{wb}}^{\mathrm{LVIF}}(t)$ is also modeled with Eq. 3.2.

3.2.4. Proposed Dual Blood Input Function (DBIF)

In this work, we hypothesize that the contribution of each blood supply is nonnegligible and should be accounted for when analyzing HTR PET data and hence propose modeling both supplies rather than omitting either of them. The proposed DBIF is a linear combination of the two image-derived input functions $C_{\mathrm{RV}}(t)$ and $C_{\mathrm{LV}}(t)$ (Figure 3.2):

$$C_{\mathrm{p}}^{\mathrm{DBIF}}(t) = [f C_{\mathrm{LV}}(t - t_{\mathrm{LV}}) + (1 - f) C_{\mathrm{RV}}(t - t_{\mathrm{RV}})] \otimes k_{\mathrm{d}} \exp{(-k_{\mathrm{d}} t)}, \text{ Eq. 3.3}$$

where f represents the fractional contribution from the bronchial blood supply. As in the RVIF and LVIF models, t_{LV} and t_{RV} are the time delays for each of the two blood supplies and k_{d} is the dispersion parameter. This setting of two separated time-delay parameters and one comprehensive dispersion parameter was selected based on our initial studies of curve fitting and parameter quantification. Again, all parameters are jointly estimate with other kinetic parameters through TAC fitting. The DBIF model is equivalent to the RVIF model if $f = 0$ and the LVIF model if $f = 1$. $C_{\mathrm{wb}}^{\mathrm{DBIF}}(t)$ is also modeled with Eq. 3.3.

With this DBIF model, a tissue TAC $C_{\mathrm{T}}(t)$ can be decomposed into an LV-supplied component $C_{\mathrm{T}}^{\mathrm{LV}}(t)$ and an RV-supplied component $C_{\mathrm{T}}^{\mathrm{RV}}(t)$:

$$C_{\mathrm{T}}(t) = C_{\mathrm{T}}^{\mathrm{LV}}(t) + C_{\mathrm{T}}^{\mathrm{RV}}(t), \qquad \text{Eq. 3.4}$$

where the decomposed TACs are calculated by

$$C_{\mathrm{T}}^{\mathrm{LV}}(t) = f\left((1 - v_{\mathrm{b}})H(t; \boldsymbol{\kappa}) \otimes C_{\mathrm{p}}^{\mathrm{LVIF}}(t) + v_{\mathrm{b}} C_{\mathrm{p}}^{\mathrm{LVIF}}(t)\right), \quad \text{Eq. 3.5}$$

$$C_{\mathrm{T}}^{\mathrm{RV}}(t) = (1 - f)\left((1 - v_{\mathrm{b}})H(t; \boldsymbol{\kappa}) \otimes C_{\mathrm{p}}^{\mathrm{RVIF}}(t) + v_{\mathrm{b}} C_{\mathrm{p}}^{\mathrm{RVIF}}(t)\right), \text{Eq. 3.6}$$

with $C_{\mathrm{p}}^{\mathrm{LVIF}}(t)$ and $C_{\mathrm{p}}^{\mathrm{RVIF}}(t)$ given by Eq. 3.2 and Eq. 3.1, respectively.

3.2.5. Evaluation of Statistical Fit Quality

To assess the statistical fitting quality of the three models (RVIF, LVIF, and DBIF), the Akaike information criterion (AIC) (Eq. 2.5) was used *(133,151)*. AIC values of the three models (LVIF, RVIF, and DBIF) were compared to quantify any improvement in fitting quality by the proposed DBIF model.

3.2.6. Impact on Kinetic Quantification

The impact of the DBIF model was evaluated for quantification of kinetic parameters of major interest, including ^{18}F-FDG delivery rate K_1, ^{18}F-FDG net influx rate K_i (calculated with Eq. 1.10), fractional blood volume v_b, and the time delay parameters t_LV and t_RV. The LV fraction f, uniquely estimated by the DBIF model, was also investigated. Further, we compared the statistical difference between the normal lung tissue group and the lung tumor group using the Mann-Whitney U test of the kinetic parameters quantified by different models. A p-value < 0.05 was considered to be significant.

3.2.7. Demonstration of Multiparametric Imaging using the DBIF Model

In addition to the ROI-based analysis, we applied the proposed DBIF model for voxel-wise parametric imaging to acquire multiparametric images of lung K_1, K_i, v_b, and f. Kernel smoothing was applied to the dynamic images for the purpose of noise reduction (*69*).

As shown by Eq. 3.4, one property of the DBIF model is to separate the LV-supplied and RV-supplied components. Therefore, we also used the decomposition to generate dynamic lung activity images showing the supply by the individual LVIF and RVIF.

3.3. Results

3.3.1. High-Temporal Resolution Dynamic Images of Subjects with Lung Tumors

Figure 3.3A shows the HTR total-body dynamic images of one representative cancer subject with lung metastasis in maximum intensity projections, and Figure 3.3B shows the corresponding ROI TACs extracted from the images. After the intravenous administration

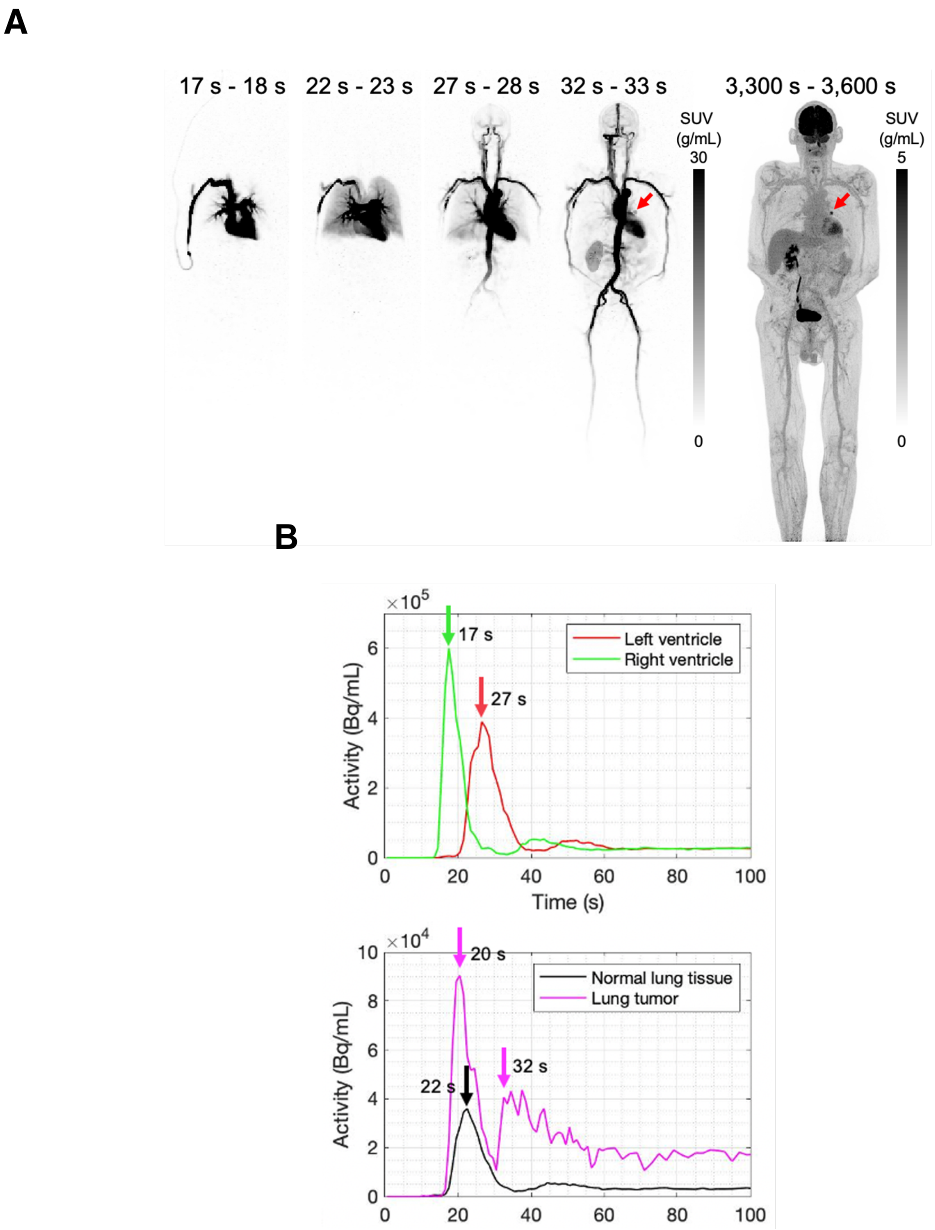

Figure 3.3. (A) High temporal resolution (HTR) total-body ^{18}F-FDG dynamic images of a cancer subject with lung metastasis acquired with the uEXPLORER PET/CT system. Red arrows point to the lesion. (B) HTR time-activity curves (TACs) extracted from the dynamic image set.

at around 10 s, the tracer traveled through the right ventricle (Figure 3.3A, 17 s - 18 s) and arrived at the lungs (Figure 3.3A, 22 s - 23 s) through the pulmonary artery. The tracer then flowed into the left ventricle (Figure 3.3A, 27 s - 28 s) through the pulmonary vein. Hence, the arrival order of the early phase TAC peak is RV (at ~17 s), lung tissue (at ~22 s), and

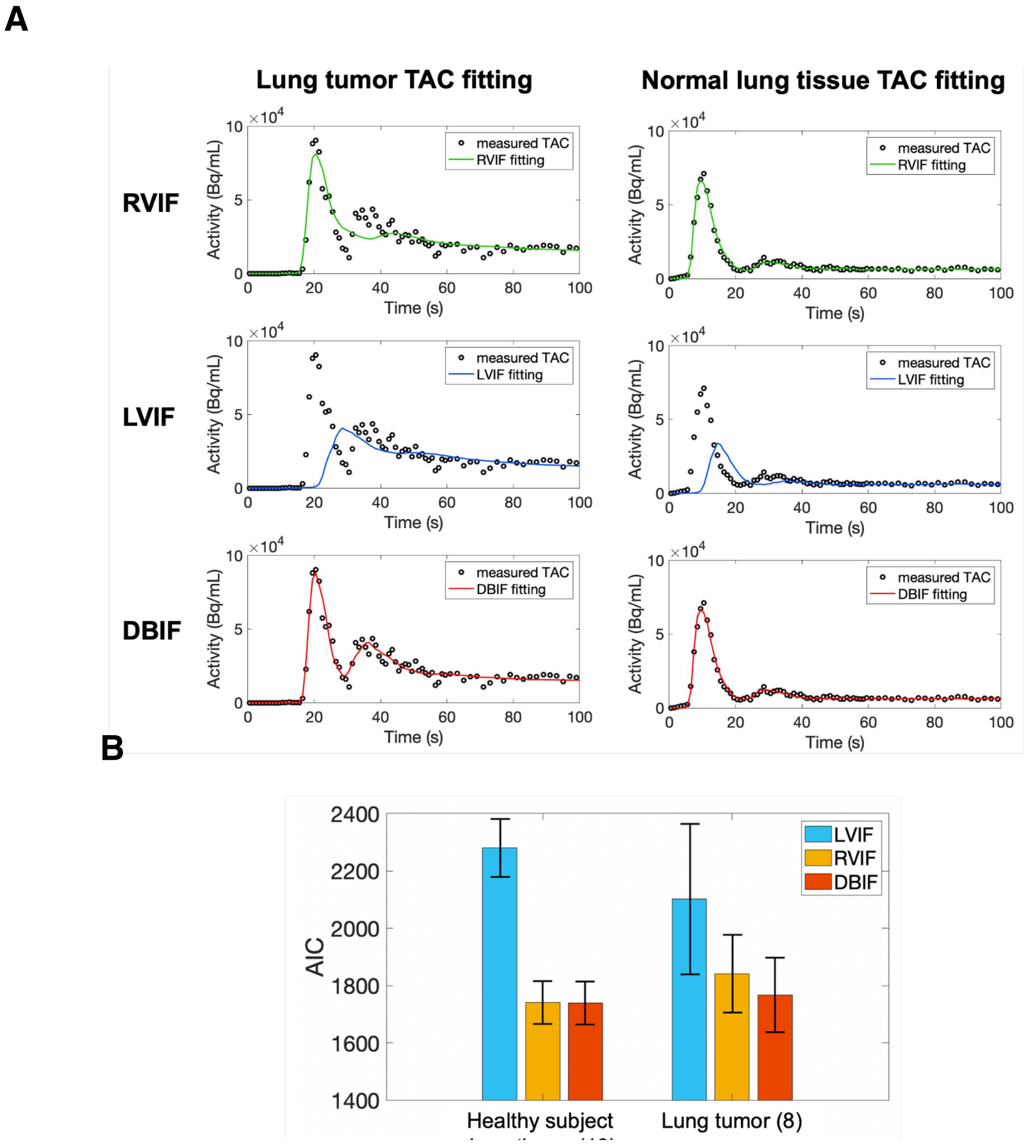

Figure 3.4. (A) High temporal resolution TAC fitting of the lung tumor from a cancer subject (left column) and the normal lung tissue from a healthy subject (right column) with the three models RVIF (top), LVIF (middle), and DBIF (bottom). (B) Akaike Information Criterion (AIC) of the RVIF, LVIF models and the proposed DBIF model in the normal lung tissue group and the lung tumor group. A lower value indicates better fitting quality.

LV (at ~27 s), as seen in Figure 3.3B. However, the lung tumor TAC had a first peak at ~20 s and a second peak at ~32 s (also visible in Figure 3.3A), and the latter is later than the LV peak. This observation suggests a dual blood supply effect in the lung tumor.

Table 3.1. AIC Value of Normal Lung Tissue and Lung Tumor TAC Fitting by Kinetic Models with Different Input Functions.

Model	AIC	
	Normal lung tissue (13)	Tumor (8)
LVIF	2280.4±101.1	2101.6±262.5
RVIF	1741.0±74.7	1841.6±135.6
DBIF	1739.1±75.1	1767.5±130.1

3.3.2. TAC Fitting Using Different Input Function Models

Figure 3.4A shows examples of fitting the TACs of one lung tumor from a cancer subject and one normal lung tissue from a healthy subject by the two single-input models (RVIF and LVIF) and the DBIF model. For the tumor TAC, neither the RVIF nor the LVIF model was able to fit the two peaks in the early phase. However, the DBIF model achieved better fitting. The normal lung tissue TAC fitting by the LVIF model was poor, while the RVIF and DBIF had similar results. The TAC fitting quality is further evaluated by AIC in Table 3.1 and Figure 3.4B. For healthy lung tissue, the AIC of the RVIF model was much lower than the LVIF model, confirming the appropriateness of using RVIF for modeling lung tissue. A better AIC by RVIF than LVIF was also observed for lung tumors, though the improvement was at a slightly lesser level. Compared to RVIF, the DBIF model achieved a better AIC, especially for the modeling of lung tumor TACs.

For an illustrative example, the TACs of the normal lung tissue from a healthy subject and the lung tumor from a cancer subject (Figure 3.4A) were further decomposed in Figure 3.5 according to the individual LV and RV blood supplies using Eq. 3.4. In the normal lung tissue, the LV-supplied component (the red curve) was small with $f = 0.045$. In

Normal lung tissue, $f = 0.045$

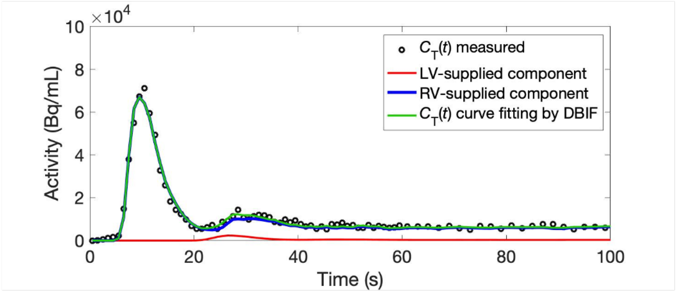

Lung tumor, $f = 0.31$

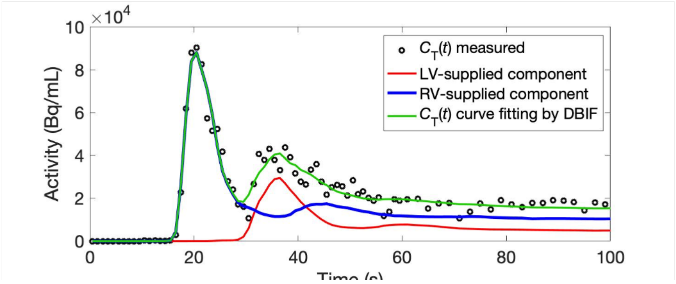

Figure 3.5. Examples of the decomposition of a fitted TAC into the LV-supplied component and RV-supplied component in the DBIF model for a normal lung tissue TAC from a healthy subject and a lung tumor TAC from a cancer subject.

comparison, for the tumor TAC, the LV-supplied component contributed significantly to fitting the second peak (~35 s) with $f = 0.31$.

3.3.3. Statistical Analysis of Estimated *f* in Lung Tissue and Tumors

Figure 3.6A compares the LV fraction *f* of the DBIF model in normal lung tissue and lung tumor groups. Note that *f* is assumed to be 0 by the RVIF model and 1 by the LVIF model for both normal lung tissue and lung tumors. The estimation of *f* by DBIF was 0.037±0.013 for normal lung tissue and 0.30±0.27 for lung tumors. A statistical U test indicated a significant difference (p<0.0003) between the two groups.

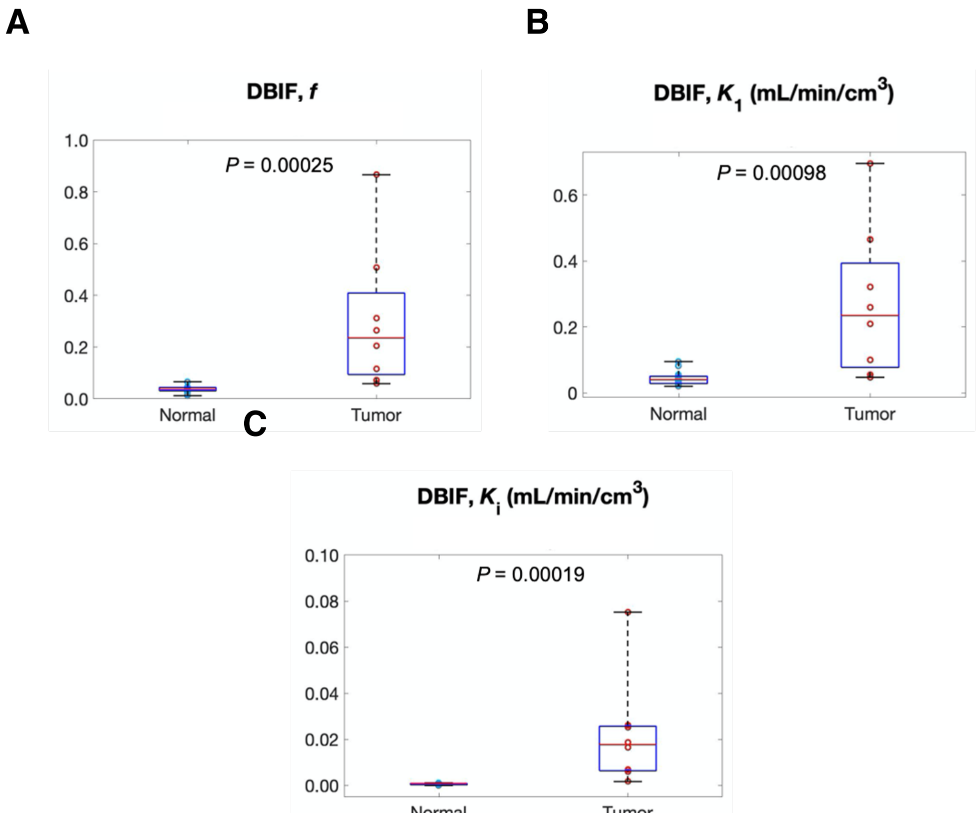

Figure 3.6. Comparison of lung tumors and normal lung tissue using kinetic parameters estimated by the proposed DBIF model. (A) left ventricle fraction f, (B) ^{18}F-FDG delivery rate K_1, and (C) ^{18}F- FDG net influx rate K_i. P-values of the Mann-Whitney U test are labeled.

3.3.4. Impact of DBIF on Kinetic Quantification

The difference in f led to changes in the estimation of kinetic parameters of interest, as shown in Table 3.2. Compared to the two single-input models (RVIF and LVIF), the DBIF resulted in higher v_b and lower K_1 in both normal lung tissue and lung tumors. Particularly, the v_b estimated by DBIF for lung tissue was closer to the reference value of 0.16 as reported in the literature (*113*).

Figure 3.6B and Figure 3.6C further compare K_1 and K_i of the DBIF model for differentiating lung tumors from normal lung tissue. Both kinetic parameters showed a

Table 3.2. Comparison of Normal Lung Tissue with Lung Tumors using ^{18}F-FDG K_1, v_b, K_i, t_RV, and t_LV estimated by Kinetic Models with Different Input Functions. P values for the Mann-Whitney U Test are included.

Parameter	Model	Lung Tissue (13)	Lung Tumor (8)	P value
K_1 (mL/min /cm^3)	RVIF	0.065±0.030	0.33±0.33	0.013
	LVIF	0.053±0.028	0.42±0.37	0.00034
	DBIF	0.044±0.022	0.27±0.22	0.00098
v_b	RVIF	0.143±0.029	0.18±0.10	0.86
	LVIF	0.101±0.029	0.14±0.12	0.74
	DBIF	0.151±0.032	0.21±0.10	0.23
K_i (mL/min /cm^3)	RVIF	0.00076±0.00047	0.022±0.024	0.00019
	LVIF	0.00007±0.00014	0.020±0.024	0.00098
	DBIF	0.00061±0.00034	0.022±0.023	0.00019
t_RV (s)	RVIF	2.16+0.38	2.3+3.3	0.14
	LVIF	/	/	/
	DBIF	2.17+0.35	1.3+0.9	0.039
t_LV (s)	RVIF	/	/	/
	LVIF	0+0	0.4+1.1	0.24
	DBIF	13.0+3.0	5.5+5.7	0.0042

statistical group difference (p<0.001). The comparison between the DBIF and single-input models is summarized in Table 3.2. The RVIF model had a poorer performance than DBIF and LVIF for using K_1 to differentiate lung tumors, while the LVIF model had a smaller power than DBIF and RVIF for using K_i to differentiate tumors, as indicated by the p values. In addition, t_RV and t_LV by the DBIF tend to be different between lung tissue and lung tumors. Overall, the DBIF demonstrated a more robust differentiation performance.

3.3.5. Demonstration of Multiparametric Imaging

Figure 3.7 shows the parametric images (f, K_1, K_i, and v_b) of the lungs of a subject by the DBIF model as compared to the image of the standardized uptake value. The parametric

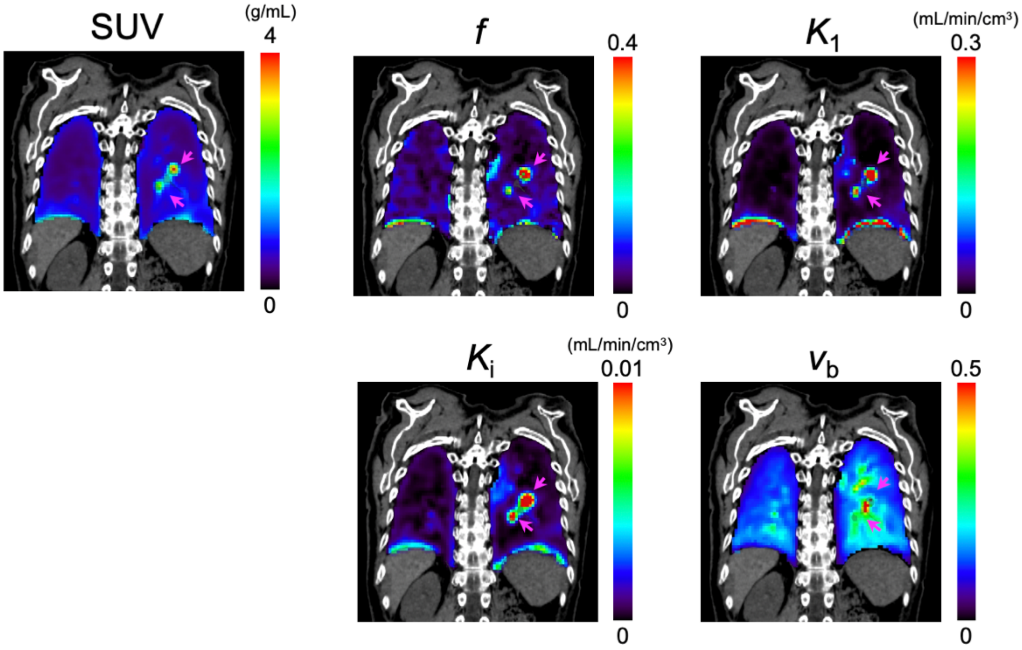

Figure 3.7. Comparison of lung ^{18}F-FDG SUV image and parametric images for a cancer subject with lung metastasis (magenta arrows). The parametric images include LV fraction f, ^{18}F-FDG delivery rate K_1, ^{18}F-FDG net influx rate K_i, and fractional blood volume v_b generated by the proposed DBIF model. The PET images are overlaid on the corresponding CT slice.

images show a clear difference in the lung tumors and surrounding tissue, confirming the ROI-based analysis.

Figure 3.8 shows the decomposition of the dynamic images into the LV-supplied and RV-supplied components for one subject. When the tracer first passed through the lung via the pulmonary artery at 20 s – 22 s (Figure 3.3B), the measured activity was all in the RV-supplied component, and there was no LV-related component (Figure 3.8, left column). However, when the second peak of the tumor TAC appears at 32 s – 34 s (Figure 3.8, middle column), the LV-supplied component appeared in the tumors (arrowheads) and was the dominant contribution to the total measured activity in those tumors. The LV-supplied

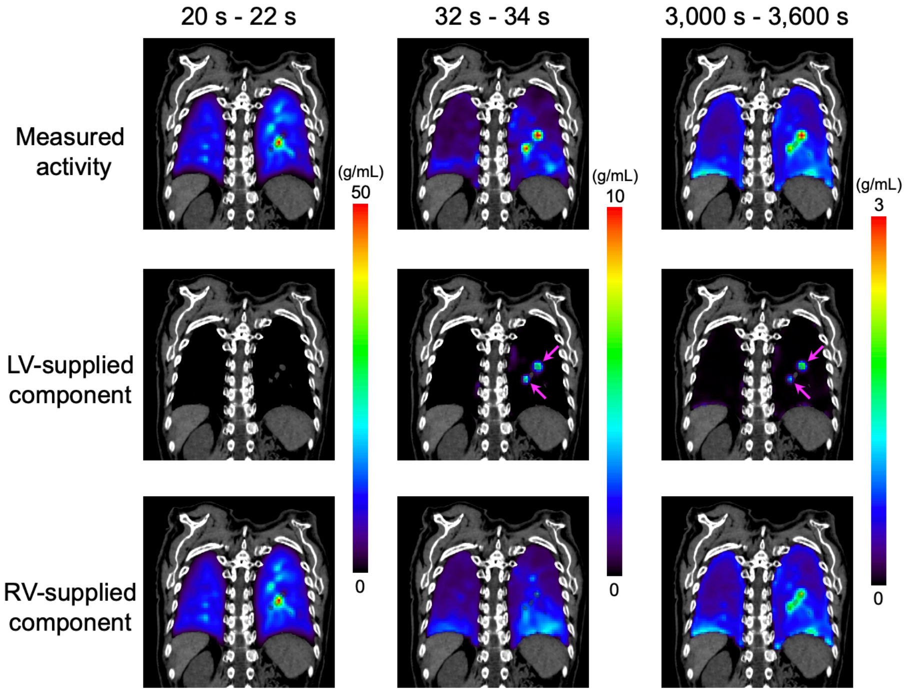

Figure 3.8. Dynamic ^{18}F-FDG images of a cancer subject with lung metastases (top) were decomposed into the LV-supplied component (middle) and the RV-supplied component (bottom) using the DBIF model. The ^{18}F-FDG PET images are overlaid on the corresponding CT slice, and the arrows point at metastases.

component continued to contribute to the total activity until the late phase of the one-hour scan (Figure 3.8, right column).

3.4. Discussion

In this study, we investigated DBIF in normal lung tissue and lung tumors using high-temporal resolution dynamic ^{18}F-FDG imaging enabled with a total-body PET scanner. To the best of our knowledge, this is the first time that the dual blood supply of the lung tumor was monitored using dynamic PET and modeled by kinetic modeling. It is also worth noting that the DBIF model is not limited to dynamic ^{18}F-FDG PET but also lung studies with other tracers, e.g., perfusion tracers such as $H_2{}^{15}O$ or ^{11}C-butanol (*152*).

The significance of DBIF was demonstrated for HTR lung kinetic modeling by comparing the DBIF model with single-input models (i.e., LVIF and RVIF). The DBIF model achieved the best AIC for TAC fitting, especially for tumor TACs, while the LVIF and the RVIF were not able to provide good fitting (Figure 3.4).

The DBIF model had a significant impact on kinetic parameter quantification and improved the performance for differentiating lung tumors from normal lung tissue using ^{18}F-FDG delivery rate K_1 and net influx rate K_i (Figure 3.6 and Table 3.2). It also led to v_b values more consistent with the literature. More notably, the DBIF model also provides for estimation of the fraction of the bronchial supply (i.e., f) and the fraction of pulmonary supply (i.e., $1 - f$), which were significantly different in lung tumors and normal lung tissue (Figure 3.6A). The potential applications of f are not limited to lung cancer but also other lung diseases for which the quantification of bronchial blood supply is crucial, such as asthma (*153*), acute lung inflammation (*83*), and coronavirus disease 2019 (*154*).

In the proposed DBIF model, the same dispersion parameter k_d was used to account for the dispersion effects in both blood supplies. This choice was selected based on its comparison with multiple other options, including (1) no dispersion correction, (2) dispersion correction for the LVIF only, (3) dispersion correction for the RVIF only, and (4) two different dispersion corrections for the LVIF and RVIF respectively. The shared dispersion correction provided the most robust and physiologically reasonable results in the comparison (results not shown). It is also worth noting that the lung DBIF model proposed in this study is mathematically and physiologically different from the DBIF model used for liver PET studies (*93,155*) that consider the dual blood supplies from the hepatic artery and portal vein.

This work has some limitations. Primary lung tumors and lung metastases were pooled together for statistical analysis due to the limited sample size. It is possible that the dual blood input effect was different in primary lung cancer ($f = 0.35 \pm 0.45$) and lung metastases ($f = 0.27 \pm 0.16$). It would be valuable to further subtype the tumor group in future investigations. The proposed DBIF model involves two more parameters (f and t_{LV}). We also tested using a single time delay for both LVIF and RVIF in the DBIF model. However, the result (not shown) suggests the need for different time delays for the two input functions. While the new model has increased complexity, its benefits were demonstrated by TAC fitting quality and the impact on the quantification of kinetic parameters of interest. Our future work will further explore the potential of these kinetic parameters (e.g., K_1 and f) as disease biomarkers.

3.5. Conclusion

The effect of modeling lung dual-blood supply was demonstrated using high-temporal resolution dynamic total-body PET. The proposed DBIF model improved TAC fitting quality and led to a better differentiation of lung tumors from lung tissue. The DBIF effect was higher in lung tumors than in normal lung tissue. HTR dynamic imaging with total-body PET has the potential to be a sensitive tool for investigating lung physiology and diseases.

Chapter 4. Total-Body Multiparametric PET Quantification of ^{18}F-FDG Delivery and Metabolism in the Study of COVID-19 Recovery

4.1. Introduction

Positron emission tomography (PET) with the radiotracer ^{18}F-fluorodeoxyglucose (^{18}F-FDG) is a non-invasive *in vivo* molecular imaging technique that reflects glucose metabolism. Conventional whole-body static ^{18}F-FDG PET imaging can provide an overall evaluation of glucose utilization throughout the body, but it mixes the specific glucose transport and metabolic steps. Identification and quantification of these specific processes separately require a fast dynamic scanning protocol, which is however limited to a single organ or a confined region by a short axial field-of-view PET scanner. The advent of total-body PET/CT systems such as uEXPLORER (*78*) and other long-axial field-of-view PET scanners (*147*,*148*) has brought new opportunities for total-body dynamic PET imaging with increased detection sensitivity and simultaneous dynamic imaging of multiple organs (*156*). Combined with tracer kinetic modeling (*72*), total-body dynamic ^{18}F-FDG-PET enables a multiparametric quantification method (*69*) that allows quantitative measurement of not only overall glucose utilization, but also the microparametric rates of glucose delivery and phosphorylation (*157*) over the entire body.

Though mostly used in oncology, ^{18}F-FDG PET also has the potential for characterizing inflammatory diseases such as vasculitis (*158*), hepatitis (*93*), osteomyelitis

(*159*), and recently Coronavirus Disease 2019 (COVID-19) (*108,160–162*). COVID-19 primarily attacks the respiratory system, leading to conditions varying from mild manifestations to high-mortality acute symptoms (*163*). Meanwhile, it can affect multiple organs associated with different body systems, including the nervous (*164*), cardiovascular (*165*), and immune systems (*166*). In addition, a variety of prolonged effects of COVID-19 have been reported (*86,167–169*). However, investigations of the whole-body consequences and prolonged effects from COVID-19 are limited, partially due to the lack of an approach for in-depth total-body evaluation.

In this chapter, we conducted a quantitative evaluation of glucose utilization in multiple organs of healthy subjects and recovering COVID-19 subjects using total-body multiparametric ^{18}F-FDG PET imaging. We analyzed the overall glucose metabolism, and more subtly, the blood-to-tissue glucose delivery and glucose phosphorylation to gain further insight into the metabolic differences induced by COVID-19.

4.2 Materials and Methods

4.2.1. Study Participants and Data Acquisition

With Institutional Review Board approval and written informed consent at the University of California Davis Health, the study includes a cohort of thirteen healthy subjects and twelve COVID-19 subjects. These healthy subjects were scanned between May 2019 and January 2020. They had no history of major disease (e.g., cancer or myocardium infarction) over the previous five years and were without ongoing acute inflammation. The COVID-19 subjects had a confirmed diagnosis of COVID-19 through radiographic findings, and/or a positive antibody test. They had mild to moderate

Table 4.1 Information of Individual Subjects in the Healthy Group and the Recovering COVID-19 Group

Subject index	Age (years)	Gender	Weight (kg)	BMI (kg/m^2)	Dose (MBq)	Blood sugar level (mg/dL)	Fasting time before PET scan (hours)	COVID-19 vaccin-ation	Symptom indices	Days symptoms affected normal life
H01	78	Male	71	24	349	101	11	No	-	-
H02	53	Female	87	33	389	101	11	No	-	-
H03	26	Male	112	34	387	77	6	No	-	-
H04	50	Male	74	27	372	94	12	No	-	-
H05	51	Female	67	24	348	93	12	No	-	-
H06	62	Male	88	29	374	92	12	No	-	-
H07	63	Male	80	24	376	79	12	No	-	-
H08	48	Male	109	34	370	116	12	No	-	-
H09	41	Female	53	19	389	78	11	No	-	-
H10	51	Female	99	36	337	96	12	No	-	-
H11	29	Female	81	30	370	100	12	No	-	-
H12	30	Female	58	20	379	79	12	No	-	-
H13	51	Female	89	35	390	91	10	No	-	-
C01	31	Female	131	44	303	96	6	No	NA	NA
C02	55	Female	106	39	309	86	8	No	NA	NA
C03	45	Female	54	20	305	74	10	Yes	1, 2, 3,	8
C04	48	Female	72	29	292	83	12	Yes	1, 2, 3, 4	NA
C05	39	Male	87	25	285	86	10	No	1, 2, 4	10
C06	40	Female	69	25	298	81	12	No	2, 3	10
C07	51	Male	87	28	309	93	12	Yes	1, 4	NA
C08	23	Female	59	19	275	74	12	No	1, 2, 3, 4	5
C09	46	Female	74	30	285	84	7	Yes	2	7
C10	48	Male	57	19	244	93	12	Yes	1, 3	5
C11	26	Female	120	43	292	82	10	Yes	1, 2, 4	7
C12	45	Female	89	31	290	93	12	Yes	1, 3	14

Healthy subjects are indexed as H01-H13, and COVID-19 recovering subjects are indexed as C01-C12. Major symptoms acquired from a survey of the COVID-19 subjects are also listed. Symptom indices: 1: cough, 2: fever, 3: body aches, 4: dyspnea.

symptoms as summarized in Table 4.1, and none of them were hospitalized. Seven COVID-19 subjects had 1-3 doses of COVID-19 vaccines prior to PET imaging, and the other five were not vaccinated. Each subject had a total-body one-hour ^{18}F-FDG dynamic scan on the uEXPLORER PET/CT system (*79*,*128*). The PET/CT scans for the COVID-19 subjects were performed within eight weeks (37 ± 16 days) of confirmed diagnosis. All COVID-19 subjects tested negative for COVID-19 11 ± 7 days prior to the PET scan. The

Table 4.2. ROI Placement in Different Organs/Tissues for Kinetic Modelling

Organ/tissue	ROI placement
Lung	Five same-sized spherical ROIs were placed in each of the five lung lobes. Large vessel structures and lung boundary were avoided to minimize the motion effect. The five lobe ROI TACs were extracted and averaged to acquire a global lung TAC.
Myocardium	A 3D free-hand ROI were placed in the myocardium according to both the late frames (45 min - 60 min) and the early frames (0 - 10 min) of the dynamic PET image to minimize the motion and the spill-over effects.
Liver	An ellipsoid ROI was placed in the liver.
Spleen	An ellipsoid ROI was placed carefully in the spleen to diminish the motion effect from the lung.
Spine bone marrow	Ten same-sized cylinder ROIs were placed in the bone marrow of ten spine sections (thoracic T8 - T12, and lumbar L1 - L5). The extracted ten TACs were averaged to acquire a global spine bone TAC. Both PET and CT images were referred.
Pelvic bone marrow	Six ellipsoid ROIs were placed in the pelvic bone marrow, three on the left and three on the right according to both the PET images and CT images.
Thigh muscle	An ellipsoid ROI was placed in the quadriceps femoris muscle of the right thigh and large blood vessels were avoided.
Gray matter	An isocontour ROI was placed in the gray matter according to the late phase (45 min - 60 min) PET image.
White matter	An ellipsoid ROI was placed in the white matter according to the PET image.
Brainstem	An ellipsoid ROI was placed in the brain stem according to the PET image.
Cerebellum	An ellipsoid ROI was placed in the cerebellum according to the PET image
Ascending Aorta	A 3D free-hand ROI was placed according to both the late frames (45 min - 60 min) and the early frames (0 - 10 min) of the dynamic PET images.
Right Ventricle	An ellipsoid ROI was placed according to both the late-frame (45 min - 60 min) and the early-frame (0 - 10 min) dynamic PET images.

subjects were injected with 333 ± 45 MBq ^{18}F-FDG intravenously immediately after initiating list-mode data acquisition. A total-body ultralow-dose CT scan with settings of 140 kVp and 5 mAs was performed before the PET scan for attenuation correction. Dynamic PET data were reconstructed into 29 frames ($6 \times 10\ \mathrm{s}, 2 \times 30\ \mathrm{s}, 6 \times 60\ \mathrm{s}, 5 \times 120\ \mathrm{s}, 4 \times 180\ \mathrm{s}, 6 \times 300\ \mathrm{s}$) with a voxel size of $4 \times 4 \times 4\ \mathrm{mm}^3$ using the vendor-provided ordered subset expectation maximization algorithm with four iterations and 20 subsets (*128*).

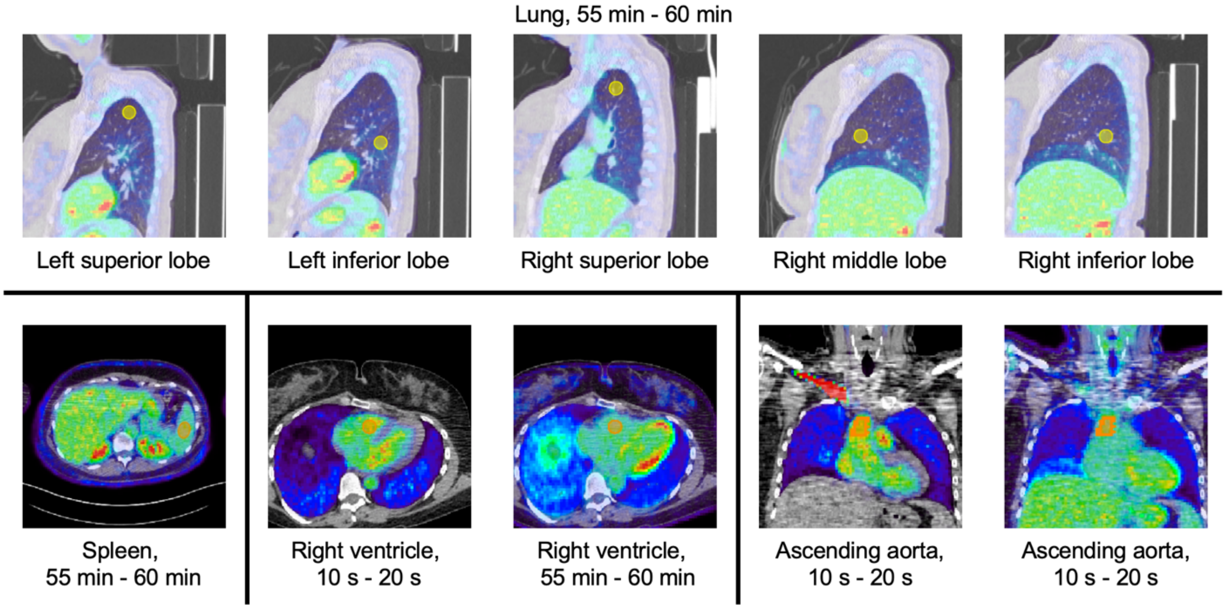

Lung, 55 min - 60 min

Left superior lobe

Left inferior lobe

Right superior lobe

Right middle lobe

Right inferior lobe

Spleen, 55 min - 60 min

Right ventricle, 10 s - 20 s

Right ventricle, 55 min - 60 min

Ascending aorta, 10 s - 20 s

Ascending aorta, 10 s - 20 s

Figure 4.1. Example ROI placement on the lung lobes, spleen, right ventricle, and ascending aorta.

4.2.2. Total-Body Kinetic Modeling

Regions of interest (ROIs) were placed in various organs and tissues (e.g., brain, liver, lungs, spleen, bone marrow) throughout the entire body on the dynamic images of each subject (see details of ROI placement in Table 4.2 and Figure 4.1). Time-activity curves (TACs) were then extracted from the organ ROIs. In addition, ROI placement and TAC extraction were also done for the ascending aorta and right ventricle to acquire image-derived input functions (IDIFs).

A two-tissue irreversible (2Ti) model, as shown in Figure 1.6B, was used for modeling the dynamic ^{18}F-FDG data with time delay correction included *(69)*. The modeled is described in Section 1.4 and follows Eqs. 1.6 - 1.9. Different image-derived input functions were used as appropriate for the kinetic modeling of different organs. The IDIF for most organs is the ascending aorta (AA) TAC:

$$C_{\mathrm{p}}(t) = C_{\mathrm{AA}}(t - t_{\mathrm{d}}), \qquad \text{Eq. 4.1}$$

except for the lungs for which the IDIF is the right ventricle (RV) TAC:

$$C_{\mathrm{p,lung}}(t) = C_{\mathrm{RV}}(t - t_{\mathrm{d}}), \qquad \text{Eq. 4.2}$$

where t_{d} (s) is the time delay correction parameter.

All the kinetic parameters (blood-to-tissue ^{18}F-FDG delivery rate K_1, tissue-to-blood delivery rate k_2, phosphorylation rate k_3, fractional blood volume v_{b}, and time delay t_{d}) were jointly estimated through a non-linear least-square fitting method (Eq. 1.11) (*69*) with a weighting factor (Eq. 2.2) that considers the time length of each frame and nuclear decay (*170*).

4.2.3. Macroparametric and Microparametric Quantification

The macro-parameter K_{i}, denoting ^{18}F-FDG net influx rate, is commonly used to characterize overall glucose metabolism and is calculated by Eq. 1.10. We also applied semi-quantitative standardized uptake value (SUV) (Eq. 1.4) (*60*) and SUV ratio relative to blood (SUVR) (Eq. 1.5) (*62*) using the last dynamic frame (55-60 min) to evaluate the overall glucose metabolism. Same as the compartmental modeling, the right ventricle was used for SUVR calculation of the lung, and the ascending aorta was used for the SUVR calculation of all other organs.

In addition to the measures of overall ^{18}F-FDG metabolism by SUV, SUVR, and K_{i}, we also used the microparameters of the 2Ti kinetic model, specifically the ^{18}F-FDG delivery rate K_1 and phosphorylation rate k_3, to gain insight into the individual molecular processes of glucose utilization. The ability of this microparametric quantification is a feature that distinguishes compartmental modeling from whole-body static imaging or whole-body dynamic imaging with a simplified graphical analysis method (e.g., the Patlak plot).

4.2.4. Statistical Analysis

Statistical analysis in this study was performed using an unpaired, two-tailed T test and the Mann-Whitney U test on SUV, SUVR and parametric PET metrics to investigate metabolic differences in the recovering COVID-19 subjects compared to the healthy subjects. In addition, the tests were performed on lung CT ROI quantitation for complementary information. Effect of vaccination was also investigated when appropriate between the vaccinated and the unvaccinated COVID-19 groups to study the potential influence of vaccination (*171*,*172*). All statistical data analyses were conducted using MATLAB (Mathworks, MA). P-values of less than 0.05 were considered statistically significant. The family-wise error rate was not corrected in this pilot study.

For organs that showed a trend of differences in glucose metabolism between the healthy and the COVID-19 groups, the Pearson correlation analysis and Spearman rank correlation analysis between K_i and micro-parameters $K_1, k_2,$ and k_3 were also calculated to understand the association among the delivery, phosphorylation, and the overall metabolism of ^{18}F-FDG.

4.2.5. Parametric Imaging of COVID-19

In addition to the ROI-based analysis, voxel-wise parametric images were generated for the healthy subjects and the recovering COVID-19 subjects using the 2Ti compartmental model (*130*,*173*). Kernel smoothing was applied to both the dynamic images and parametric images for noise reduction *(69)*. To make the comparison of parametric images more focused on organs of interest, masking was used to visualize individual organs or tissues (e.g., lung or bone marrow) within the parametric images for inter-subject comparisons.

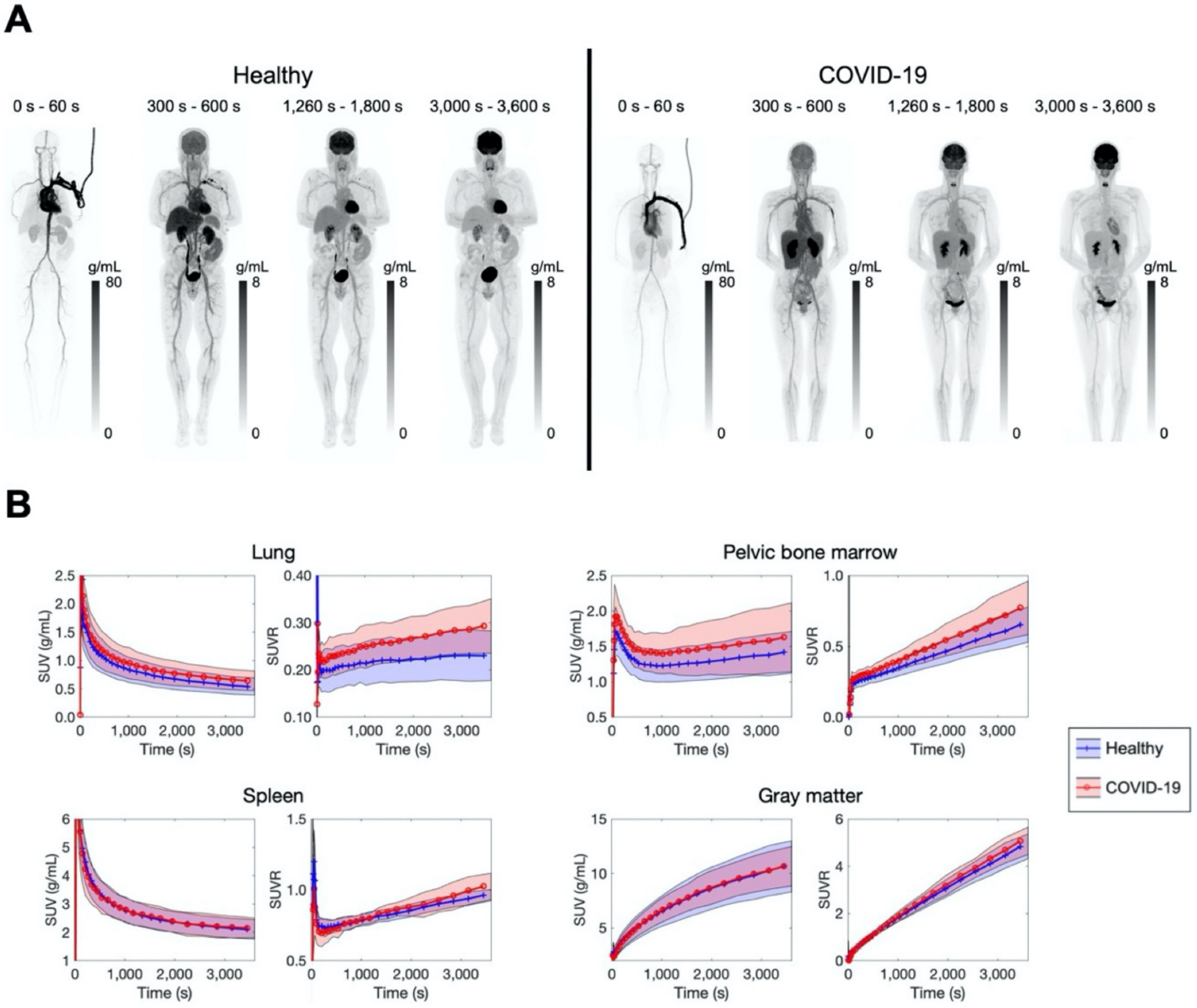

Figure 4.2. (A) Total-body dynamic ^{18}F-FDG PET images of a healthy subject and a recovering COVID-19 subject. Shown are maximum intensity projections. (B) Averaged TACs (shown as SUV and SUVR) of four organs of interest (lung, pelvic bone marrow, spleen, and gray matter) of the thirteen healthy and the twelve recovering COVID-19 subjects. The averaged values are shown as the solid lines, and the standard deviations are shown as the bands.

4.3. Results

4.3.1. Patient Characteristics

A summary of patient characteristics is provided in Table 4.1. The healthy subjects include six males and seven females with age 49 ± 15 y and weight 82 ± 18 kg. The COVID-19 subjects include three males and nine females with age 41 ± 10 y and weight 84 ± 25 kg. There was no statistical difference between the two groups in age, weight, body mass index (BMI), blood glucose level, or fasting time before the PET scan using the unpaired T test and the U test. In addition, there was no statistical difference in lung CT values and in the SUV of the input functions between the two groups.

4.3.2. Dynamic Images and TACs

Total-body dynamic ^{18}F-FDG PET images of a representative healthy subject and a recovering COVID-19 subject are shown in Figure 4.2A. Figure 4.2B shows four examples of the TACs in the form of SUV and SUVR over time. The most notable finding was the increased lung SUVR in the recovering COVID-19 group compared to the healthy group, while the bone marrow SUVR and spleen SUVR of recovering COVID-19 group also tended to be higher.

4.3.3. Comparison of Overall Glucose Utilization in Multiple Organs

Table 4.3 summarizes the SUV, SUVR, and K_i of the healthy and the recovering COVID-19 groups along with group comparison results for 11 different organ ROIs. There was no significant difference in lung SUV between the two groups ($p > 0.1$) (Figure 4.3).

Table 4.3. Comparison of the ^{18}F-FDG Metabolic Metrics SUV (g/mL), SUVR, and K_i (mL/min/cm^3) Between the Healthy Subjects and Recovering COVID-19 Subjects in Multiple Organs/Tissues.

Organ/tissue	Metric	Healthy group (mean ± sd)	COVID-19 recovering group (mean ± sd)	P_T	P_U
Lung	SUV	0.54±0.16	0.64±0.18	0.15	0.22
	SUVR	0.230±0.055	0.293±0.060	0.012	0.018
	K_i	0.00038±0.00033	0.00084±0.00045	0.0075	0.011
Myocardium	SUV	7.5±3.5	5.8±2.8	0.21	0.20
	SUVR	3.4±1.6	2.8±1.4	0.38	0.34
	K_i	0.055±0.033	0.043±0.025	0.31	0.37
Liver	SUV	2.64±0.44	2.56±0.40	0.65	0.61
	SUVR	1.208±0.060	1.218±0.061	0.69	0.68
	K_i	0.00279±0.00094	0.00330±0.00086	0.17	0.17
Spleen	SUV	2.11±0.35	2.15±0.36	0.74	0.93
	SUVR	0.963±0.041	1.024±0.097	0.048	0.053
	K_i	0.0037±0.0010	0.0049±0.0018	0.055	0.087
Spine bone marrow	SUV	2.06±0.38	2.21±0.59	0.43	0.57
	SUVR	0.95±0.17	1.05±0.21	0.21	0.22
	K_i	0.0072±0.0015	0.0080±0.0023	0.35	0.50
Pelvic bone marrow	SUV	1.42±0.31	1.63±0.51	0.22	0.43
	SUVR	0.65±0.13	0.77±0.20	0.087	0.13
	K_i	0.0050±0.0012	0.0059±0.0019	0.19	0.24
Thigh muscle	SUV	0.57±0.16	0.58±0.12	0.92	0.93
	SUVR	0.262±0.056	0.279±0.065	0.50	0.72
	K_i	0.00168±0.00057	0.00179±0.00059	0.65	0.89
Gray matter	SUV	10.7±2.4	10.7±1.9	0.99	0.76
	SUVR	4.84±0.54	5.07±0.60	0.33	0.31
	K_i	0.0476±0.0062	0.0487±0.0061	0.65	0.68
White matter	SUV	4.5±1.6	3.9±1.0	0.28	0.22
	SUVR	2.03±0.45	1.85±0.31	0.26	0.46
	K_i	0.0168±0.0051	0.0148±0.0046	0.33	0.50
Brainstem	SUV	6.1±1.3	5.84±0.82	0.55	0.68
	SUVR	2.78±0.24	2.79±0.34	0.90	0.85
	K_i	0.0247±0.0023	0.0241±0.0033	0.62	0.46
Cerebellum	SUV	7.3±1.3	6.99±0.77	0.49	0.50
	SUVR	3.34±0.28	3.35±0.27	0.93	0.89
	K_i	0.0300±0.0033	0.0300±0.0030	1.0	1.0

However, there was a statistically significant increase of ~120% in lung K_i in the COVID-19 group ($p \approx 0.01$). SUVR showed a difference (~25% increase) but to a lower degree.

The ^{18}F-FDG metabolism of the spleen was higher in the COVID-19 group as shown in Table 4.3 and the boxplots in Figure 4.3. K_i produced a larger group difference than

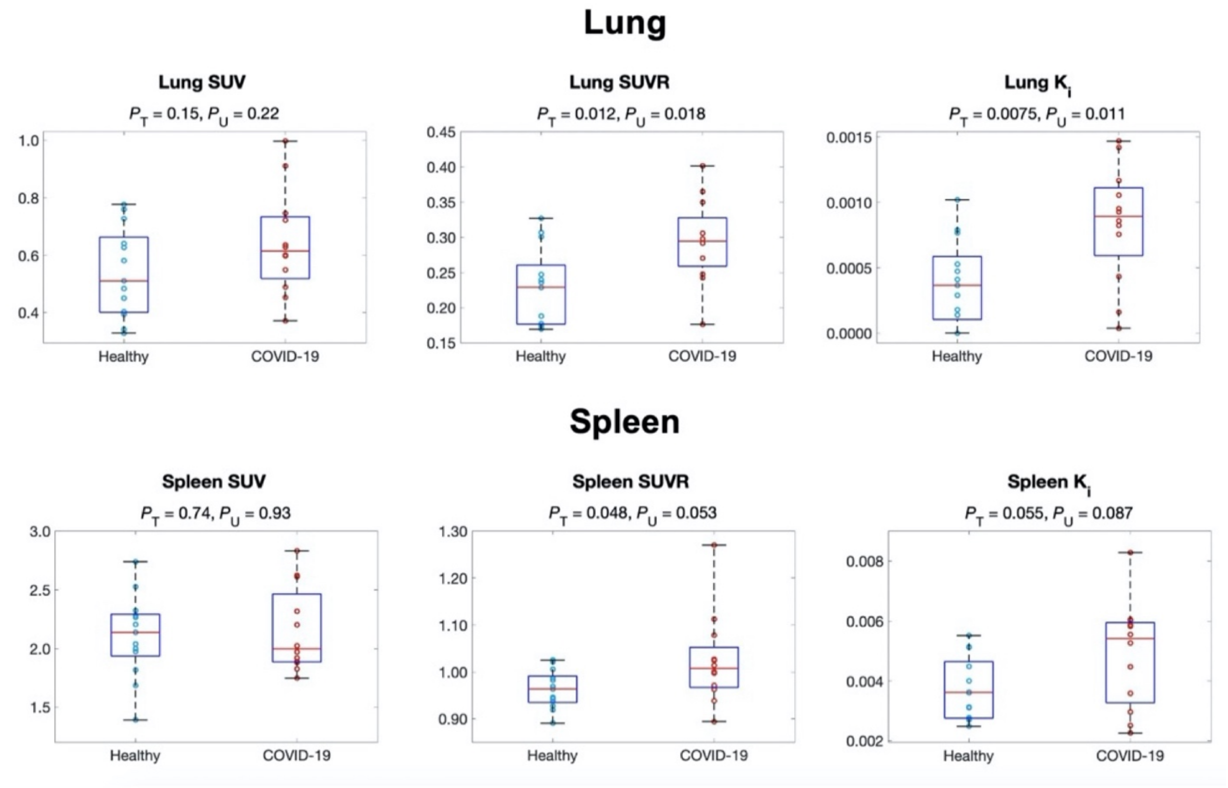

Figure 4.3. Comparison of ^{18}F-FDG metabolism in the lung (top) and spleen (bottom) between the healthy and recovering COVID-19 groups using SUV, SUVR (both at 55 - 60 min), and K_i. P_T and P_U are the p-values of the T test and the Mann-Whitney U test, respectively.

SUV, while SUVR was comparable to K_{i}. The ^{18}F-FDG metabolism of the pelvic bone marrow also tended to increase ($p \approx 0.1$), as shown by the SUVR measures in Table 4.3 and Figure 4.4. We did not observe a statistically significant difference with SUV, SUVR, and K_{i} in other organs (e.g., brain, liver).

Based on the above analyses, the lung, bone marrow, and spleen were selected for further study of microparametric quantification.

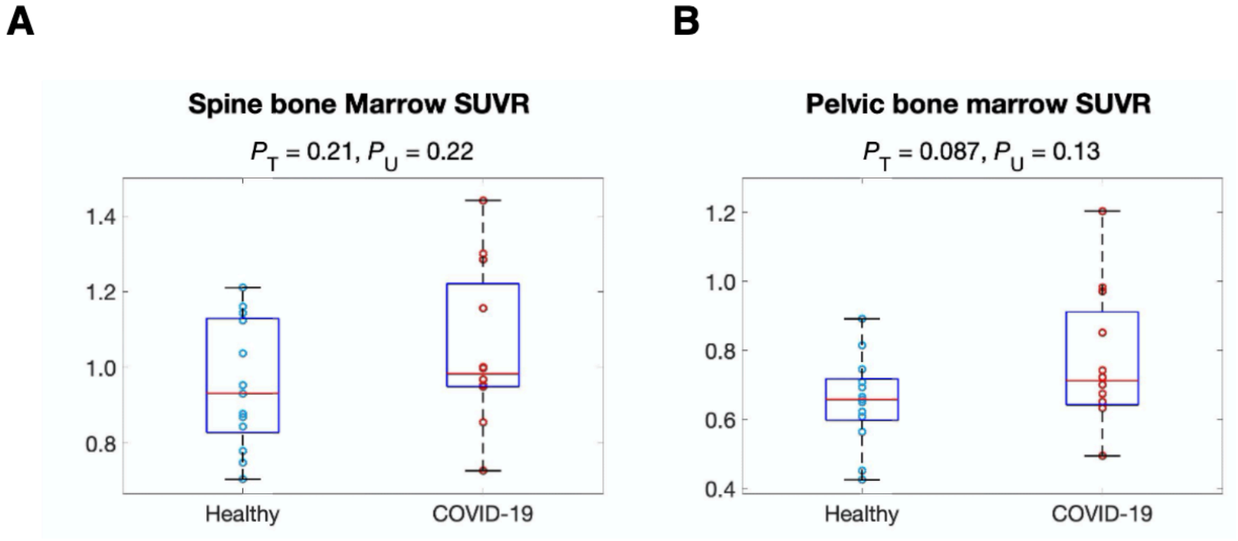

Figure 4.4. Comparison of ^{18}F-FDG SUVR of the (A) spine bone marrow and (B) pelvic bone marrow between the healthy and the recovering COVID-19 groups.

Table 4.4. Comparison of Lung Micro Kinetic Parameters K_1, k_2, and k_3 Between Healthy Subjects and Recovering COVID-19 Subjects and the Correlation Between the Microparameters and Lung ^{18}F-FDG Net Influx Rate K_i Using the Pearson and Spearman Analyses.

Kinetic parameter	Healthy *vs.* COVID-19 group comparison				Correlation with K_i			
	Healthy group (mean ± sd)	COVID-19 recovering group (mean ± sd)	P_T	P_U	Pearson		Spearman	
					r	P	ρ	P_S
K_1 (mL/min/cm^3)	0.018±0.022	0.017±0.019	0.89	0.98	0.23	0.26	0.44	0.028
k_2 (min^{-1})	0.32±0.33	0.26±0.25	0.61	0.81	0.17	0.42	0.36	0.075
k_3 (min^{-1})	0.0079±0.0071	0.021±0.023	0.049	0.011	0.56	0.0035	0.87	1.7e-08

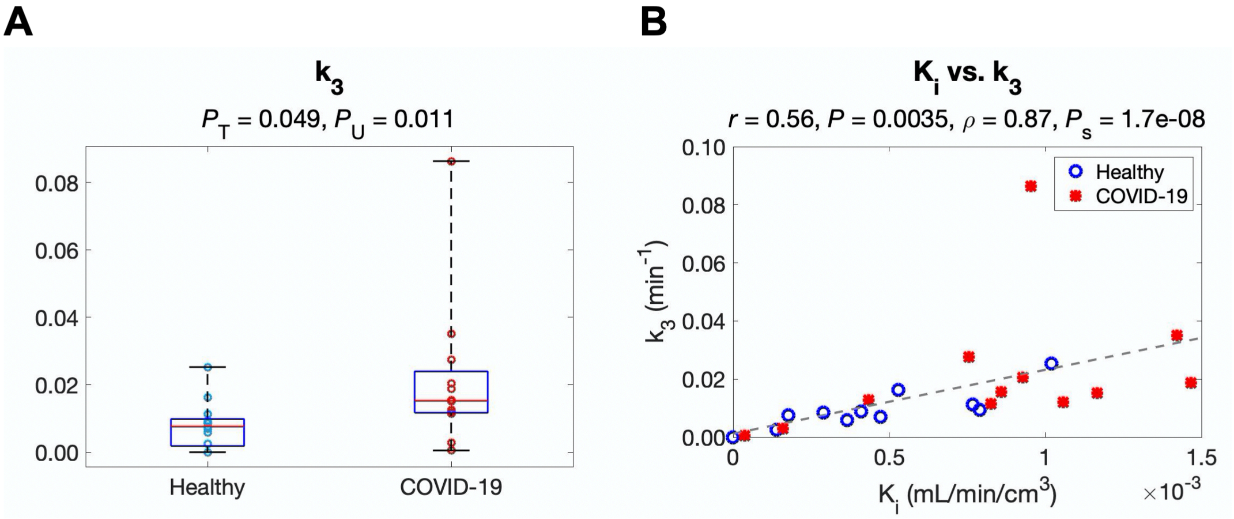

Figure 4.5. Study of lung kinetic parameters in the healthy and the recovering COVID-19 groups. (A) Comparison of ^{18}F-FDG phosphorylation rate k_3 between the two groups. (B) Correlation between k_3 and ^{18}F-FDG net influx rate K_i among the subjects.

4.3.4. Microparametric Quantification of the Lungs

Table 4.4 shows the analysis of microparametric quantification of the lungs. The correlation between each microparameter and lung K_i is also included using all subject data. Neither K_1 nor k_2 detected any group difference ($p > 0.6$). k_3 was much higher in the COVID-19 group ($p < 0.05$), as further shown in Figure 4.5A. Also, k_3 had the strongest correlation with K_i ($p < 0.01$) among the three microparameters (Figure 4.5B), while the correlations of K_1 and k_2 with K_i were weaker ($p > 0.25$). The findings suggested that increased ^{18}F-FDG phosphorylation (as quantified by k_3) might be the main driving factor for the increased lung ^{18}F-FDG metabolism (assessed by K_i) in COVID-19 recovery.

Table 4.5. Comparison of Bone Marrow Micro Kinetic Parameters K_1, k_2, and k_3 Between Healthy Subjects and Recovering COVID-19 Subjects and the Correlation Between the Microparameters and Bone Marrow ^{18}F-FDG Net Influx Rate K_i Using the Pearson and Spearman Analyses.

Bone marrow type	Kinetic parameter	Healthy *vs.* COVID-19 recovering comparison				Correlation with K_i			
		Healthy group (mean±sd)	COVID-19 recovering group (mean±sd)	P_T	P_U	Pearson		Spearman	
						r	P	ρ	P_S
Spine	K_1(mL/min /cm^3)	0.221 ±0.055	0.285 ±0.089	0.041	0.068	0.46	0.020	0.39	0.056
	k_2 (min^{-1})	0.76 ±0.19	0.92 ±0.31	0.14	0.20	0.45	0.023	0.35	0.091
	k_3 (min^{-1})	0.0261 ±0.0061	0.027 ±0.013	0.73	0.76	0.78	3.5e-06	0.82	2.2e-06
Pelvic	K_1(mL/min /cm^3)	0.122 ±0.026	0.149 ±0.037	0.042	0.047	0.66	0.00032	0.71	9.5e-05
	k_2 (min^{-1})	0.573 ±0.081	0.64 ±0.14	0.17	0.26	0.51	0.0090	0.51	0.011
	k_3 (min^{-1})	0.0246 ±0.0060	0.0262 ±0.0088	0.61	0.81	0.85	9.1e-08	0.77	1.3e-05

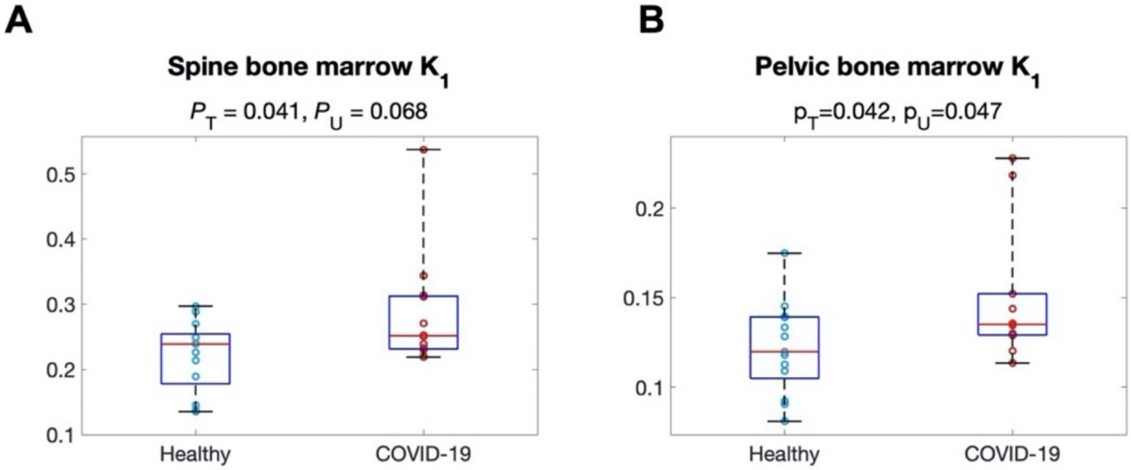

Figure 4.6. Comparison of ^{18}F-FDG delivery rate K_1 of the (A) spine bone marrow and (B) pelvic bone marrow between the healthy and the recovering COVID-19 groups.

Table 4.6. Comparison of Spleen Micro Kinetic Parameters K_1, k_2, and k_3 Between Healthy Subjects and Recovering COVID-19 Subjects and the Correlation Between the Microparameters and Spleen ^{18}F-FDG Net Influx Rate K_i Using the Pearson and Spearman Analyses.

Kinetic parameter	Healthy *vs.* COVID-19 group comparison				Correlation with K_i			
	Healthy group (mean ± sd)	COVID-19 recovering group (mean ± sd)	P_T	P_U	Pearson		Spearman	
					r	P	ρ	P_S
K_1 (mL/min/cm^3)	1.61±0.75	1.31±0.88	0.37	0.40	-0.55	0.0044	-0.65	0.00052
k_2 (min^{-1})	2.5±1.0	2.1±1.2	0.34	0.40	-0.43	0.034	-0.46	0.021
k_3 (min^{-1})	0.0062 ±0.0024	0.0090 ±0.0041	0.047	0.097	0.98	9.6e-17	0.98	6.3e-07

4.3.5. Microparametric Quantification of Bone Marrow

The microparametric quantification results for bone marrow are summarized in Table 4.5. While bone marrow metabolism did not show a statistically significant difference between the two groups as measured with SUV, SUVR or K_i (Table 4.3), bone-marrow ^{18}F-FDG delivery rate K_1 was ~20% higher in the COVID-19 subjects with statistical difference ($p < 0.05$), as shown in Figure 4.6 and Table 4.5. In comparison, no statistical significances were observed in k_2 or k_3. In contrast to the results in the lungs, here the bone marrow microparameters K_1, k_2, and k_3 all had strong correlations with K_i, though the correlation of K_1 with K_i remained weaker (Table 4.5).

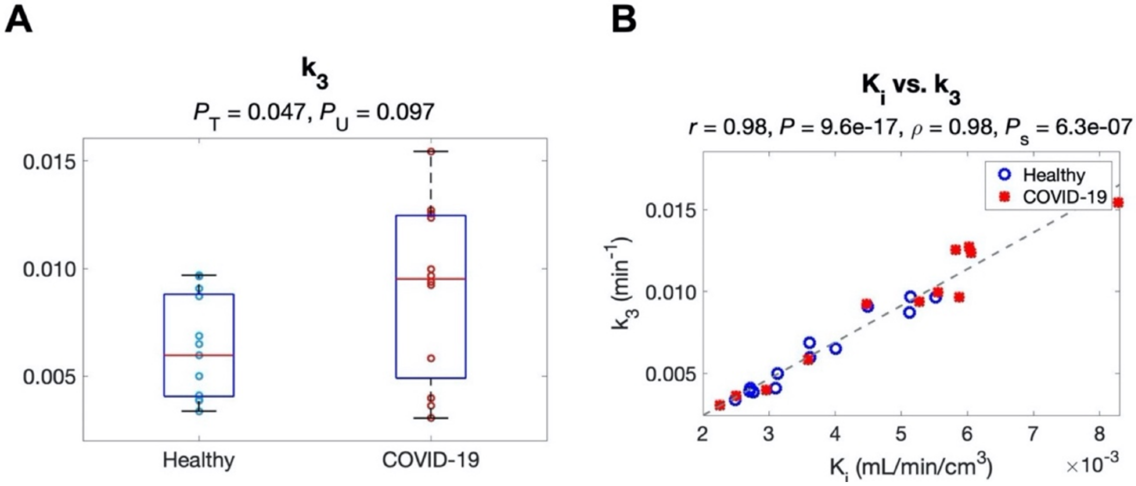

Figure 4.7. Study of microparametric quantification in the spleen. (A) Comparison of k_3 between the two groups. (B) Correlation between k_3 and K_i among the subjects.

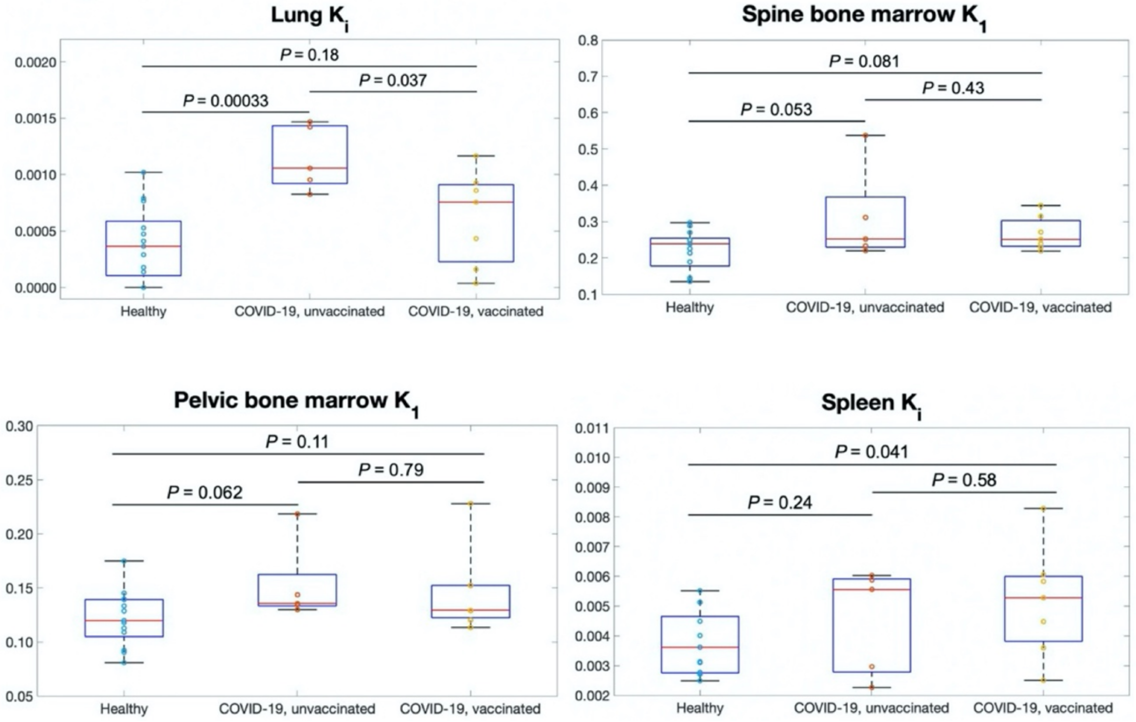

Figure 4.8. Evaluation of unvaccinated and vaccinated COVID-19 subjects as compared to healthy subjects using kinetic parameters of interest: lung ^{18}F-FDG net influx rate K_i, spine bone marrow ^{18}F-FDG delivery rate K_1, pelvic bone marrow K_1, and spleen K_i. P values were calculated using the unpaired T test.

4.3.6. Microparametric Quantification of the Spleen

Table 4.6 shows the microparametric quantification results for the spleen. k_3 was ~45% higher in the COVID-19 group (Figure 4.7A), while K_1 and k_2 did not show a significant group difference ($p > 0.3$). k_3 correlated the most strongly with K_i among the three microparameters (Figure 4.7B), indicating that the increased trend in spleen ^{18}F-FDG metabolism (represented by SUVR and K_i) was dominated by the increased phosphorylation. Overall, the observed changes in the spleen were similar to that of the lungs but with a weaker statistical significance.

4.3.7. Effect of Vaccination

Among the COVID-19 subjects, five were unvaccinated and seven were vaccinated prior to their PET scans (Table 4.1). There was no statistical difference in age, BMI, blood sugar level between the unvaccinated and vaccinated COVID-19 subjects ($p > 0.2$). Lung K_i was higher in unvaccinated COVID-19 subjects as compared to healthy subjects ($p < 0.001$), as shown in Figure 4.8. Lung K_i was reduced in vaccinated COVID-19 subjects but still slightly higher than in the healthy group. Spine bone-marrow K_1 of both unvaccinated and vaccinated COVID-19 subjects was higher than that of healthy subjects, but it did not differ much between unvaccinated and vaccinated COVID-19 subjects. Figure 4.8 also shows that spleen K_i of the vaccinated subjects tended to have a larger difference from the healthy subjects than that of the unvaccinated ones. No effect of vaccination was noted in other organs of recovering COVID-19 subjects.

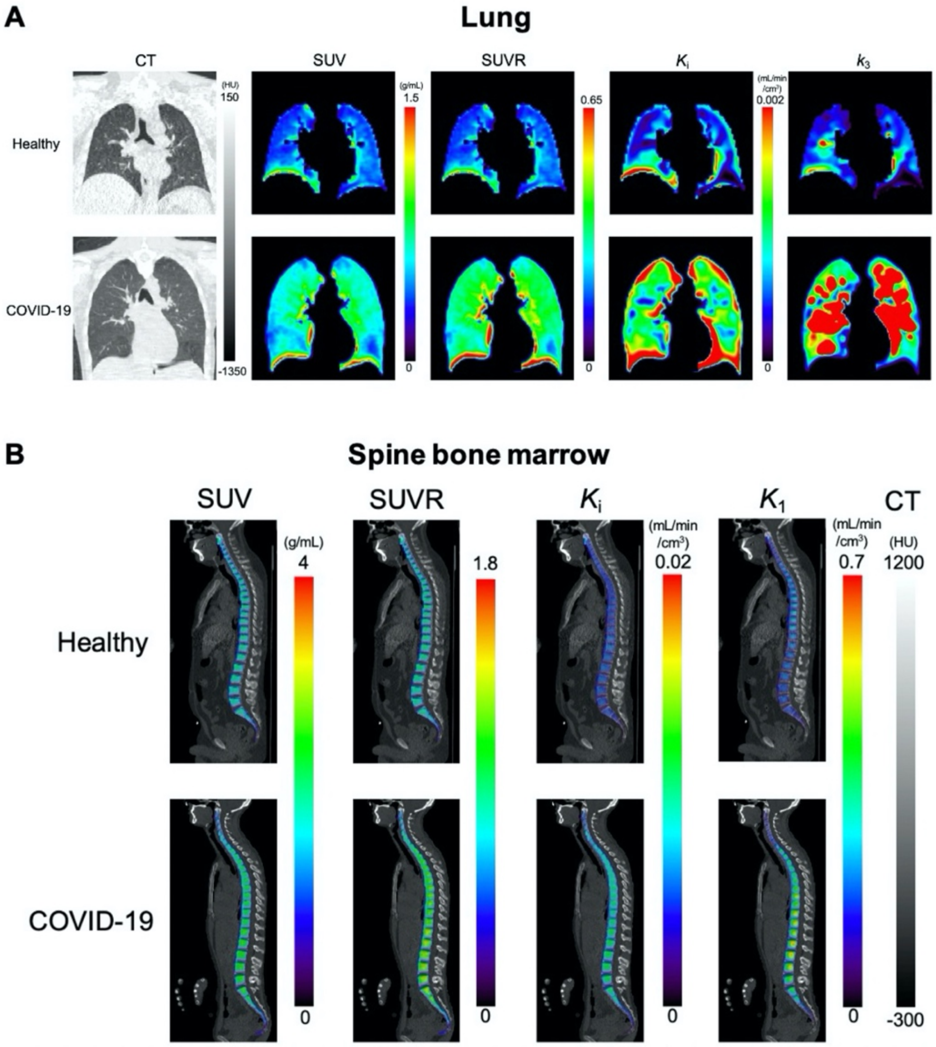

Figure 4.9. Parametric images of example healthy subjects and COVID-19 subjects. (A) Lung CT, ^{18}F-FDG SUV, SUVR, and parametric images of ^{18}F-FDG net influx rate K_i, and ^{18}F-FDG phosphorylation rate k_3. The coronal slices are selected as the mid of trachea carina. (B) Spine bone marrow images of ^{18}F-FDG SUV, SUVR, and parametric images ^{18}F-FDG net influx rate K_i, and blood-to-tissue ^{18}F-FDG delivery rate K_1. The PET images are masked for the bone marrow region and overlaid on the CT images.

4.3.8. Parametric Imaging of Recovering COVID-19

Figure 4.9 shows the parametric images of the lungs and bone marrow from healthy subjects and COVID-19 subjects. The lung images of SUVR, K_i and k_3 showed enhanced

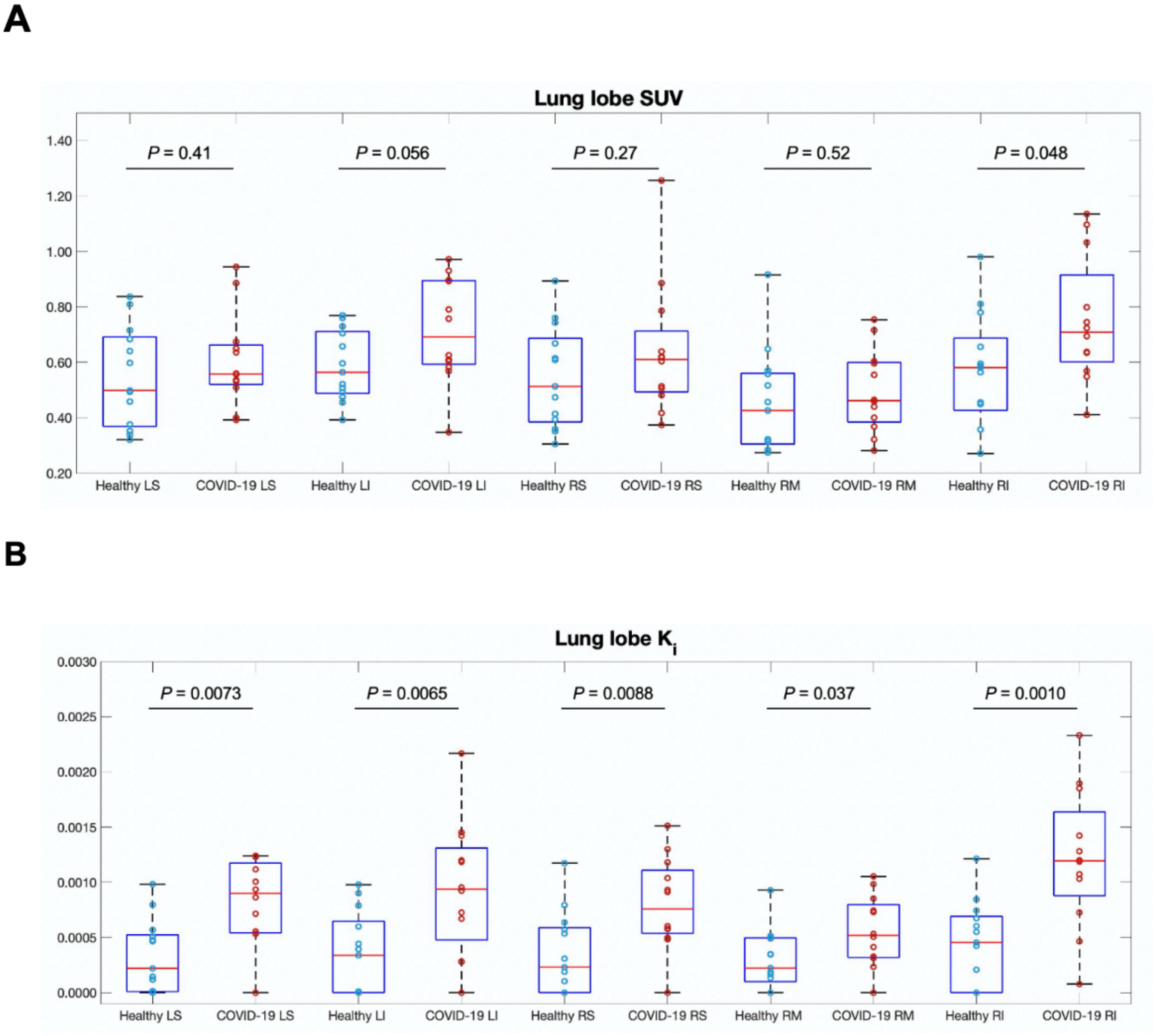

Figure 4.10. SUV (A) and K_i (B) of the five lung lobes (LS, LI, RS, RM, RI) of the healthy subjects and the COVID-19 recovery subjects. T test p-values are labeled. LS: left superior; LI: left inferior; RS: right superior; RM: right middle; RI: right inferior.

contrast between the healthy and the recovering COVID-19 compared to SUV (Figure 4.9A) through visual inspection, supporting the ROI-based analyses. The demonstrated spatial heterogeneity across different lung lobes (Figure 4.9A) is also consistent with the lobe-based results of lung SUV and K_i as reported in Figure 4.10. In all five individual lung lobes, K_i produced a larger statistical group difference than SUV.

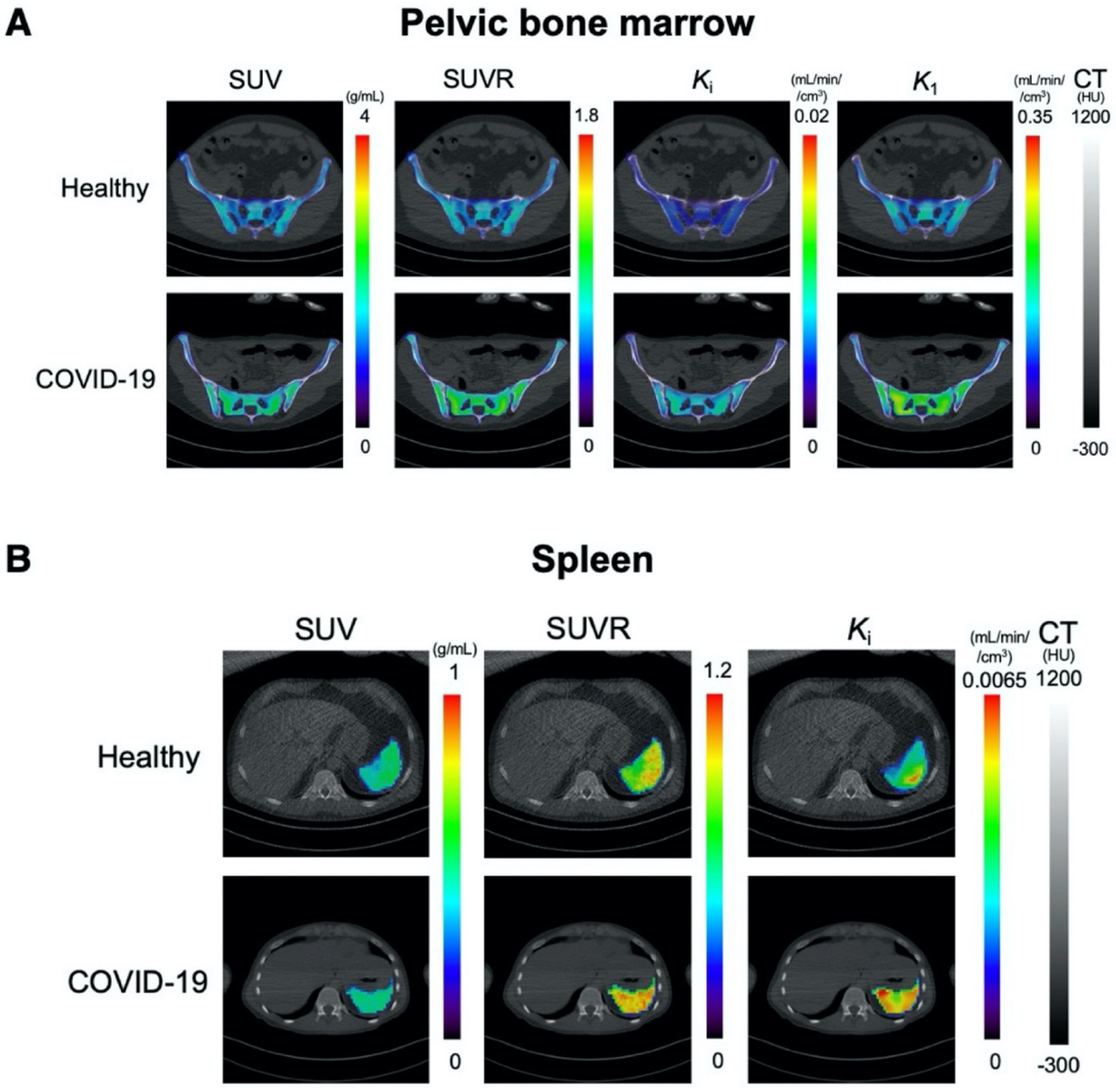

Figure 4.11. Parametric images of example healthy subjects and COVID-19 subjects. (A) Pelvic bone-marrow images of ^{18}F-FDG SUV, SUVR, and parametric images of ^{18}F-FDG net influx rate K_i, and blood-to-tissue ^{18}F-FDG delivery rate K_1. (B) Spleen ^{18}F-FDG SUV, SUVR, and parametric images of ^{18}F-FDG net influx rate K_i. The masked PET images are overlaid on the CT images.

The spine bone marrow (Figure 4.9B) and pelvic bone marrow (Figure 4.11A) images of K_i and K_1 showed increased contrast between the two subjects than SUV. The SUVR and K_i images of the spleen also tended to have higher contrast as compared to the SUV images (Figure 4.11B). These observations are consistent with the ROI-based findings.

4.4. Discussion

In this pilot study, we evaluated the metabolic differences in multiple organs between recovering COVID-19 subjects and healthy subjects using total-body dynamic ^{18}F-FDG PET combined with kinetic modeling. This chapter focuses on establishing the technical foundation for quantitative measurements of glucose metabolism using total-body dynamic PET within the context of COVID-19, which helps inform and guide future research that involves subtle systemic changes, such as in longitudinal tracking of long COVID-19.

We detected increased metabolism using K_i in the lung, while SUV or CT values gave no group differentiation (Table 4.3 and Figure 4.3), indicating the ability of lung K_i to detect a subtle difference that is undetectable with SUV or CT. The inability of SUV to distinguish the groups is likely due to its semi-quantitative nature and being susceptible to confounding factors (*60*). The results suggest the power of kinetic quantification for assessing glucose metabolism. The increased lung metabolism in the COVID-19 group may indicate continued inflammation during the early stages of recovery. Previous dynamic lung ^{18}F-FDG PET studies have associated increased lung K_i with pulmonary inflammation in multiple conditions, such as acute lung injury (*112*) and chronic obstructive pulmonary disease (*174*). Meanwhile, prolonged lung inflammation caused by COVID-19 has also been reported, which can last more than 60 days after infection, even for asymptomatic and patients with mild cases (*175*,*176*). The detected difference in lung glucose metabolism might potentially be related to the increased metabolism of immune cells, such as neutrophils (*104*,*112*,*177*) and macrophages (*178*,*179*), due to their accumulation and activation in the lungs.

Another advantage of compartmental modeling is microparametric quantification. According to the analysis in the lungs, ^{18}F-FDG phosphorylation rate k_3 is the parameter that was responsible for the healthy *vs.* COVID-19 group difference in K_i (Figure 4.5, and Figure 4.9A) and correlated best with K_i among different microparameters (Table 4.4). The result implied that increased glucose phosphorylation, rather than glucose delivery, may be the main driving factor for increased lung metabolism. These findings are also consistent with previous animal studies that observed k_3 increases in lung inflammation and the association between K_i and k_3 (*112*,*125*,*130*,*173*).

Interestingly, bone marrow demonstrated a significant change of K_1 in the recovering COVID-19 group as compared to healthy subjects (Figure 4.6, and Figure 4.9B), but no differences were observed with SUV, SUVR or K_i that reflects the overall ^{18}F-FDG metabolism (Table 4.3). This result further indicates the substantial importance of microparametric quantification. Bone marrow is essential for immunoregulation and is the origin of immune cells (*180*). Animal studies have reported that bone marrow cells play an important role in the repair of the injured lung during lung inflammation (*181*,*182*). Hence, the increased ^{18}F-FDG delivery represented by K_1 may be associated with immune system response during COVID-19 recovery. Given that ^{18}F-FDG K_1 of liver was also demonstrated to associate with hepatic inflammation in fatty liver disease (*93*,*183*), the interplay between K_1 and inflammation reaction, and the potential of K_1 as a biomarker of disease, are worth more studies to explore its clinical applications.

The spleen tended to have higher glucose metabolism in the COVID-19 group, as represented by K_i or SUVR (Table 4.3). This observation is consistent with the splenic ^{18}F-FDG uptake increase reported in previous studies of COVID-19 (*162*) and other infectious diseases (*184*). As an immune organ, the spleen plays an important role in response to COVID-19 (*185*), and the immune response may lead to increased metabolism.

Our study also separated the unvaccinated and vaccinated COVID-19 groups to evaluate the potential effect of vaccination. The results from the unvaccinated COVID-19 subjects alone (Figure 4.8) confirmed that COVID-19 is likely responsible for the observed differences in the lungs and bone marrow between the recovering COVID-19 group and healthy subjects. Nonetheless, vaccination showed a combined effect on top of the impact of COVID-19. The lower lung K_i in the vaccinated group may indicate reduced lung inflammation due to a protecting effect of vaccination. The higher spleen K_i in the vaccinated subjects (Figure 4.8) could also suggest increased immune response due to vaccination. It is worth noting that these results are complicated by different vaccination conditions, such as the type, dose, and vaccination date prior to the PET scan.

Our study in this chapter has several limitations. First, the pilot study cohort is relatively small, especially in the comparison of unvaccinated (five subjects) *vs.* vaccinated (seven subjects). Therefore, the results, particularly concerning physiological insights, should be interpreted with caution and warrant further confirmation with future hypothesis-driven studies. With an increased sample size, it may be possible to further observe some group differences that were not statistically significant in the current study. Second, the healthy and the COVID-19 groups are not exactly matched in this pilot study. Although

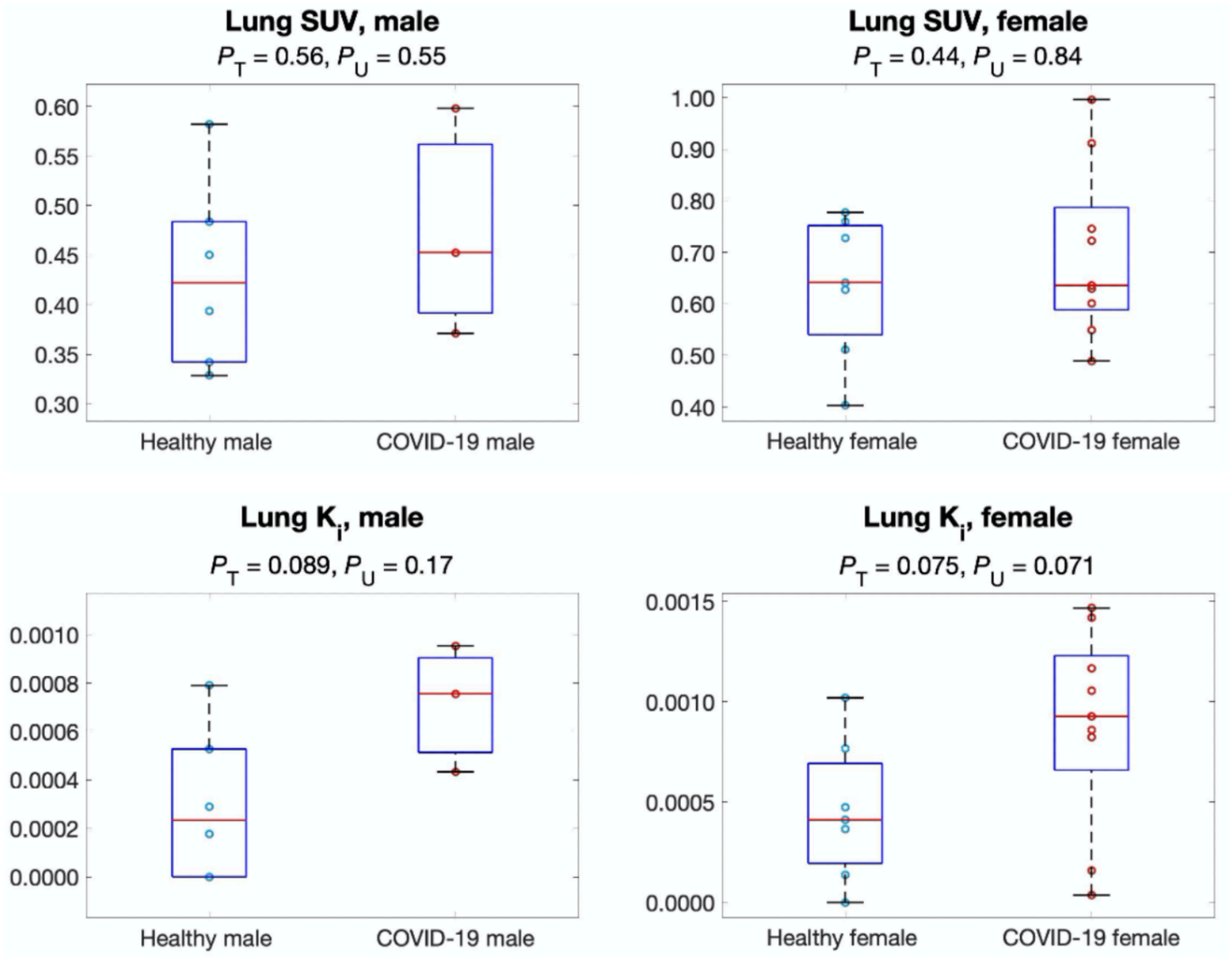

Figure 4.12. Comparison of lung SUV and K_i between healthy and COVID-19 recovery groups separating male subjects and female subjects.

there is no statistical difference in age, weight, BMI, and blood sugar level between healthy subjects and recovering COVID-19 subjects, the unpaired age and the time variability between the COVID-19 diagnosis and PET/CT scan could introduce potential bias. We noticed that the percentage of females is higher in the COVID-19 group, and therefore further separated the analyses according to gender. Example results for lung SUV and K_i are provided in Figure 4.12 to indicate that the major findings of this chapter remained valid, though the statistical difference of K_i became lower, primarily due to the limited sample size. Third, the study lacks histopathology or clinical laboratory data to elaborate the reason for the differences in ^{18}F-FDG kinetics between the two groups, and the potential impact of COVID-19 treatment on PET quantification was not analyzed due to the inaccessibility of medical records. In addition, some of the healthy cohort, though recruited between May 2019 and January 2020, before the COVID-19 pandemic (first confirmed US case was January 18th, 2020), might possibly have been exposed to COVID-19. Fourth, the statistical analysis in this pilot study was not corrected for possible family-wise error rate as the focus of this chapter is on comparing parametric metrics with SUV. Confirmation of the physiologic findings from this study will require a larger sample size with an appropriate correction for multiple comparisons. Finally, the kinetic model for ROI-based analysis and parametric imaging (*130,173*) used in this chapter followed a commonly used two-tissue model for analyzing ^{18}F-FDG data and considered time delay and organ-specific input functions. More advanced and organ-specific compartmental models could be investigated, e.g., the three-tissue model (*112*) and the recent high-temporal resolution model (*186*) for the lungs. We are currently investigating such models.

Our next steps are to use a similar methodology and more advanced models to study the impact of long COVID-19 on individual subjects. The interplay and correlation of tracer kinetics among different organs will be of interest. In addition, the results from this pilot work suggest future study designs should focus more on immune-related metabolic changes, e.g., by tracking macrophage (*187*) or neutrophil (*188*) recruitment or monitoring serum inflammatory factors to gain a deeper understanding of the prolonged impact of COVID-19 on glucose metabolism.

4.5. Conclusion

With total-body multiparametric PET, increased lung ^{18}F-FDG metabolism (measured by K_i) and increased bone-marrow ^{18}F-FDG delivery (measured by K_1) were detected in recovering COVID-19 subjects as compared to healthy subjects. The changes may be associated with continued inflammation and immune response during the early stages of recovery from COVID-19. Vaccination may have a protection effect. These findings are otherwise missed or not possible to find if standard SUV measures are used. Total-body multiparametric ^{18}F-FDG PET can be a more sensitive tool than conventional whole-body static ^{18}F-FDG imaging for detecting subtle changes and may be used for studying post-acute sequelae of COVID-19.

Chapter 5. Exploration of Deep Learning for Total-Body Parametric Imaging

5.1. Introduction

As the data amount acquired by the total-body dynamic PET imaging is unprecedentedly huge, conventional kinetic modeling methods, such as the model-fitting based (*69*,*122*) compartmental modeling, can be time-consuming for total-body parametric imaging owing to the iterative fitting algorithm (*75*,*76*) for millions of body voxels. Besides, an additional step of kinetic model selection, i.e., to select the appropriate kinetic model for each body voxel, has been shown to be important for total-body parametric imaging (*69*). This process further increases the computational burden for total-body parametric imaging. As a result, conventional methods for total-body parametric imaging can take several hours per subject, and there is a need for more efficient methods.

Deep learning has the potential to present feasible and efficient tools for total-body parametric imaging (*156*). Once the deep learning models are trained, they can provide high-speed prediction. In addition, the noise-reduction ability of deep learning (*95*,*189*) endows it with the potential to improve the parametric image quality compared to conventional methods.

In this chapter, we explore deep learning for total-body parametric imaging, pursuing efficient alternatives for the time-consuming conventional methods. In Section 5.2, we use deep learning for total-body voxel-wise model selection. In Section 5.3, we apply deep learning for the total-body voxel-wise kinetic parameter quantification.

5.2. Total-Body Kinetic Model Selection Using Single-Subject Deep Learning

5.2.1. The Problem

In conventional PET parametric imaging with a limited field of view, only one kinetic model (e.g., the two-tissue compartmental model) is used for modeling all image voxels. However, this may not be appropriate for total-body parametric imaging, as the appropriate tracer model varies in different organs in the body and cannot be described by a single model. Voxel-wise kinetic model selection has been shown to overcome this problem by adaptively choosing the best of two or more candidates for each voxel (*69*). Conventional methods for model selection calculate a statistical metric such as the Akaike information criterion (AIC) by fitting each time-activity curve (TAC) with all candidate models (*96*,*190*). These methods, however, can have high computational costs for total-body parametric imaging due to the need to perform kinetic modeling for all candidate models over a large number of body voxels (e.g., ~10 million). Hence, effective and efficient deep learning methods are desired for the voxel-wise kinetic model selection for total-body parametric imaging.

In addition to the efficiency, another problem lay in the preparation of the training database. A common approach for deep learning is based on a large patient population database for model training, which may not be available yet for dynamic PET. Specifically, as each patient has only one blood input function, it is high-demanding to prepare a population-based dataset of input functions, and the generalization capability of a trained model based on the population data remains a concern. Hence, methods reducing the reliance on the population data would be valuable.

5.2.2. Materials and Methods

5.2.2.1. Voxel-wise model selection using AIC

The Akaike information criterion (AIC) is a commonly used method for model selection (Eq. 2.5) (*96*,*134*,*191*). It is a balance between the curve fitting error and the model complexity, and a smaller value indicates a better model fitting quality. As a proof of concept, this work focuses on a binary model selection problem. For each voxel, we select the best of two kinetic models A (e.g., one-tissue compartmental model) and B (e.g., two-tissue compartmental model) using the difference between the two AICs:

$$\Delta\mathrm{AIC} = \mathrm{AIC}_A - \mathrm{AIC}_\mathrm{B}, \qquad \text{Eq. 5.1}$$

where AIC_x ($x = A$ or B) is calculated from the residual sum of squares of the TAC fit and the number of unknown parameters in the model x (Eq. 2.5). If $\Delta\mathrm{AIC} < 0$, model A is selected; otherwise, model B is selected. For calculating $\Delta\mathrm{AIC}$, the TAC of each voxel needs to be fitted twice using the two models, which is computationally expensive due to the huge number of voxels in the total-body context.

5.2.2.2. Proposed Single-Subject Deep Learning Method

We propose a deep learning-based method for the fast prediction of $\Delta\mathrm{AIC}$ from TAC data. To avoid the need for a population-based training data base, we propose a deep learning method on a single-subject basis (Figure 5.1) with both training and testing data sharing the same input function.

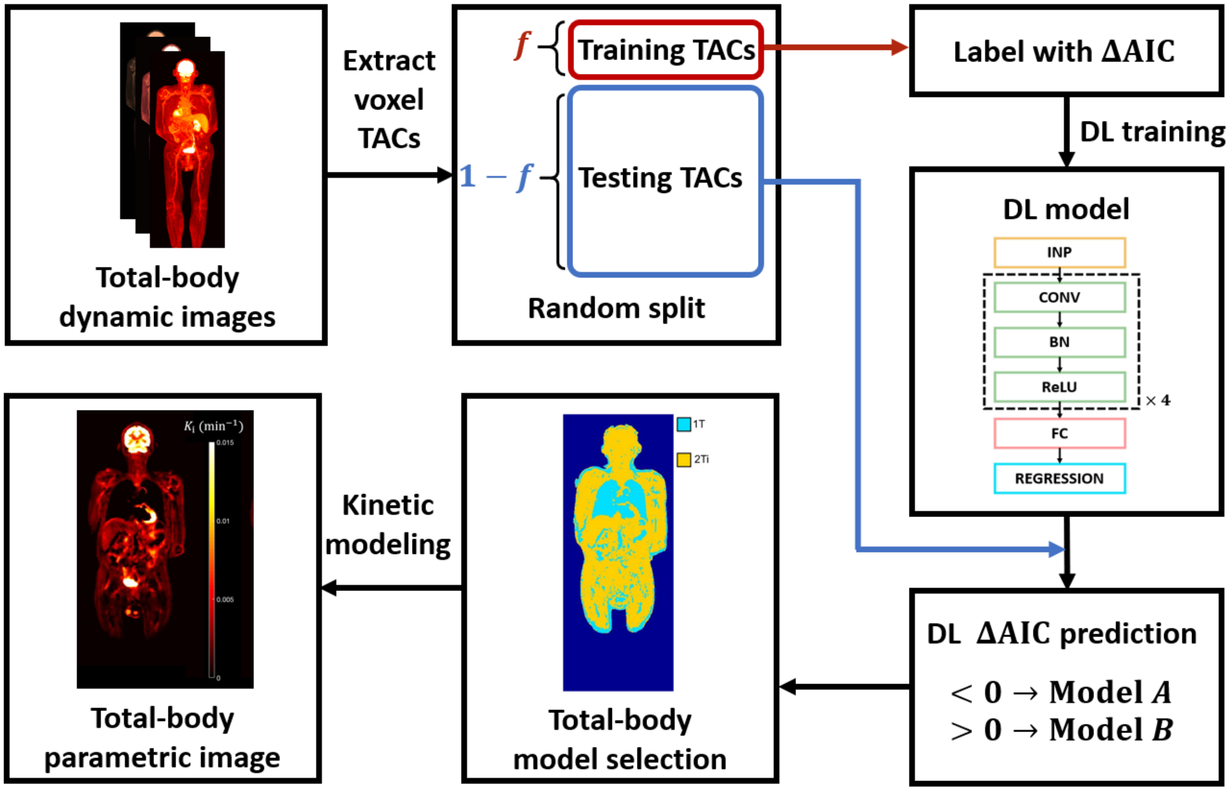

Figure 5.1. Flow chart of the proposed single-subject deep learning for kinetic model selection. The total-body time-activity curves (TACs) are randomly split into the training TACs with the fraction f and the testing TACs with the fraction $1-f$. The training TACs are fitted with the two candidate models and are labeled with the AIC difference (ΔAIC) of the two models (Eq. 5.1) to make up the training data. The deep learning (DL) model is then trained with the training data and then predicts the ΔAIC for the testing TACs. The testing TACs with positive predicted ΔAIC are labeled with model A and otherwise model B to generate the total-body model selection map. Voxel-wise compartmental modeling is performed according to the model selection map to obtain the total-body parametric image.

Suppose there are N voxels in the total-body PET image of the studied subject. The proposed deep learning method randomly splits the N image voxels into two subsets: the training set with a fraction of f $(0 < f < 1)$ and the testing set with a fraction $(1-f)$. The input of the deep learning model is the TAC of a voxel, and the output is the corresponding ΔAIC that is generated using the conventional nonlinear fitting-based

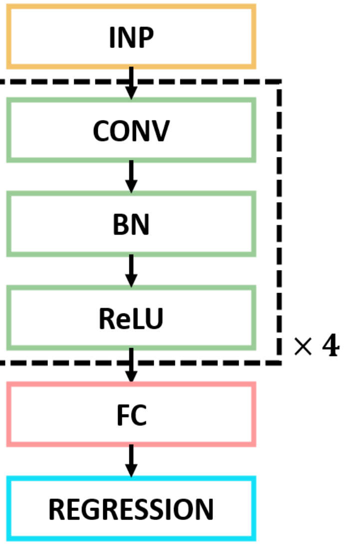

INP: Input layer.

CONV: Convolutional layer.

With 64 filters.

Each filter is 29x1.

BN: Batch normalization layer.

ReLU: Rectified Linear Unit layer.

FC: Fully connected layer.

REGRESSION: Regression layer.

Figure 5.2. The architecture of the CNN in the proposed deep learning model selection.

method. After the deep learning model training with the pairs of TACs and ΔAIC values in the training set, the network is used to predict the ΔAIC for the testing set voxels. Voxels with negative ΔAIC are labeled as model A. Otherwise, they are labeled as model B.

The proposed single-subject deep learning can accommodate various types of deep learning models. In this work, a convolutional neural network (CNN) is used (*192*) because the convolution layers may mimic the convolution formula of the impulse response function of compartmental models (Eq. 1.7). The CNN we use contains four convolutional layers (Figure 5.2), each with 64 1D temporal filters, and the filters have the same length as the TAC. Each convolutional layer is followed by a batch-normalization (BN) layer and a rectified linear unit (ReLU) layer. A fully connected layer is followed by the four-fold repeated structures of convolution-BN-ReLU and serves as the output of the network. The loss function used for model training is the mean squared error between the ground truth and the predicted values of the ΔAIC:

$$\text{Loss} = \frac{1}{N_\mathrm{f}}\sum_{n=1}^{N_\mathrm{f}}\left(\Delta\mathrm{AIC}_{n,\mathrm{GT}} - \Delta\mathrm{AIC}_{n,\mathrm{Pred}}\right)^2, \qquad \text{Eq. 5.2}$$

in which $\Delta\mathrm{AIC}_{n,\mathrm{GT}}$ and $\Delta\mathrm{AIC}_{n,\mathrm{Pred}}$ are the ground truth and the network predicted ΔAIC of the n^{th} of the total N_f training TACs. An alternative to using ΔAIC as the training label would be to use the kinetic model type directly. The reason we use the ΔAIC rather than the preferred kinetic model type as the training label is that the former provides a quantitative representation of the probability of the better model (*193*,*194*), and its amplitude can reflect the certainty of model selection. The deep learning model was trained with an Nvidia RTX 2080Ti GPU.

5.2.2.3. Acquisition of Total-Body ^{18}F-FDG-PET Dynamic Images

Four subjects with genitourinary cancer were injected with ~10 mCi ^{18}F-FDG before scanned on the uEXPLORER PET/CT system for an hour. The list-mode data were reconstructed into 29 total-body frames: 6×10 s, 2×30 s, 6×60 s, 5×120 s, 4×180 s, and 6×300 s. Each subject had N=7–10 million isotropic voxels of 2.344 mm. For each subject, an image-derived input function was extracted from the left ventricle with careful ROI placement to reduce the partial volume and spill-over effects from the myocardium.

5.2.2.4. Total-Body Parametric Imaging with Model Selection

We used the one-tissue (1T) compartmental model as model A and the two-tissue irreversible (2Ti) compartmental model as model B. Both models incorporated the time delay correction for the input function. The 1T model leads to a ^{18}F-FDG net influx rate

$K_\mathrm{i} = 0$, and the 2Ti model has $K_\mathrm{i} = \frac{K_1 k_3}{k_2 + k_3}$. Use of the 2Ti model only would result in incorrect high K_i values in some blood voxels. Total-body K_i images were generated with and without model selection.

5.2.2.5. Evaluation Metrics

The performance of the deep learning model selection was evaluated using the AIC-based method as the gold standard. Among the total N voxels in a total-body image, we define N_s as the number of voxels where deep learning gave the same model selection as the reference. The accuracy of the deep learning method is

$$\mathrm{Accuracy} = \frac{N_S}{N}. \qquad \text{Eq. 5.3}$$

As the generation of the model selection map can be deemed as an image segmentation task, we also use the Dice coefficient (*195*), a common metric in segmentation, for the sets of voxels preferring model A or B:

$$\mathrm{Dice}(x) = 2\frac{|x_\mathrm{Pred} \cap x_\mathrm{GT}|}{|x_\mathrm{Pred}| + |x_\mathrm{GT}|}, \quad x = A \text{ or } B. \qquad \text{Eq. 5.4}$$

x_GT and x_Pred ($x = A$ or B) are the set of voxels preferring model x given by the ground-truth method and the deep learning prediction, respectively.

We also assessed the impact of deep learning model selection on image quality. The normalized root mean squared error (RMSE) of K_i images with the deep learning model selection were calculated and converted in the unit of dB:

$$\text{Normalized RMSE (dB)} = 20\log_{10}\left(\sqrt{\frac{\sum_{n=1}^{N}\left(K_{\mathrm{i,\,Pred},n} - K_{\mathrm{i,\,GT},n}\right)^2}{\sum_{n=1}^{N} K_{\mathrm{i,\,GT},n}^2}}\right), \qquad \text{Eq. 5.5}$$

in which $K_{\mathrm{i,Pred},n}$ and $K_{\mathrm{i,GT},n}$ represent the K_{i} of the n^{th} image voxel using the deep learning predicted model selection and the ground-truth AIC model selection, respectively. $n = 1,2, \ldots, N$ represents the loop over all image voxels. For comparison purposes, the normalized RMSE of K_{i} images without model selection was calculated as well.

In addition to the global image quality, we placed regions of interest (ROIs) in the left ventricle of the K_{i} parametric images to extract and examine the regional values. These values should be close to zero as the blood pool has negligible ^{18}F-FDG metabolism.

Time efficiency was compared between the total-body parametric imaging with conventional AIC-based model selection and with the proposed deep learning method. As the proposed single-subject deep learning requires model training for each subject, the time cost of deep learning included the training data preparation, model training, and model prediction.

5.2.2.6. Investigation of the Training Data Fraction f

The deep learning training fraction f is an important hyperparameter. A too-small fraction would lead to a poor generalization performance in the testing, while a too-large one results in a high training computation cost. The trade-off between the performance and the time cost was investigated.

5.2.3. Results

5.2.3.1. Accuracy of the Deep Learning Model Selection

We first tested the deep learning-based model selection on the four subjects with $f = 0.05$. The total accuracy was 90±1%, and the Dice coefficients for the 1T model and

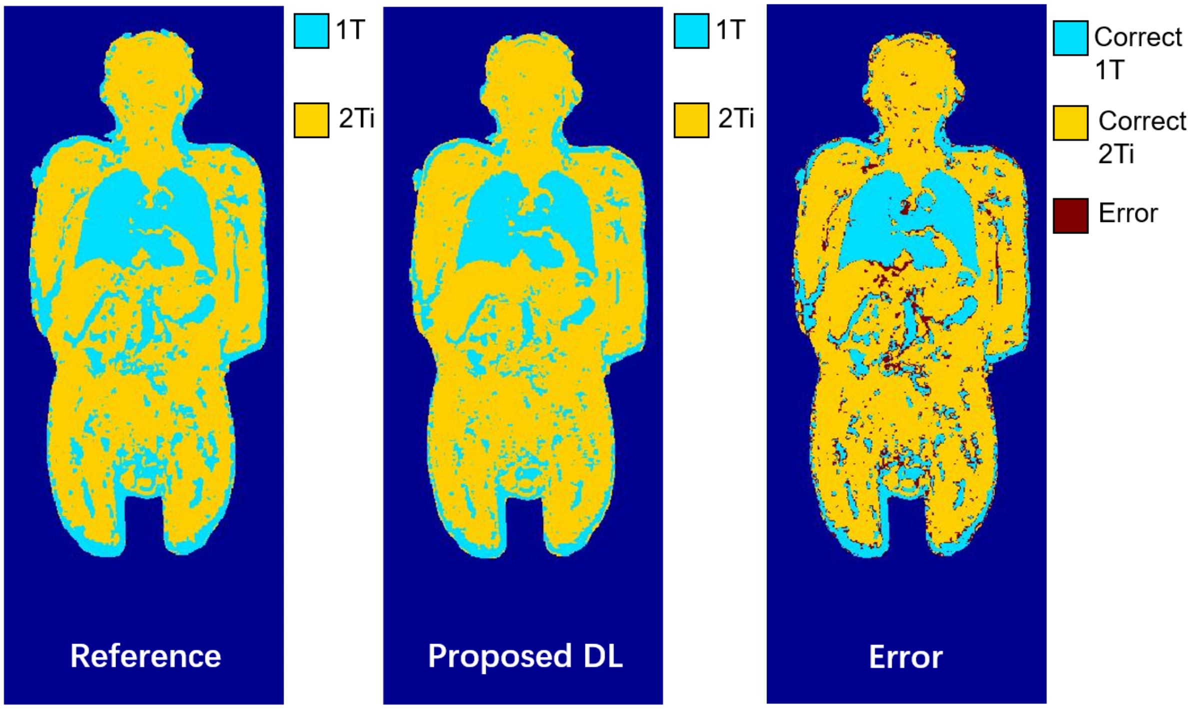

Figure 5.3. Model selection maps of one subject using the reference AIC method (left), the proposed deep learning (DL) method (middle), and the error map of the deep learning method overlaid on the model selection map (right).

the 2Ti model are 88.1%±0.2% and 91.1%±1.6%, respectively. The total-body model selection maps are shown in Figure 5.3. Most of the wrongly predicted voxels are at margins between 1T and 2Ti regions.

5.2.3.2. Effects of Training Data Fraction f

The effects of f on the accuracy of deep learning model selection and computational time are shown in Figure 5.4. When increasing f, the accuracy of the deep learning model selection increased, reaching 90% at $f \geq 0.01$. The time cost of the deep learning method (including both the training and total-body prediction) increased linearly for $f > 0.05$. $f = 0.05$ may be a good trade-off, as it had a good accuracy and took only 15 minutes.

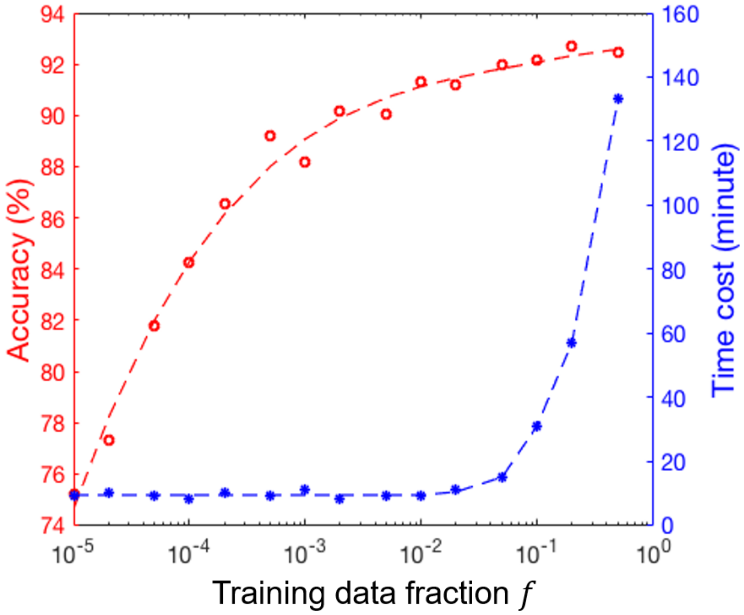

Figure 5.4. Effects of the training data fraction f on the accuracy (left axis) and the time cost (right axis) of the deep learning method in one subject.

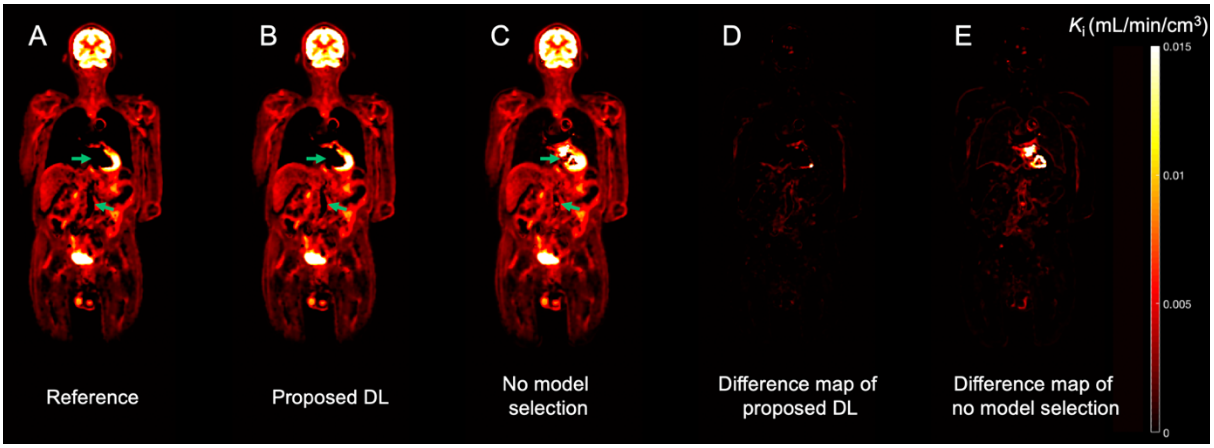

Figure 5.5. Total body K_i image with the reference model selection (A), with the proposed deep learning (DL) model selection (B), and with no model selection (C). The difference images relative to the reference are also displayed for the proposed DL (D) and for no model selection (E).

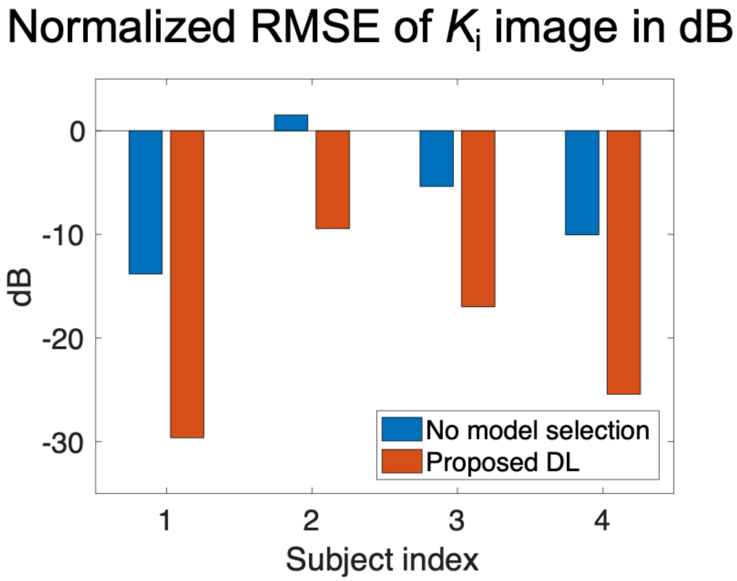

Figure 5.6. The normalized RMSE (dB) of total-body K_i images with no model selection and with the proposed deep learning (DL) model selection.

5.2.3.3. Impact of Deep Learning Model Selection on Parametric Images

The effects of model selection on total-body K_i images are shown in Figure 5.5. Without model selection (i.e., 2Ti only), the image shows artificially high values in the blood regions, e.g., ventricle and descending aorta (shown with arrows). Voxel-wise model selection corrected these artifacts by selecting the 1T model over the 2Ti model. The K_i image by the deep learning method is very close to that of the reference method. Compared to no model selection, the image RMSE was decreased from -7 ± 7 dB to -20 ± 9 dB (Figure 5.6) after applying the deep learning method. The ROI-based values of K_i extracted from the left ventricle cavity are further shown in Figure 5.7. The values of the reference AIC model selection and the proposed deep learning are close to each other while those with no

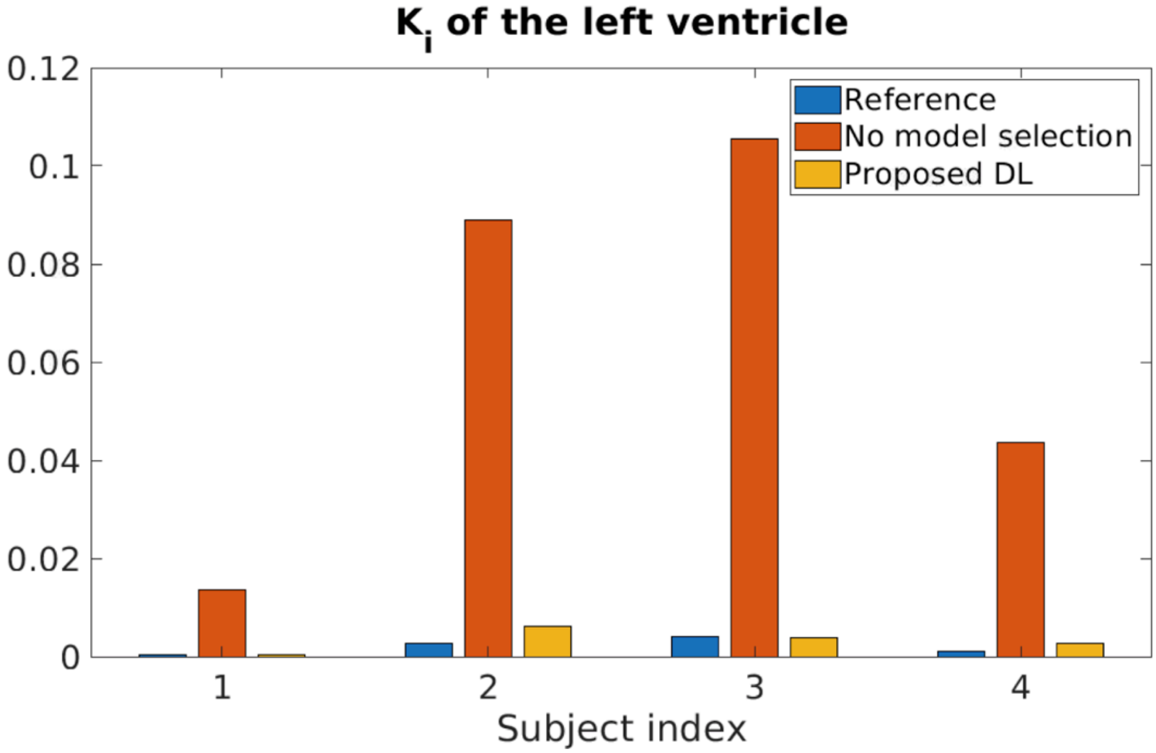

Figure 5.7. Region of interest (ROI) based quantification of the K_i of the left ventricle by methods with different model selection settings.

model selection can be falsely high. Compared to the reference method, the total time for generating the total-body K_i image decreased from 7.1 hours to 2.5 hours using the deep learning method.

5.3. Total-Body Parametric Imaging with Deep Patlak

5.3.1. The Problem

Compartmental modeling is a standard method for estimating the tracer influx rate K_i. The kinetic parameter quantification is performed through the non-linear fitting of the tissue TAC $C_\mathrm{T}(t)$, usually with iterative algorithms, such as the Levenberg–Marquardt algorithm (75,76). However, compartmental modeling can be time-consuming for total-body parametric imaging owing to the need to process millions of voxel-wise TACs.

The conventional Patlak plot (Eq. 1.12) *(77)* is a fast alternative for K_i estimation. However, it is less accurate due to model simplification. The Patlak plot neglects the correction of fractional blood volume in the tissue activity (i.e., the $(1 - v_\mathrm{b})$ in Eq. 1.9), leading to the Patlak-estimated K_i closer to $(1 - v_\mathrm{b})K_\mathrm{i}$ by compartmental modeling. While this approximation is acceptable for organs with small v_b such as the brain (<5%), it becomes inappropriate for the total-body parametric imaging and can lead to an underestimation of K_i for highly vascularized tumors (*121*). In addition, the setting of the steady-state time t^* is empirical and can influence K_i quantification.

Given the limitations of compartmental modeling and the conventional Patlak plot, there is a need for accurate and efficient methods for total-body parametric imaging of K_i. Deep learning is promising to offer good solutions. Beyond accuracy and efficiency, the interpretability of deep learning models is an important point to consider, as previous studies usually applied commonly used models or networks (*97–102*) without a thorough understanding of how the models solve the specific kinetic modeling tasks. Hence, we aim to develop deep learning approaches that are more explainable.

5.3.2. Materials and Methods

5.3.2.1 Revisit of the Conventional Patlak Plot Method

The conventional Patlak method for K_i estimation from the blood input function $C_\mathrm{p}(t)$ and tissue TAC $C_\mathrm{T}(t)$ using Eq. 1.12. The equation describes a linear relationship between the sequence terms $\frac{C_\mathrm{T}(t)}{C_\mathrm{p}(t)}$ and $\frac{\int_0^t C_\mathrm{p}(\tau)\mathrm{d}\tau}{C_\mathrm{p}(t)}$ among time points after the steady time t^*.

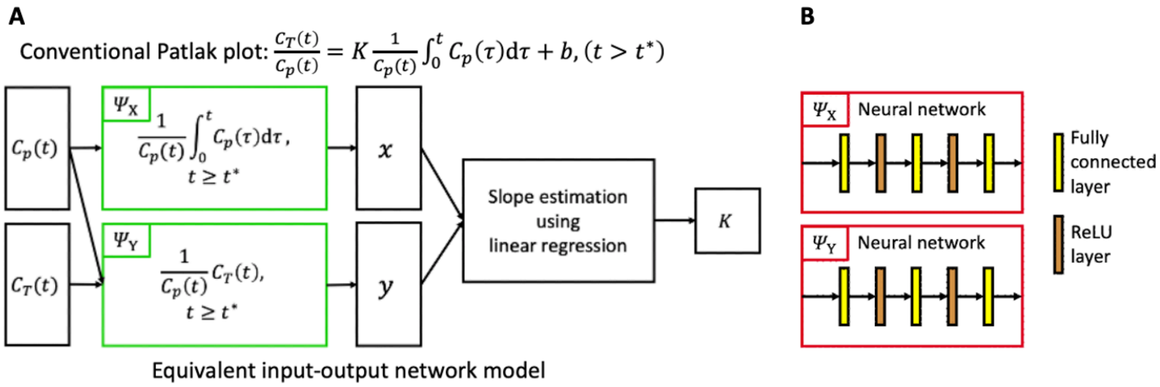

Figure 5.8. (A) Equivalent input-output network of the conventional Patlak plot with the nonlinear transformations Ψ_X and Ψ_Y in closed-form expressions. (B) Ψ_X and Ψ_Y are replaced with neural networks in the proposed Deep Patlak model.

Consequently, K_i, viewed as the slope, can be estimated via the least-square linear regression between the two sequence terms:

$$K_i = \frac{\sum_{i=1}^{M}(x_i - \bar{x})(y_i - \bar{y})}{\sum_{i=1}^{M}(x_i - \bar{x})^2} \qquad \text{Eq. 5.6}$$

in which $i = 1,2,\ldots,M$ represents the time frames after t^*; x_i and y_i represent the values of $\frac{\int_0^t C_p(\tau)\mathrm{d}\tau}{C_p(t)}$ and $\frac{C_T(t)}{C_p(t)}$, respectively. $\bar{x}$ and $\bar{y}$ are the average values, i.e., $\bar{x} = \frac{1}{M}\sum_{i=1}^{M} x_i$, and $\bar{y} = \frac{1}{M}\sum_{i=1}^{M} y_i$.

One critical observation from the revisit is that the computation process of the Patlak plot can be represented with an equivalent input-output network (Figure 5.8A). The nonlinear transformations $x = \Psi_X\left(C_p(t)\right)$ and $y = \Psi_Y\left(C_p(t), C_T(t)\right)$ convert the TACs of $C_p(t)$ and $C_T(t)$ into sequences x and y. In the conventional Patlak plot, Ψ_X and Ψ_Y are model-driven with closed-form expressions:

$$\Psi_X = \frac{\int_0^t C_p(\tau)\mathrm{d}\tau}{C_p(t)}, \Psi_Y = \frac{C_T(t)}{C_p(t)}. \qquad \text{Eq. 5.7}$$

Then, x and y are input to an equivalent linear regression layer following Eq. 5.6, and the resulting slope is the Patlak-plot estimation of K_{i}.

5.3.2.2. Proposed Deep Patlak Method

In the proposed Deep Patlak, we hypothesize that the transformations Ψ_{X} and Ψ_{Y} are imperfect if defined with the analytical format (Eq. 5.7). Hence, we propose revising them to be data-driven, as implemented by two neural networks (Figure 5.8B):

$$\Psi_{\mathrm{X}} = \mathrm{NN}_{\mathrm{X}}\left(C_p(t)\right),\ \Psi_{\mathrm{Y}} = \mathrm{NN}_{\mathrm{Y}}\left(C_{\mathrm{p}}(t), C_{\mathrm{T}}(t)\right), \qquad \text{Eq. 5.8}$$

in which NN_{X} and NN_{Y} represent the neural networks. Hence, the sequences x and y are produced by the neural networks. Then, same as the conventional Patlak plot, the slope between x and y is analytically calculated with the linear least-square regression as Eq. 5.6.

Various sequence-to-sequence networks can serve as the NN_{X} and NN_{Y}. As a proof of concept, fully connected networks are used here. The network has three fully connected layers, each with 50 neurons, and two ReLU layers. To train the Deep Patlak network, we use the input function $C_{\mathrm{p}}(t)$, voxel tissue TACs $C_{\mathrm{T}}(t)$ derived from total-body dynamic images and corresponding K_{i} values estimated by the gold-standard compartmental modeling *(69)*. We employed a mean squared error loss function between the K_{i} estimated by the compartmental modeling $K_{\mathrm{i,CM}}$, and those predicted by the network $K_{\mathrm{i,DP}}$. Similar to Section 5.2, the Deep Patlak was tested with the strategy of single-subject deep learning with the training data fraction $f = 10\%$. The value 10% was chosen based on our initial investigations. Hence, the mean squared loss function with the single-subject deep learning strategy is:

$$\text{Loss} = \frac{1}{N_\text{f}}\sum_{n=1}^{N_\text{f}}\left(K_\text{i,CM} - K_\text{i,DP}\right)^2. \qquad \text{Eq. 5.9}$$

Again, N_f is the number of training voxels, and $n = 1,2,\dots,N_\text{f}$ is the loop over all training voxels.

5.3.2.3. Acquisition of Total-Body Dynamic Images

We tested the Deep Patlak method for total-body K_i parametric imaging in 16 subjects (nine healthy and seven cancer patients), each with an ^{18}F-FDG dynamic scan on the uEXPLORER PET/CT system for one hour. The data were reconstructed into 29 frames: 6×10 s, 2×30 s, 6×60 s, 5×120 s, 4×180 s, 6×300 s with an isotropic voxel size of 4 mm. The image-derived input function was obtained from the ROI placed in the ascending aorta. For an ROI-based analysis of the parametric image, additional ROIs were placed in the gray matter and the liver of each subject. Furthermore, a total of 35 tumors/lesions were identified from the cancer subjects, and corresponding ROIs were placed.

5.3.2.4. Comparison of the Deep Patlak with the Conventional Patlak

To demonstrate the advancement of the proposed Deep Patlak compared with the conventional Patlak, the root-mean-squared error (RMSE) of $K_\text{i,DP}$ taking $K_\text{i,CM}$ as the gold standard was calculated for both the ROI quantification and the global image quality.

$$\text{RMSE} = \sqrt{\frac{1}{N}\sum_{n=1}^{N}\left(K_{\text{i,DP},n} - K_{\text{i,CM},n}\right)^2}, \qquad \text{Eq. 5.10}$$

in which $n = 1,2,\ldots,N$ represents the loop over all TACs for the ROI quantification and the loop over all image voxels for the global image quality. For comparison purposes, the RMSE of the conventional Patlak estimation was also calculated.

In addition, time costs were also compared across the methods. As the single subject deep learning strategy was applied, the time cost of the Deep Patlak includes the training data preparation, model training, and model prediction (similar to Section 5.2.2.5), which uses an Nvidia RTX 2080Ti GPU.

5.3.2.5. Comparison of the Deep Patlak with the Common Neural Network

To evaluate the performance of the Deep Patlak compared to commonly used neural networks, we tested a fully connected network in which there are three fully connected layers and two ReLU layers. The amount of network parameters is approximately the same as in the Deep Patlak neural network. This common neural network for comparison took $C_{\mathrm{p}}(t)$ and $C_{\mathrm{T}}(t)$ as the input and output the estimated K_{i}. We used the same single-subject strategy and trained the network with the same loss function and the same training data. The total-body image RMSE was compared between Deep Patlak and the common neural network.

5.3.3. Results

5.3.3.1. Efficacy of the Deep Patlak for Total-Body Parametric Imaging

The total-body parametric images of a cancer subject generated by different methods are shown in Figure 5.9A. Compared with the gold-standard compartmental modeling, the conventional Patlak underestimated lesion K_{i}, especially for some

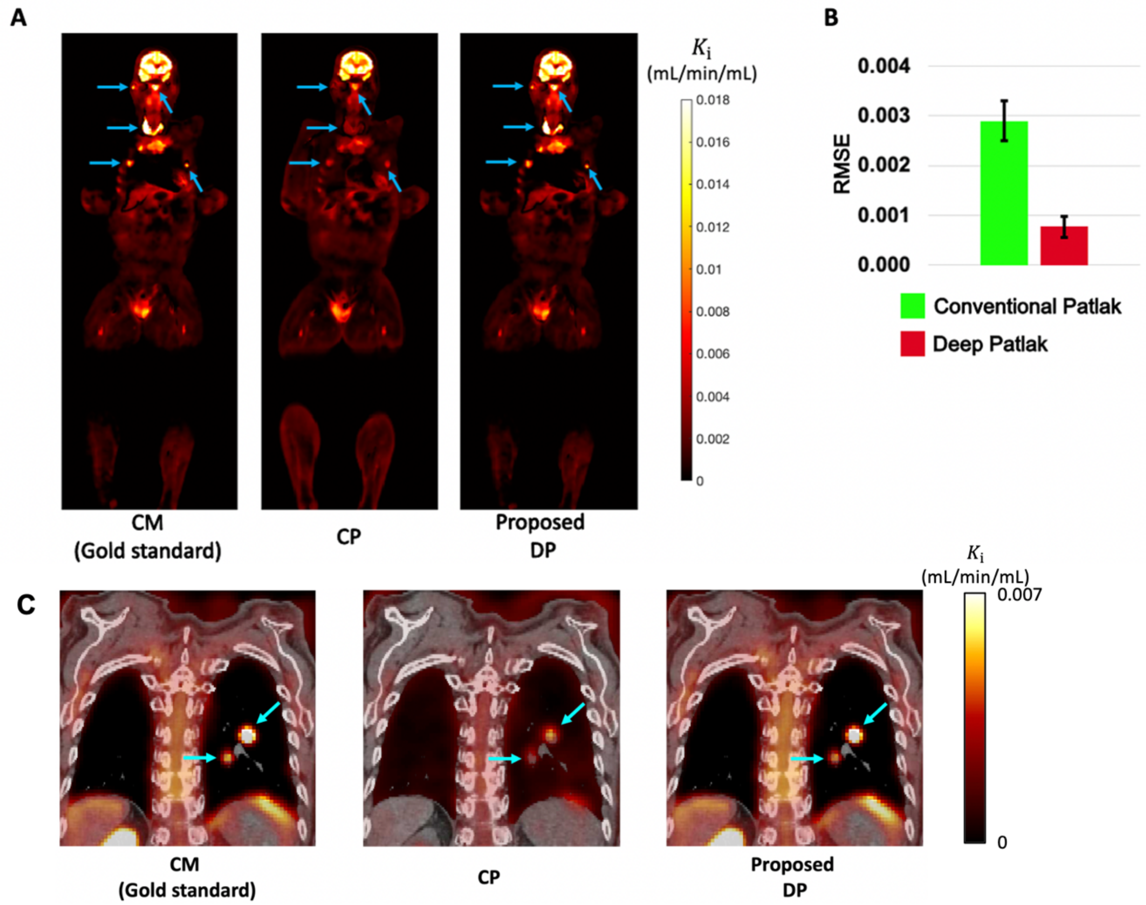

Figure 5.9. (A) Total-body K_i parametric images of an example cancer subject obtained with compartmental modeling (CM) (gold standard), the conventional Patlak (CP), and the proposed Deep Patlak (DP) methods. (B) Image RMSE of the CP and DP methods for total-body K_i imaging averaged from the 16 subjects. (C) Parametric images K_i of lung metastases (pointed by arrowheads) generated by the three methods overlaid on the corresponding CT slice.

tumors/lesions. The proposed Deep Patlak overcame this problem, and the generated parametric image closely resembled the one by compartmental modeling. More quantitatively, the global image RMSE showed a decrease of ~75% by the Deep Patlak (0.00078±0.00023) compared to the conventional Patlak (0.0029±0.0004) (Figure 5.9B). Parametric images of lung metastases were examined (Figure 5.9C), and the proposed Deep Patlak had a stronger tumor contrast than the conventional Patlak.

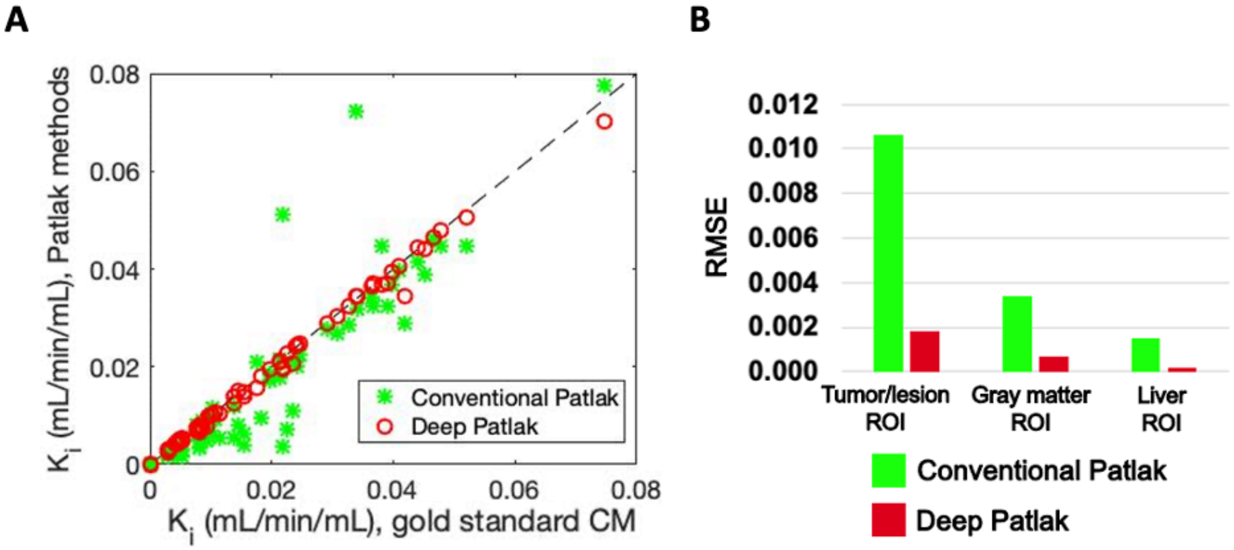

Figure 5.10. (A) Scatter plot of ROI-based quantifications of the conventional Patlak and the proposed Deep Patlak methods of 67 ROIs from the 16 subjects. (B) RMSE of categorized ROIs (35 tumors/lesions, 16 gray matters, and 16 livers) using the Patlak methods.

The ROI-based analysis of the parametric images is shown in Figure 5.10. The scattered plot in Figure 5.10A shows the pooled results of all the ROIs from gray matter, liver, and tumor/lesion. The Deep Patlak largely improved the K_i quantification compared with the conventional Patlak plot, indicating that the transformations Ψ_X and Ψ_Y are enhanced by the data-driven networks (Eq. 5.8) compared to the original analytical formula (Eq. 5.7). This is further supported by the RMSE of the categorized ROIs (Figure 5.10B), in which the RMSE of Deep Patlak was ~80% lower.

5.3.3.2. Comparison with the Common Neural Network

The RMSE for the total-body parametric imaging of the common network is 0.00078±0.00021, very close to that of the Deep Patlak (0.00078±0.00023). This result indicates the difference between the Deep Patlak and the common neural network is small.

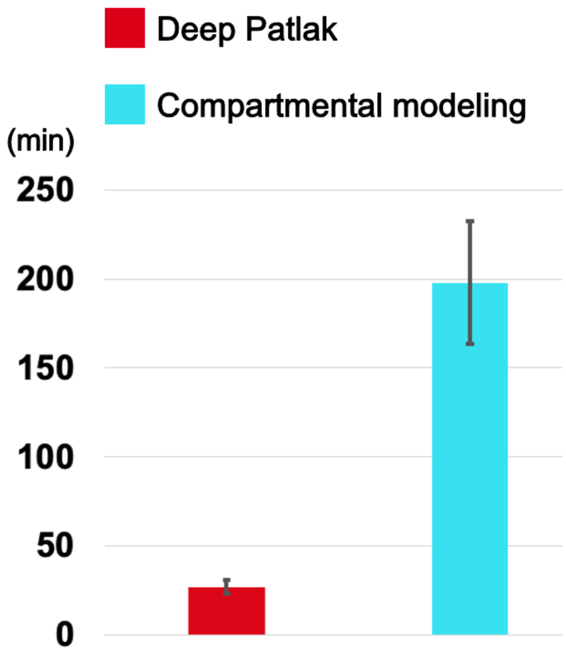

Figure 5.11. Time cost for total-body parametric imaging of compartmental modeling and the proposed Deep Patlak. The results are averaged from the 16 subjects.

5.3.3.3. Efficiency in Time

The average time cost for total-body parametric imaging is less than 0.5 hours per subject by the Deep Patlak method (Figure 5.11), demonstrating better efficiency compared to the compartmental modeling method, which takes ~3.3 hours per subject.

5.4. Discussion

In this chapter, we explored deep learning for total-body parametric imaging and obtained methods with increased efficiency compared with conventional kinetic modeling methods. We targeted the total-body voxel-wise model selection in Section 5.2 and proposed the single-subject deep learning strategy, which is a practical solution to avoid the demand for a population database for model training. Through the preliminary tests, we find it is practically feasible to separate the total-body voxels into the training and the testing groups, and the deep learning models have good performance even when trained with data from a small fraction (e.g., 5%) of the body voxels. The single-subject deep learning was further validated with the kinetic parameter quantification with the Deep Patlak in Section 5.3,

Although this single-subject strategy has the capability to largely decrease the requirement of data, one major adversity is the added time cost of training data preparation and model training, as these steps are required for each subject. Hence, it is still highly desired to develop a population-based model for total-body parametric imaging. The single-subject deep learning will also help as a benchmark for model performance. Future studies can explore how the population-based model approaches or even exceeds the accuracy of the single-subject model with the gradual increase of available population training data. This investigation will also instruct about the decent size of a population database.

For the specific task of kinetic model selection, if there are multiple candidate kinetic models, the use of the cross-entropy loss function (*196*) is worth further investigation:

$$\text{Loss} = -\sum_{n=1}^{N}\sum_{m=1}^{M} y_{n,m}\log\left(\hat{y}_{n,m}\right). \qquad \text{Eq. 5.11}$$

$n = 1,2,\dots,N$ represents a total of N voxels, $m = 1,2,\dots,M$ represents a total of M candidate kinetic models. $y_{n,m}$ and $\hat{y}_{n,m}$ are the label and the deep learning prediction for the n^{th} voxel regarding the m^{th} candidate model, respectively. The value of $y_{m,n}$ can be a one-hot encoded vector (1 for the best kinetic model, and 0 for others), or the Akaike weight

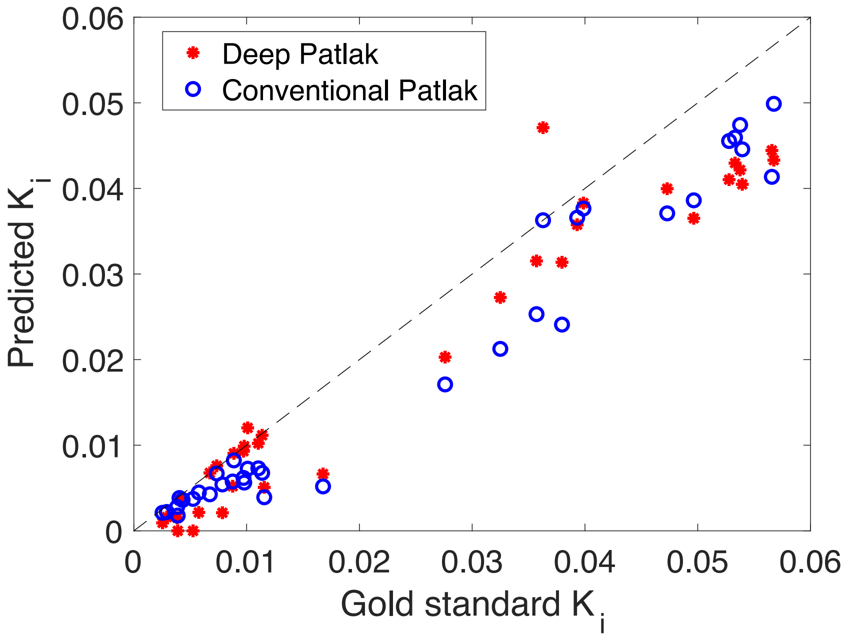

Figure 5.12. Scatter plot of the estimation of the K_i for 35 lesions using the conventional Patlak and the Deep Patlak. The Deep Patlak model here was trained with the data from a healthy subject. The K_i estimated by compartmental modeling is taken as the gold standard.

$w_{n,m}$ (*197*) that represents the possibility of the m^{th} kinetic model to be the best model for the n^{th} voxel:

$$w_{n,m} = \frac{\exp(-\frac{1}{2}\mathrm{AIC}_{n,m})}{\sum_{i=1}^{M}\exp(-\frac{1}{2}\mathrm{AIC}_{n,i})}, \qquad \text{Eq. 5.12}$$

in which $\mathrm{AIC}_{n,m}$ is the AIC value of the m^{th} model for fitting the n^{th} voxel.

The proposed Deep Patlak method in Section 5.3 created a more interpretable deep learning model for parametric imaging. The network mimics the conventional Patlak plot but has the nonlinear transformations Ψ_X and Ψ_Y substituted into trainable neural networks. The evident improvement in the overall parametric image quality and the ROI-based quantification demonstrated the benefit of the proposed method. Although the Deep Patlak did not show improved performance than the common neural network, it has the advantage of being more interpretable. Future studies may enroll in further development of the Deep Patlak, for example, modification of the loss functions to better accommodate the linear regression step.

For the use of the single-subject deep learning to the Deep Patlak, it is a concern whether the latter has good performance when the training data does not include voxel TACs of disease tissue (e.g., tumors). To investigate this problem, we trained the Deep Patlak model with TACs from a healthy subject and tested its performance in K_i prediction with synthetic lesion TACs. The synthetic lesion data were generated with the kinetic parameters of 35 lesions from the genitourinary cancer subjects and the blood input function of the trained healthy subject. The results (Figure 5.12) showed that the Deep Patlak trained on the healthy subject data had a similar error level for tumor K_i prediction compared to the conventional Patlak (prediction error: -0.0051 ± 0.0260 for the conventional Patlak, -0.0044 ± 0.0258 for the Deep Patlak; correlation coefficient with the gold standard K_i: 0.970 for the conventional Patlak, 0.982 for the Deep Patlak), and the performance was worse than the Deep Patlak trained on individual cancer subjects (Figure 5.10A), indicating the potential adversity of the single-subject deep learning strategy. To address this problem, a potential solution may be to train the model with population data first and then fine-tune it with single-subject data.

Our current studies took the traditional kinetic modeling methods, such as the AIC-based model selection and the kinetic quantification through the compartmental model fitting, as the reference or gold standard for the assessment of deep learning performance.

Although we demonstrated that deep learning could approach these traditional methods with good efficiency, the unanswered question is whether the deep learning methods surpass the traditional methods in the quality of parametric imaging. Hence, further study may evaluate this topic with simulation studies and compare the conventional approaches and deep learning with the known ground truth. Another feasible way is to test the methods with low-dose dynamic data while taking the parametric images generated with high-dose dynamic data as the gold standard.

5.5. Conclusion

The deep learning implementations in this study achieved good efficiency and efficacy in the total-body voxel-wise model selection and parameter quantification. The proposed single-subject deep learning is a feasible solution to decrease the requirement for training data, and the Deep Patlak has the potential to improve model interpretability. The utilization and development of deep learning hold promise in total-body parametric imaging.

Chapter 6. Summary and Future Investigations

6.1. Summary of This Work

In this work, we studied kinetic modeling and parametric imaging with total-body PET, highlighting applications to lung disease with the potential for many other systemic diseases. The rationale and research topics covered in this thesis are summarized by the diagram in Figure 6.1. The introduction of total-body PET systems permits a paradigm shift in PET. It brings a lot of changes that include the high detection sensitivity along with the associated high image quality, the total-body field of view, and the unprecedented data amount to process. These changes permit many opportunities in PET imaging and further allow novel research in kinetic modeling and parametric imaging. Our investigations of kinetic modeling focus on these novel research topics and explore the utilization of kinetic quantifications as biomarkers for physiological insights and disease assessment. We conclude that kinetic modeling with total-body PET provides a sensitive tool for evaluating health and disease and holds significant promise to benefit human healthcare.

The first mainline research direction we explored is high-temporal resolution (HTR) kinetic modeling, accomplished by the high sensitivity of total-body PET and high-temporal resolution dynamic imaging. Our investigations of HTR kinetic modeling focus on the lung, an organ unique for its dual blood supplies from the left ventricle (LV) and the right ventricle (RV) (*81–85*) with their rapidly changing early kinetics captured by the HTR dynamic imaging. In Chapter 2, we studied HTR lung kinetic modeling of normal lungs and demonstrated the necessity of delay and dispersion corrections for the image-derived

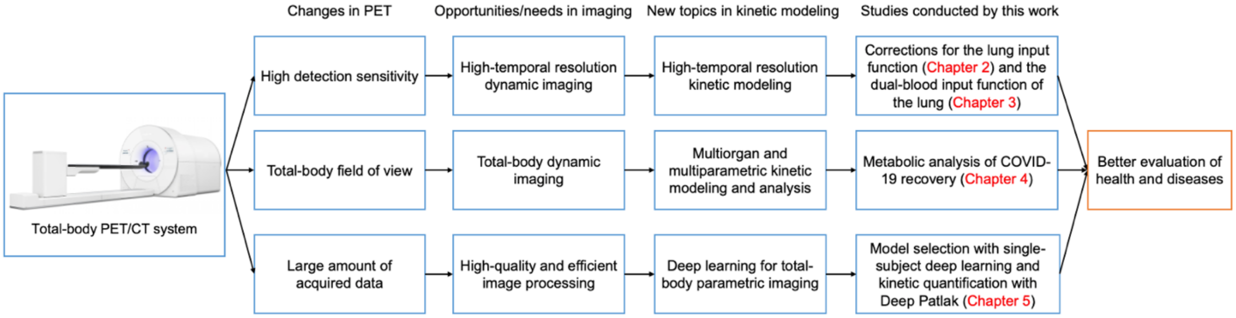

Figure 6.1. Structure diagram of this work.

input function of the RV, the dominant blood supply of normal lung tissue. The benefits include better model fitting, physiologically-reasonable quantification of fractional blood volume v_b (~0.14 compared to the reference value 0.16 and the uncorrected kinetic modeling result ~0.04), and the detected aging effect of v_b (Figure 2.7). Further, we incorporate the dual-blood input function (DBIF) for HTR kinetic modeling of lung tumors in Chapter 3 to account for their dual-blood supplies from the RV and the left ventricle (LV). The DBIF model, with the delay and dispersion corrections applied, showed further improvement in fitting. The quantified LV supply fraction f in lung tumors was significantly higher than in normal lung tissue (~0.04 vs. ~0.3, $P < 0.0003$). Our study highlights the HTR kinetic quantification with an emphasis on the early kinetics, such as f, v_b, and ^{18}F-FDG delivery rate K_1.

In addition to the high detection sensitivity, the total-body scanner also enables the simultaneous imaging of the entire body. Hence, multiorgan and multiparametric analyses of tracer kinetics are further realized, providing a promising approach for the study of systematic diseases. Therefore, we take the multiorgan and multiparametric kinetic analyses as the second mainline of this work. As an example, these analyses were applied to the evaluation of ^{18}F-FDG delivery and metabolism of COVID-19 recovery in Chapter 4. The increased lung ^{18}F-FDG metabolism in the recovering group, as represented by the net influx rate K_{i}, would be otherwise missed if only evaluated with the semi-quantitative SUV. In addition, the increase in bone marrow ^{18}F-FDG delivery through K_1 quantification shows the potential benefit of multiparametric analysis compared to only assessing the overall tracer uptake (e.g., SUV or K_{i}).

The high-temporal resolution and total-body imaging with total-body PET not only provide more advanced imaging approaches but also bring a vast amount of image data to process, spurring the need for efficient approaches. This requirement can be an excellent arena for deep learning and introduces the third mainline of this work. In Chapter 5, we implemented deep learning for total-body parametric imaging and targeted voxel-wise model selection and parameter quantification. The single-subject deep learning strategy proposed for the voxel-wise model selection is practically feasible to avoid the need for a population database for model training, while the proposed Deep Patlak enhances the deep learning model interpretability. These methods achieved good performance in parametric image quality and time cost, offering fresh perspectives to the utilization of deep learning in total-body PET imaging.

In this study, we verify and validate the kinetic modeling from various perspectives, which can be summarized by the dendrogram in Figure 6.2. These approaches fall primarily into two categories: modeling quality and indication of quantification.

The modeling quality focuses more on the math modeling side. First, it is imperative to examine the curve-fitting performance to obtain a preliminary assurance of the modeling

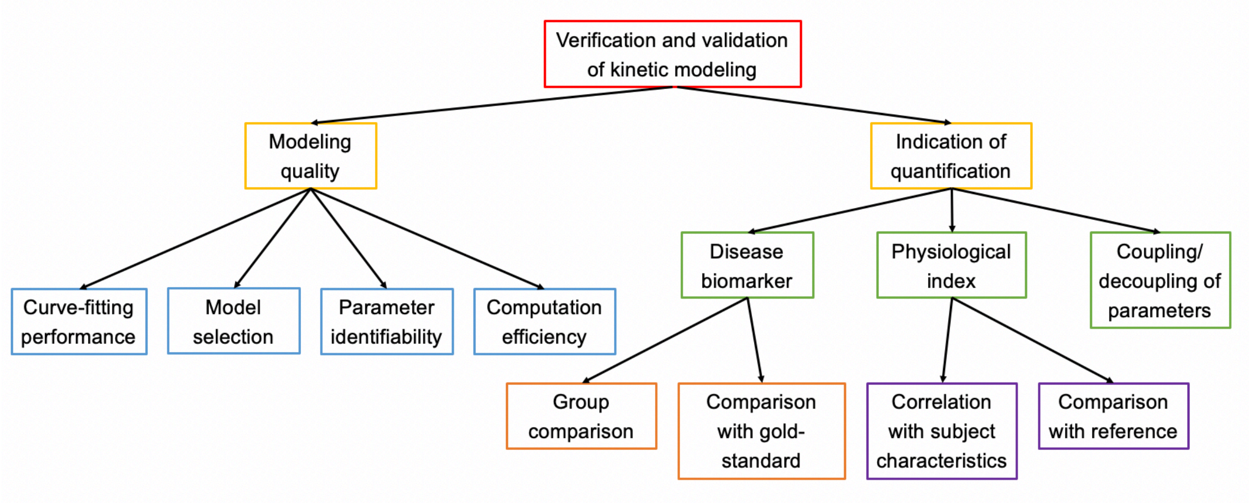

Figure 6.2. The dendrogram of the verification and validation of kinetic modeling.

feasibility (e.g., the improved fitting by the IDIF-T-D in Figure 2.3A and 2.3B and by the DBIF in Figure 3.4A). Then, kinetic model selection should be considered to confirm the improved model fitting (e.g., the AIC comparison in Figure 2.3C and Figure 3.4B) or to enhance the parametric image quality (e.g., the total-body voxel-wise model selection (*69*)). Subsequently, the robustness of kinetic quantification can be assessed with the parameter identifiability test (e.g., the test over the IDIF-T-D model in Table 2.3). Furthermore, computational efficiency is an important consideration, especially for total-body parametric imaging (e.g., the deep learning applications in Chapter 5 and the leading edge method for efficient time-delay correction (*122*)).

The indication of kinetic quantification concentrates on the physiological interpretation of the parameters and the potential utilization for health condition assessment. Specifically, the kinetic parameters may serve as physiological indices, which can be studied with their correlation with subject characteristics (e.g., the aging effect of v_b in

Figure 2.7) or the comparison with reference values (e.g., the v_{b} estimation by the proposed IDIF-T-D in Chapter 2 is closer to the literature value than without corrections). Also, the kinetic parameters have the potential to be biomarkers, which can be investigated with statistical group comparisons (e.g., the higher LV supply fraction f in lung tumors shown in Figure 3.6) or the comparison with the gold-standard diagnosis (e.g., liver K_1 vs. the liver histopathologic inflammation score (*93*)). Besides the analyses over one parameter, comprehensive insights of different parameters may be obtained through the study of their coupling or decoupling (e.g., the flow-metabolism mismatch or the transport-metabolism mismatch in the myocardium (*92*,*198*)).

The investigations conducted in this work have several limitations. First, the HTR kinetic modeling is not integrated into the multiorgan kinetic modeling in this study. As the fast tracer kinetics that the HTR data can reflect are complicated and heterogeneous among different organs, further development of organ-specific HTR kinetic models (e.g., incorporation of the interstitial space for the liver (*199*) and the independently modeled blood flow for the kidney (*200*)) is the prerequisite for the multiorgan HTR kinetic analyses. Second, the conclusions of the studies are limited by the enrolled subject number, mostly fewer than 20 per cohort. These constraints may be mitigated by larger cohort sizes in future studies and potential collaborations across institutes. Third, although the deep learning studies in Chapter 5 approach the conventional methods with an improved computational efficiency, they have not demonstrated the improvement in parametric imaging quality compared with conventional methods. Improved deep learning methods would be possible to further push the limit of the performance.

6.2. Future Investigations of Kinetic Modeling and Parametric Imaging with Total-Body PET

6.2.1. Incorporation of Multiorgan Compartmental Systems

Current PET kinetic models usually focus on the tracer kinetics of a single organ, supposing it is independent of other organs. This supposition, however, may be inaccurate in some cases where different organs may interact with each another and the interaction effect cannot be neglected. Thus, multiorgan compartment systems may be needed for a better description of tracer kinetics. One example is the combined system of the liver and gastrointestinal tract, as explored in (*201*). One possible solution is the physiologically-based pharmacokinetic (PBPK) model, which has been explored for optimizing the personalized dose in theranostics (*202–204*). However, the robustness and the benefit of this approach may need further evaluation by considering the complicated mathematical modeling.

6.2.2. Incorporation of Automatic ROI Placement

In our current workflow for kinetic modeling (Figure 1.5), most steps are performed automatically or only require minor human intervention, such as dynamic image reconstruction, kinetic model fitting, and quantification result analysis. However, ROI placement needs manual delineation. This process may be subjective, leading to differences across image readers (*205*) and can be laborious for multi-organ and multi-subject analysis (e.g., 10-50 ROIs per subject and a subject cohort of ~30). Hence, automatic ROI placement would be desired for kinetic modeling using total-body PET. It is worth noting that although there are lots of similarities, ROI placement is a different task from segmentation. The ROI placement does not necessarily need contouring of the whole organ, while it should consider minimizing the partial volume and motion effects for the best representation of the tracer kinetics of the target. Therefore, current implementations of automatic whole-body image segmentation, such as (*206*), may be adapted for automatic ROI placement.

6.2.3. Open-Access of Total-Body Dynamic Image Repository and Open-Source of Kinetic Modeling Code Package

While total-body PET kinetic modeling and parametric imaging show great potential, the availability of total-body dynamic image data and code suitable for total-body kinetic modeling remains a problem for researchers. Hence, open access data and code is an important infrastructure construction for the researcher community. Publicly-available image data will help build up a population database as a baseline group in disease evaluation or that can serve as the training data for deep learning. However, concerns of protected healthy information should be handled carefully with data anonymization and de-identification (*207*). Besides open data access, open-source code packages will decrease the technical difficulty of performing kinetic modeling and parametric imaging and help with code verification.

6.2.4. Total-Body Parametric Imaging with Reduced Dynamic Scan Time

A major obstacle for the clinical application of dynamic PET and kinetic modeling is the long image acquisition time, e.g., usually 60 min for ^{18}F-FDG, compared with static clinical PET scans which typically have a 10 - 20 min duration. This problem may be

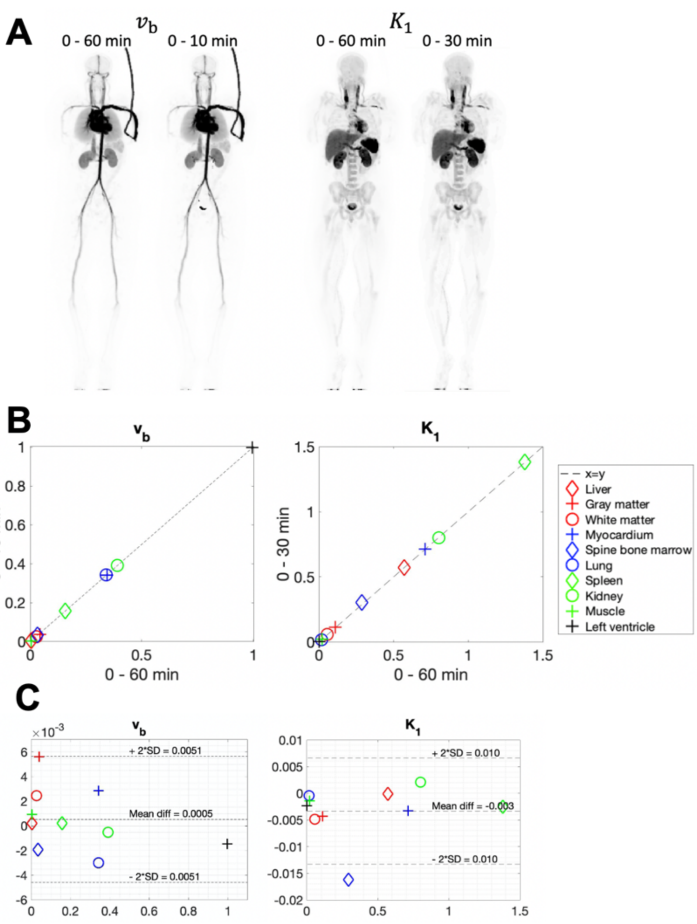

Figure 6.3. A. Parametric images of fractional blood volume v_b generated with the standard 0 - 60 min scan and the shortened 0 - 10 min scan (left) and of ^{18}F-FDG delivery rate K_1 generated with the 0 - 60 min scan and the 0 - 30 min scan (right). The images are maximum intensity projections (MIPs). B. Scatter plots of the ROI quantifications extracted from the parametric images. The x-axis is the result of the standard 0 - 60 min scan, and the y-axis is that of the shortened 0 - 10 min scan for v_b and the 0 - 30 min scan for K_1. C. The corresponding Bland-Altman plot of ROI quantifications with the two scan durations.

approached using shortened total-body dynamic PET scans, which have the potential for stable quantification of v_b and K_1 with reduced scan time, e.g., 10 min for v_b and 30 min for K_1, as shown in Figure 6.3. As we find lots of potential in v_b and K_1 as biomarkers, shortened dynamic imaging may find its clinical applications in assessing blood perfusion,

Table 6.1. Test of the Coding Ability of GPT-4 on PET Kinetic Modeling.

Task	Brief description	Domain knowledge requirement	Math difficulty	Result	Modifications needed
Parametric imaging loop	Loop over image voxels	Low	Low	Correct	0
Patlak plot	Perform the Patlak plot for K_i estimation	High	Low	Minor error in the vector size	1
Kinetic model selection	Kinetic model selection among candidate models	High	Low	Correct	0
TAC generation	Generate TACs based on a novel compartmental model	High	High	A parameter was passed wrongly due to a misunderstanding of the MATLAB function ode45.	6
Kinetic quantification	Kinetic parameter estimation through solving a set of differential equations	High	High	Error in the math formula of the kinetic model, and error in the implementation of the non-linear least square regression.	~10

The five tasks have different levels of domain knowledge requirements and math difficulties. Test results and the number of modifications to the code are also listed.

blood supply, or angiogenesis. In addition, parameters that traditionally require the 60-min dynamic scan, e.g., K_i, also have the potential to be quantified robustly with reduced scan time using novel imaging protocol (*208*) or novel tracer administration protocol (*209*). Furthermore, the development of novel tracers with fast uptake, such as FAPI (*210,211*), may enable shorter dynamic scan time compared to the 60 min as commonly used by ^{18}F-FDG dynamic scans. Hence, the application of these new tracers may offer new opportunities to apply total-body dynamic PET imaging and kinetic modeling more widely.

6.2.5. Application of Large Language Models

The recent boom of large language models (LLMs) such as ChatGPT (*212*) brings opportunities for the enhancement of the user-friendliness of PET kinetic modeling. Our test of GPT-4 (via ChatGPT) showed encouraging results regarding its coding ability for kinetic modeling (Table 6.1). In the future, LLMs may be able to perform kinetic modeling, parametric imaging, and result analysis utilizing only natural language prompts (*213*,*214*) and raw data file paths as input. Another potential usage would be the education of basic knowledge of kinetic modeling to reduce barriers for beginners or non-professionals. However, LLMs may require specific fine-tuning to minimize the risk of being misleading.

References

1. Cherry SR, Sorenson JA, Phelps ME. Positron emission tomography. In: Physics in Nuclear Medicine. 4th ed. Elsevier Health Sciences; 2012:155-172.

2. Cherry SR, Sorenson JA, Phelps ME. Tracer kinetic modeling. In: Physics in Nuclear Medicine. 4th ed. Saunders; 2012:379-405.

3. Cherry SR, Sorenson JA, Phelps ME. Modes of radioactive decay. In: Physics in Nuclear Medicine. 4th ed. Saunders; 2012:19-30.

4. Humm JL, Rosenfeld A, Del Guerra A. From PET detectors to PET scanners. *Eur J Nucl Med Mol Imaging*. 2003;30:1574-1597.

5. Gong K, Kim K, Cui J, Wu D, Li Q. The evolution of image reconstruction in PET. *PET Clin*. 2021;16:533-542.

6. Deppen SA, Blume JD, Kensinger CD, et al. Accuracy of FDG-PET to Diagnose Lung Cancer in Areas With Infectious Lung Disease: A Meta-analysis. *JAMA*. 2014;312:1227.

7. Chételat G, Arbizu J, Barthel H, et al. Amyloid-PET and 18F-FDG-PET in the diagnostic investigation of Alzheimer's disease and other dementias. *Lancet Neurol*. 2020;19:951-962.

8. Dorbala S, Di Carli MF. Cardiac PET Perfusion: Prognosis, Risk Stratification, and Clinical Management. *Semin Nucl Med*. 2014;44:344-357.

9. Bahri H, Laurence L, Edeline J, et al. High Prognostic Value of ^{18} F-FDG PET for Metastatic Gastroenteropancreatic Neuroendocrine Tumors: A Long-Term Evaluation. *J Nucl Med*. 2014;55:1786-1790.

10. Habl G, Sauter K, Schiller K, et al. ^{68} Ga-PSMA-PET for radiation treatment planning in prostate cancer recurrences after surgery: Individualized medicine or new standard in salvage treatment. *The Prostate*. 2017;77:920-927.

11. Nestle U, Schimek-Jasch T, Kremp S, et al. Imaging-based target volume reduction in chemoradiotherapy for locally advanced non-small-cell lung cancer (PET-Plan): a multicentre, open-label, randomised, controlled trial. *Lancet Oncol*. 2020;21:581-592.

12. Benz MR, Evilevitch V, Allen-Auerbach MS, et al. Treatment Monitoring by ^{18} F-FDG PET/CT in Patients with Sarcomas: Interobserver Variability of Quantitative Parameters in Treatment-Induced Changes in Histopathologically Responding and Nonresponding Tumors. *J Nucl Med*. 2008;49:1038-1046.

13. Avril S, Muzic RF, Plecha D, Traughber BJ, Vinayak S, Avril N. ^{18}F-FDG PET/CT for Monitoring of Treatment Response in Breast Cancer. *J Nucl Med*. 2016;57:34S-39S.

14. East J, Vleugels J, Roelandt P, et al. Advanced endoscopic imaging: European Society of Gastrointestinal Endoscopy (ESGE) Technology Review. *Endoscopy*. 2016;48:1029-1045.

15. Evans JA, Chandrasekhara V, Chathadi KV, et al. The role of endoscopy in the management of premalignant and malignant conditions of the stomach. *Gastrointest Endosc*. 2015;82:1-8.

16. Humphrey PA. Histopathology of Prostate Cancer. *Cold Spring Harb Perspect Med*. 2017;7:a030411.

17. Brunt EM, Tiniakos DG. Histopathology of nonalcoholic fatty liver disease. *World J Gastroenterol*. 2010;16:5286.

18. Veta M, Pluim JPW, Van Diest PJ, Viergever MA. Breast Cancer Histopathology Image Analysis: A Review. *IEEE Trans Biomed Eng*. 2014;61:1400-1411.

19. Cherry SR, Sorenson JA, Phelps ME. What is nuclear medicine? In: Physics in Nuclear Medicine. 4th ed. Saunders; 2012:1-6.

20. Pimlott SL, Sutherland A. Molecular tracers for the PET and SPECT imaging of disease. *Chem Soc Rev*. 2011;40:149-162.

21. Kayani I, Bomanji JB, Groves A, et al. Functional imaging of neuroendocrine tumors with combined PET/CT using 68Ga-DOTATATE (DOTA-DPhe1,Tyr3-octreotate) and18F-FDG. *Cancer*. 2008;112:2447-2455.

22. Cheson BD. Role of functional imaging in the management of lymphoma. *J Clin Oncol*. 2011;29:1844-1854.

23. Israel O, Kuten A. Early detection of cancer recurrence: 18F-FDG PET/CT can make a difference in diagnosis and patient care. *J Nucl Med*. 2007;48.

24. Gallamini A, Zwarthoed C, Borra A. Positron emission tomography (PET) in oncology. *Cancers*. 2014;6:1821-1889.

25. Bengel FM, Markus S. PET in clinical cardiology. In: Positron Emission Tomography: Clinical Practice. London: Springer London; 2006:413-431.

26. Jones T, Rabiner EA. The development, past achievements, and future directions of brain PET. *J Cereb Blood Flow Metab*. 2012;32:1426-1454.

27. Cherry SR, Sorenson JA, Phelps ME. Radionuclide and radiopharmaceutical

production. In: Physics in Nuclear Medicine. 4th ed. Saunders; 2012:43-62.

28. Cherry SR, Sorenson JA, Phelps ME. Decay of radioactivity. In: Physics in Nuclear Medicine. 4th ed. Saunders; 2012:31-42.

29. Cherry SR, Sorenson JA, Phelps ME. Radiation detectors. In: 4th ed. Saunders; 2012:87-106.

30. Cherry SR, Sorenson JA, Phelps ME. Electronic instrumentation for radiation detection systems. In: Physics in Nuclear Medicine. 4th ed. Saunders; 2012:107-124.

31. Cho ZH, Farukhi MR. Bismuth germanate as a potential scintillation detector in positron cameras. *J Nucl Med*. 1977;18:840-844.

32. Shao Y, Cherry SR, Farahani K, et al. Development of a PET detector system compatible with MRI/NMR systems. *IEEE Trans Nucl Sci*. 1997;44:1167-1171.

33. Pepin CM, Berard P, Perrot A-L, et al. Properties of LYSO and recent LSO scintillators for phoswich PET detectors. *IEEE Trans Nucl Sci*. 2004;51:789-795.

34. Cherry SR, Sorenson JA, Phelps ME. Interaction of radiation with matter. In: Physics in Nuclear Medicine. 4th ed. Saunders; 2012:63-86.

35. Einstein A. Über einen die erzeugung und verwandlung des lichtes betreffenden heuristischen gesichttspunkt (Concerning an heuristic point of view toward the emission and transformation of light). *Ann Phys*. 1905;4.

36. Compton AH. A quantum theory of the scattering of X-rays by light elements. *Phys Rev*. 1923;21:483.

37. Gonzalez-Montoro A, Ullah MN, Levin CS. Advances in detector instrumentation for PET. *J Nucl Med*. 2022;63:1138-1144.

38. Cherry SR, Sorenson JA, Phelps ME. Digital image processing in nuclear medicine. In: Physics in Nuclear Medicine. 4th ed. Saunders; 2012:363-378.

39. Cherry SR, Sorenson JA, Phelps ME. Tomographic reconstruction in nuclear medicine. In: Physics in Nuclear Medicine. 4th ed. Saunders; 2012:253-278.

40. Surti S, Karp JS. Update on latest advances in time-of-flight PET. *Phys Med*. 2020;80:251-258.

41. Feldkamp LA, Davis LC, Kress JW. Practical cone-beam algorithm. *J Opt Soc Am A*. 1984;1:612.

42. Lange K, Carson R. EM reconstruction algorithms for emission and transmission

tomography. *J Comput Assist Tomogr*. 1984;8:306-316.

43. Reader AJ, Zaidi H. Advances in PET image reconstruction. *PET Clin*. 2007;2:173-190.

44. Hess S, Blomberg BA, Zhu HJ, Høilund-Carlsen PF, Alavi A. The pivotal role of FDG-PET/CT in modern medicine. *Acad Radiol*. 2014;21:232-249.

45. Warburg O. On the Origin of Cancer Cells. *Science*. 1956;123:309-314.

46. Liberti MV, Locasale JW. The Warburg effect: How does it benefit cancer cells? *Trends Biochem Sci*. 2016;41:211-218.

47. Mosconi L, Mistur R, Switalski R, et al. FDG-PET changes in brain glucose metabolism from normal cognition to pathologically verified Alzheimer's disease. *Eur J Nucl Med Mol Imaging*. 2009;36:811-822.

48. Carli MFD, Geva T, Davidoff R. The Future of Cardiovascular Imaging. *Circulation*. 2016;133:2640-2661.

49. Youssef G, Leung E, Mylonas I, et al. The Use of ^{18} F-FDG PET in the Diagnosis of Cardiac Sarcoidosis: A Systematic Review and Metaanalysis Including the Ontario Experience. *J Nucl Med*. 2012;53:241-248.

50. Glaudemans AWJM, De Vries EFJ, Galli F, Dierckx RAJO, Slart RHJA, Signore A. The use of 18F-FDG-PET/CT for diagnosis and treatment monitoring of inflammatory and infectious diseases. *Clin Dev Immunol*. 2013;2013:1-14.

51. Beckers C, Ribbens C, Andre B, et al. Assessment of disease activity in rheumatoid arthritis with 18F-FDG PET. *J Nucl Med*. 2004;45:956-964.

52. Dahibom M, Hoffman E, Hoh CK, et al. Whole-Body Positron Emission Tomography: Part I. Methods and Performance Characteristics. *J Nucl Med*. 1992;33:1191-1199.

53. Wang G, Rahmim A, Gunn RN. PET parametric imaging: Past, present, and future. *IEEE Trans Radiat Plasma Med Sci*. 2020;4:663-675.

54. Reivich M, Alavi A, Wolf A, et al. Glucose metabolic rate kinetic model parameter determination in humans: The lumped constants and rate constants for [^{18}F]Fluorodeoxyglucose and [^{11}C]Deoxyglucose. *J Cereb Blood Flow Metab*. 1985;5:179-192.

55. Kubota K, Itoh M, Ozaki K, et al. Advantage of delayed whole-body FDG-PET imaging for tumour detection. *Eur J Nucl Med*. 2001;28:696-703.

56. Lortie M, Beanlands RSB, Yoshinaga K, Klein R, DaSilva JN, deKemp RA.

Quantification of myocardial blood flow with 82Rb dynamic PET imaging. *Eur J Nucl Med Mol Imaging*. 2007;34:1765-1774.

57. Greve DN, Svarer C, Fisher PM, et al. Cortical surface-based analysis reduces bias and variance in kinetic modeling of brain PET data. *NeuroImage*. 2014;92:225-236.

58. Karakatsanis NA, Lodge MA, Tahari AK, Zhou Y, Wahl RL, Rahmim A. Dynamic whole-body PET parametric imaging: I. Concept, acquisition protocol optimization and clinical application. *Phys Med Biol*. 2013;58:7391-7418.

59. Karakatsanis NA, Lodge MA, Zhou Y, Wahl RL, Rahmim A. Dynamic whole-body PET parametric imaging: II. Task-oriented statistical estimation. *Phys Med Biol*. 2013;58:7419-7445.

60. Thie JA. Understanding the standardized uptake value, its methods, and implications for usage. *J Nucl Med*. 2004;45:1431-1434.

61. Keyes JW. SUV: Standard uptake or silly useless value? *J Nucl Med*. 1995;36:1836-1839.

62. van den Hoff J, Oehme L, Schramm G, et al. The PET-derived tumor-to-blood standard uptake ratio (SUR) is superior to tumor SUV as a surrogate parameter of the metabolic rate of FDG. *EJNMMI Res*. 2013;3:1-8.

63. Chen YJ, Rosario BL, Mowrey W, et al. Relative ^{11} C-PiB delivery as a proxy of relative CBF: Quantitative evaluation using single-session ^{15} O-Water and ^{11} C-PiB PET. *J Nucl Med*. 2015;56:1199-1205.

64. Slifstein M. Revisiting an Old Issue: The Discrepancy Between Tissue Ratio–Derived Binding Parameters and Kinetic Modeling–Derived Parameters After a Bolus of the Serotonin Transporter Radioligand ^{123} I-ADAM. *J Nucl Med*. 2008;49:176-178.

65. Price JC, Klunk WE, Lopresti BJ, et al. Kinetic modeling of amyloid binding in humans using PET imaging and Pittsburgh compound-B. *J Cereb Blood Flow Metab*. 2005;25:1528-1547.

66. Zanotti-Fregonara P, Chen K, Liow J-S, Fujita M, Innis RB. Image-derived input function for brain PET studies: Many challenges and few opportunities. *J Cereb Blood Flow Metab*. 2011;31:1986-1998.

67. Patt M, Schildan A, Barthel H, et al. Metabolite analysis of [18F]Florbetaben (BAY 94-9172) in human subjects: a substudy within a proof of mechanism clinical trial. *J Radioanal Nucl Chem*. 2010;284:557-562.

68. Becker GA, Ichise M, Barthel H, et al. PET quantification of ^{18}F-florbetaben binding

to β-amyloid deposits in human brains. *J Nucl Med*. 2013;54:723-731.

69. Wang G, Nardo L, Parikh M, et al. Total-body PET multiparametric imaging of cancer using a voxel-wise strategy of compartmental modeling. *J Nucl Med*. 2022;63:1274-1281.

70. Muzi M, Spence AM, O'Sullivan F, et al. Kinetic analysis of 39-deoxy-39-18F-fluorothymidine in patients with gliomas. *J Nucl Med*. 2006;47:1612-1621.

71. Feng D, Huang S-C, Wang X. Models for computer simulation studies of input functions for tracer kinetic modeling with positron emission tomography. *Int J Biomed Comput*. 1993;32:95-110.

72. Carson RE. Tracer kinetic modeling in PET. In: Positron Emission Tomography. London: Springer; 2005:127-159.

73. Wood IS, Trayhurn P. Glucose transporters (GLUT and SGLT): expanded families of sugar transport proteins. *Br J Nutr*. 2003;89:3-9.

74. Pauwels EKJ, Ribeiro MJ, Stoot JHMB, McCready VR, Bourguignon M, Mazière B. FDG accumulation and tumor biology. *Nucl Med Biol*. 1998;25:317-322.

75. Marquardt DW. An algorithm for least-squares estimation of nonlinear parameters. *J Soc Ind Appl Math*. 1963;11:431-441.

76. Guobao Wang, Jinyi Qi. Generalized algorithms for direct reconstruction of parametric images from dynamic PET data. *IEEE Trans Med Imaging*. 2009;28:1717-1726.

77. Patlak CS, Blasberg RG, Fenstermacher JD. Graphical evaluation of blood-to-brain transfer constants from multiple-time uptake data. *J Cereb Blood Flow Metab*. 1983;3:1-7.

78. Cherry SR, Badawi RD, Karp JS, Moses WW, Price P, Jones T. Total-body imaging: Transforming the role of positron emission tomography. *Sci Transl Med*. 2017;9:eaaf6169.

79. Badawi RD, Shi H, Hu P, et al. First human imaging studies with the EXPLORER total-body PET scanner. *J Nucl Med*. 2019;60:299-303.

80. Zhang X, Cherry SR, Xie Z, Shi H, Badawi RD, Qi J. Subsecond total-body imaging using ultrasensitive positron emission tomography. *Proc Natl Acad Sci*. 2020;117:2265-2267.

81. West JB. Evolution of the pulmonary circulation and the right heart. In: Pulmonary

Circulation. CRC Press; 2016:22-30.

82. Suresh K, Shimoda LA. Lung Circulation. In: Terjung R, ed. Comprehensive Physiology. 1st ed. Hoboken: Wiley; 2016:897-943.

83. Deffebach ME, Charan NB, Lakshminarayan S, Butler J. The bronchial circulation. *Am Rev Respir Dis*. 1987;135:463-481.

84. Walker CM, Rosado-de-Christenson ML, Martínez-Jiménez S, Kunin JR, Wible BC. Bronchial arteries: Anatomy, function, hypertrophy, and anomalies. *Radiographics*. 2015;35:32-49.

85. McCullagh A, Rosenthal M, Wanner A, Hurtado A, Padley S, Bush A. The bronchial circulation—worth a closer look: A review of the relationship between the bronchial vasculature and airway inflammation. *Pediatr Pulmonol*. 2010;45:1-13.

86. Crook H, Raza S, Nowell J, Young M, Edison P. Long covid—mechanisms, risk factors, and management. *BMJ*. July 2021:374.

87. Zuo Y, Cherry SR, Badawi RD, Wang G. Multiphase Patlak plot enabled by high temporal resolution total-body dynamic PET. *J Nucl Med*. 2020;61:207.

88. Wang G, Sarkar S, Kim E, Badawi RD. Time-varying kinetic modeling of high temporal-resolution dynamic 18F-FDG PET data for multiparametric imaging. *J Nucl Med*. 2018;59:503.

89. Mitzner W, Lee W, Georgakopoulos D, Wagner E. Angiogenesis in the mouse lung. *Am J Pathol*. 2000;157:93-101.

90. Kiessling F, Boese J, Corvinus C, et al. Perfusion CT in patients with advanced bronchial carcinomas: a novel chance for characterization and treatment monitoring? *Eur Radiol*. 2004;14:1226-1233.

91. Yuan X, Zhang J, Ao G, Quan C, Tian Y, Li H. Lung cancer perfusion: Can we measure pulmonary and bronchial circulation simultaneously? *Eur Radiol*. 2012;22:1665-1671.

92. Zuo Y, Badawi RD, Foster CC, Smith T, Lopez JE, Wang G. Multiparametric cardiac ^{18}F-FDG PET in humans: Kinetic model selection and identifiability analysis. *IEEE Trans Radiat Plasma Med Sci*. 2020;4:759-767.

93. Wang G, Corwin MT, Olson KA, Badawi RD, Sarkar S. Dynamic PET of human liver inflammation: impact of kinetic modeling with optimization-derived dual-blood input function. *Phys Med Biol*. 2018;63:155004.

94. Gong K, Berg E, Cherry SR, Qi J. Machine learning in PET: From photon detection

to quantitative image reconstruction. *Proc IEEE*. 2020;108:51-68.

95. Ulyanov D, Vedaldi A, Lempitsky V. Deep image prior. 2018:9446-9454.

96. Akaike H. A new look at the statistical model identification. *IEEE Trans Autom Control*. 1974;19:716-723.

97. Wang B, Ruan D, Liu H. Noninvasive estimation of macro-parameters by deep learning. *IEEE Trans Radiat Plasma Med Sci*. 2020;4:684-695.

98. Xu J, Liu H. Deep-learning-based separation of a mixture of dual-tracer single-acquisition PET signals with equal half-lives: A simulation study. *IEEE Trans Radiat Plasma Med Sci*. 2019;3:649-659.

99. Pan L, Cheng C, Haberkorn U, Dimitrakopoulou-Strauss A. Machine learning-based kinetic modeling: a robust and reproducible solution for quantitative analysis of dynamic PET data. *Phys Med Biol*. 2017;62:3566-3581.

100. Strauss LG, Pan L, Cheng C, Haberkorn U, Dimitrakopoulou-Strauss A. Shortened acquisition protocols for the quantitative assessment of the 2-tissue-compartment model using dynamic PET/CT ^{18} F-FDG studies. *J Nucl Med*. 2011;52:379-385.

101. Liu L, Ding H, Huang HB. Improved simultaneous estimation of tracer kinetic models with artificial immune network based optimization method. *Appl Radiat Isot*. 2016;107:71-76.

102. Golish SR, Hove JD, Schelbert HR, Gambhir SS. A fast nonlinear method for parametric imaging of myocardial perfusion by dynamic 13N-ammonia PET. *J Nucl Med*. 2001;42:924-931.

103. Dimitrakopoulou-Strauss A, Hoffmann M, Bergner R, et al. Prediction of short-term survival in patients with advanced nonsmall cell lung cancer following chemotherapy based on 2-deoxy-2-[F-18]fluoro-d-glucose-Positron Emission Tomography: a feasibility study. *Mol Imaging Biol*. 2007;9:308-317.

104. de Prost N, Tucci MR, Melo MFV. Assessment of lung inflammation with ^{18}F-FDG PET during acute lung injury. *Am J Roentgenol*. 2010;195:292-300.

105. Rodrigues RS, Miller PR, Bozza FA, et al. FDG-PET in patients at risk for acute respiratory distress syndrome: a preliminary report. *Intensive Care Med*. 2008;34:2273-2278.

106. Castro M, Fain SB, Hoffman EA, Gierada DS, Erzurum SC, Wenzel S. Lung imaging in asthmatic patients: The picture is clearer. *J Allergy Clin Immunol*. 2011;128:467-478.

107. Chen DL, Schiebler ML, Goo JM, van Beek EJR. PET imaging approaches for inflammatory lung diseases: Current concepts and future directions. *Eur J Radiol*. 2017;86:371-376.

108. Fields BKK, Demirjian NL, Dadgar H, Gholamrezanezhad A. Imaging of COVID-19: CT, MRI, and PET. *Semin Nucl Med*. 2021;51:312-320.

109. Hellwig D, Graeter TP, Ukena D, et al. ^{18}F-FDG PET for mediastinal staging of lung cancer: Which SUV threshold makes sense? *J Nucl Med*. 2007;48:1761-1766.

110. Mullani NA, Herbst RS, O'Neil RG, Gould KL, Barron BJ, Abbruzzese JL. Tumor blood flow measured by PET dynamic imaging of first-pass ^{18}F-FDG uptake: A comparison with ^{15}O-labeled water-measured blood flow. *J Nucl Med*. 2008;49:517-523.

111. Laffon E, Calcagni ML, Galli G, et al. Comparison of three-parameter kinetic model analysis to standard Patlak's analysis in ^{18}F-FDG PET imaging of lung cancer patients. *EJNMMI Res*. 2018;8:1-8.

112. de Prost N, Feng Y, Wellman T, et al. ^{18}F-FDG kinetics parameters depend on the mechanism of injury in early experimental acute respiratory distress syndrome. *J Nucl Med*. 2014;55:1871-1877.

113. Chen DL, Cheriyan J, Chilvers ER, et al. Quantification of lung PET images: Challenges and opportunities. *J Nucl Med*. 2017;58:201-207.

114. Chen DL, Schuster DP. Positron emission tomography with [^{18}F]fluorodeoxyglucose to evaluate neutrophil kinetics during acute lung injury. *Am J Physiol-Lung Cell Mol Physiol*. 2004;286:L834-L840.

115. Wellman TJ, de Prost N, Tucci M, et al. Lung metabolic activation as an early biomarker of acute respiratory distress syndrome and local gene expression heterogeneity. *Anesthesiology*. 2016;125:992-1004.

116. Dimitrakopoulou-Strauss A, Georgoulias V, Eisenhut M, et al. Quantitative assessment of SSTR2 expression in patients with non-small cell lung cancer using ^{68}Ga-DOTATOC PET and comparison with ^{18}F-FDG PET. *Eur J Nucl Med Mol Imaging*. 2006;33:823-830.

117. Holman BF. Improving Quantification of PET/CT Biomarkers for Evaluation of Disease Progression and Treatment Effectiveness in Pulmonary Fibrosis. Ph.D. dissertation, University College London; 2016.

118. Surti S, Pantel AR, Karp JS. Total body PET: Why, how, what for? *IEEE Trans Radiat Plasma Med Sci*. 2020;4:283-292.

119. Nadig V, Herrmann K, Mottaghy FM, Schulz V. Hybrid total-body pet scanners—current status and future perspectives. *Eur J Nucl Med Mol Imaging*. 2022;49:445-459.

120. Zhang X, Cherry SR, Xie Z, Shi H, Badawi RD, Qi J. Subsecond total-body imaging using ultrasensitive positron emission tomography. *Proc Natl Acad Sci*. 2020;117:2265-2267.

121. Feng T, Zhao Y, Shi H, et al. Total-body quantitative parametric imaging of early kinetics of ^{18}F-FDG. *J Nucl Med*. 2021;62:738-744.

122. Li E, Spencer BA, Schmall JP, et al. Efficient delay correction for total-body PET kinetic modeling using pulse timing methods. *J Nucl Med*. 2022;63:1266-1273.

123. Iida H, Kanno I, Miura S, Murakami M, Takahashi K, Uemura K. Error analysis of a quantitative cerebral blood flow measurement using $H_2{}^{15}O$ autoradiography and Positron Emission Tomography, with respect to the dispersion of the input function. *J Cereb Blood Flow Metab*. 1986;6:536-545.

124. Meyer E. Simultaneous correction for tracer arrival delay and dispersion in CBF measurements by the $H_2{}^{15}O$ autoradiographic method and dynamic PET. *J Nucl Med*. 1989;30:1069-1078.

125. Chen DL, Mintun MA, Schuster DP. Comparison of methods to quantitate ^{18}F-FDG uptake with PET during experimental acute lung injury. *J Nucl Med*. 2004;45:1583-1590.

126. Holman BF, Cuplov V, Millner L, et al. Improved correction for the tissue fraction effect in lung PET/CT imaging. *Phys Med Biol*. 2015;60:7387-7402.

127. Schroeder T, Vidal Melo MF, Musch G, Harris RS, Venegas JG, Winkler T. Modeling pulmonary kinetics of 2-deoxy-2-[^{18}F]fluoro-d-glucose during acute lung injury. *Acad Radiol*. 2008;15:763-775.

128. Spencer BA, Berg E, Schmall JP, et al. Performance evaluation of the uEXPLORER total-body PET/CT scanner based on NEMA NU 2-2018 with additional tests to characterize PET scanners with a long axial field of view. *J Nucl Med*. 2021;62:861-870.

129. Leung EK, Berg E, Omidvari N, et al. Quantitative accuracy in total-body imaging using the uEXPLORER PET/CT scanner. *Phys Med Biol*. 2021;66:205008.

130. de Prost N, Costa EL, Wellman T, et al. Effects of surfactant depletion on regional pulmonary metabolic activity during mechanical ventilation. *J Appl Physiol*. 2011;111:1249-1258.

131. Schroeder T, Vidal Melo MF, Musch G, Harris RS, Venegas JG, Winkler T. Image-derived input function for assessment of ^{18}F-FDG uptake by the inflamed lung. *J Nucl Med*. 2007;48:1889-1896.

132. Thiele F, Buchert R. Evaluation of non-uniform weighting in non-linear regression for pharmacokinetic neuroreceptor modelling. *Nucl Med Commun*. 2008;29:179-188.

133. Akaike H. A new look at the statistical model identification. *IEEE Trans Autom Control*. 1974;19:716-723.

134. Glatting G, Kletting P, Reske SN, Hohl K, Ring C. Choosing the optimal fit function: Comparison of the Akaike information criterion and the F-test. *Med Phys*. 2007;34:4285-4292.

135. Carson RE, Yan Y, Daube-Witherspoon ME, Freedman N, Bacharach SL, Herscovitch P. An approximation formula for the variance of PET region-of-interest values. *IEEE Trans Med Imaging*. 1993;12:240-250.

136. Wu Y, Carson RE. Noise reduction in the simplified reference tissue model for neuroreceptor functional imaging. *J Cereb Blood Flow Metab*. 2002;22:1440-1452.

137. Zuo Y, Sarkar S, Corwin MT, Olson K, Badawi RD, Wang G. Structural and practical identifiability of dual-input kinetic modeling in dynamic PET of liver inflammation. *Phys Med Biol*. 2019;64:175023.

138. Georges R, Saumon G, Loiseau A. The relationship of age to pulmonary membrane conductance and capillary blood volume. *Am Rev Respir Dis*. 1978;117:1069-1078.

139. Chang S-C, Chang H-I, Liu S-Y, Shiao G-M, Perng R-P. Effects of body position and age on membrane diffusing capacity and pulmonary capillary blood volume. *Chest*. 1992;102:139-142.

140. Galvin I, Drummond GB, Nirmalan M. Distribution of blood flow and ventilation in the lung: gravity is not the only factor. *Br J Anaesth*. 2007;98:420-428.

141. Grecchi E, Veronese M, Moresco RM, et al. Quantification of dynamic [^{18}F]FDG PET studies in acute lung injury. *Mol Imaging Biol*. 2016;18:143-152.

142. Hunter CRRN, Klein R, Beanlands RS, deKemp RA. Patient motion effects on the quantification of regional myocardial blood flow with dynamic PET imaging. *Med Phys*. 2016;43:1829-1840.

143. Coello C, Fisk M, Mohan D, et al. Quantitative analysis of dynamic ^{18}F-FDG PET/CT for measurement of lung inflammation. *EJNMMI Res*. 2017;7:1-12.

144. Nguyen-Kim TDL, Frauenfelder T, Strobel K, Veit-Haibach P, Huellner MW. Assessment of bronchial and pulmonary blood supply in non-small cell lung cancer subtypes using computed tomography perfusion. *Invest Radiol*. 2015;50:179-186.

145. Yuan X, Zhang J, Quan C, et al. Differentiation of malignant and benign pulmonary nodules with first-pass dual-input perfusion CT. *Eur Radiol*. 2013;23:2469-2474.

146. Chen X, Xu Y, Duan J, Li C, Sun H, Wang W. Correlation of iodine uptake and perfusion parameters between dual-energy CT imaging and first-pass dual-input perfusion CT in lung cancer. *Medicine (Baltimore)*. 2017;96:e7479.

147. Alberts I, Hünermund J-N, Prenosil G, et al. Clinical performance of long axial field of view PET/CT: a head-to-head intra-individual comparison of the Biograph Vision Quadra with the Biograph Vision PET/CT. *Eur J Nucl Med Mol Imaging*. 2021;48:2395-2404.

148. Pantel AR, Viswanath V, Daube-Witherspoon ME, et al. PennPET Explorer: Human imaging on a whole-body imager. *J Nucl Med*. 2020;61:144-151.

149. Wang Y, Spencer BA, Schmall J, et al. High-temporal-resolution lung kinetic modeling using total-body dynamic PET with time-delay and dispersion corrections. *J Nucl Med*. 2023;64:1154-1161.

150. Torizuka T, Nobezawa S, Momiki S, et al. Short dynamic FDG-PET imaging protocol for patients with lung cancer. *Eur J Nucl Med*. 2000;27:1538-1542.

151. Glatting G, Kletting P, Reske SN, Hohl K, Ring C. Choosing the optimal fit function: Comparison of the Akaike information criterion and the F-test: Choosing the optimal fit function. *Med Phys*. 2007;34:4285-4292.

152. Li EJ, López JE, Spencer BA, et al. Total-body perfusion imaging with [^{11}C]-Butanol. *J Nucl Med*. 2023;64:1831-1838.

153. Jeffery PK. Remodeling in asthma and chronic obstructive lung disease. *Am J Respir Crit Care Med*. 2001;164:S28-S38.

154. Ackermann M, Tafforeau P, Wagner WL, et al. The Bronchial Circulation in COVID-19 Pneumonia. *Am J Respir Crit Care Med*. 2022;205:121-125.

155. Keiding S. Bringing physiology into PET of the liver. *J Nucl Med*. 2012;53:425-433.

156. Wang Y, Li E, Cherry SR, Wang G. Total-body PET kinetic modeling and potential opportunities using deep learning. *PET Clin*. 2021;16:613-625.

157. Sundaram SM, Doughty LA, Sereda MW. Location matters: Hexokinase 1 in glucose

metabolism and inflammation. *Trends Endocrinol Metab*. 2022;33:665-667.

158. Zerizer I, Tan K, Khan S, et al. Role of FDG-PET and PET/CT in the diagnosis and management of vasculitis. *Eur J Radiol*. 2010;73:504-509.

159. Wenter V, Müller J-P, Albert NL, et al. The diagnostic value of [^{18}F]FDG PET for the detection of chronic osteomyelitis and implant-associated infection. *Eur J Nucl Med Mol Imaging*. 2016;43:749-761.

160. Zou S, Zhu X. FDG PET/CT of COVID-19. *Radiology*. 2020;296:E118-E118.

161. Afshar-Oromieh A, Prosch H, Schaefer-Prokop C, et al. A comprehensive review of imaging findings in COVID-19 - status in early 2021. *Eur J Nucl Med Mol Imaging*. 2021;48:2500-2524.

162. Dietz M, Chironi G, Claessens Y-E, et al. COVID-19 pneumonia: relationship between inflammation assessed by whole-body FDG PET/CT and short-term clinical outcome. *Eur J Nucl Med Mol Imaging*. 2021;48:260-268.

163. Hu B, Guo H, Zhou P, Shi Z-L. Characteristics of SARS-CoV-2 and COVID-19. *Nat Rev Microbiol*. 2021;19:141-154.

164. Soltani Zangbar H, Gorji A, Ghadiri T. A review on the neurological manifestations of COVID-19 infection: A mechanistic view. *Mol Neurobiol*. 2021;58:536-549.

165. Zaim S, Chong JH, Sankaranarayanan V, Harky A. COVID-19 and multiorgan response. *Curr Probl Cardiol*. 2020;45:100618.

166. Yazdanpanah F, Hamblin MR, Rezaei N. The immune system and COVID-19: Friend or foe? *Life Sci*. 2020;256:117900.

167. Guedj E, Campion JY, Dudouet P, et al. ^{18}F-FDG brain PET hypometabolism in patients with long COVID. *Eur J Nucl Med Mol Imaging*. 2021;48:2823-2833.

168. Sollini M, Morbelli S, Ciccarelli M, et al. Long COVID hallmarks on [18F]FDG-PET/CT: a case-control study. *Eur J Nucl Med Mol Imaging*. 2021;48:3187-3197.

169. Sollini M, Ciccarelli M, Cecconi M, et al. Vasculitis changes in COVID-19 survivors with persistent symptoms: an [^{18}F]FDG-PET/CT study. *Eur J Nucl Med Mol Imaging*. 2021;48:1460-1466.

170. Thiele F, Buchert R. Evaluation of non-uniform weighting in non-linear regression for pharmacokinetic neuroreceptor modelling. *Nucl Med Commun*. 2008;29:179-188.

171. McIntosh LJ, Bankier AA, Vijayaraghavan GR, Licho R, Rosen MP. COVID-19 vaccination-related uptake on FDG PET/CT: An emerging dilemma and suggestions

for management. *Am J Roentgenol*. 2021;217:975-983.

172. Keshavarz P, Yazdanpanah F, Rafiee F, Mizandari M. Lymphadenopathy following COVID-19 vaccination: Imaging findings review. *Acad Radiol*. 2021;28:1058-1071.

173. Wellman TJ, Winkler T, Costa ELV, et al. Effect of local tidal lung strain on inflammation in normal and lipopolysaccharide-exposed sheep. *Crit Care Med*. 2014;42:e491-e500.

174. Subramanian DR, Jenkins L, Edgar R, Quraishi N, Stockley RA, Parr DG. Assessment of pulmonary neutrophilic inflammation in emphysema by quantitative Positron Emission Tomography. *Am J Respir Crit Care Med*. 2012;186:1125-1132.

175. Doykov I, Hällqvist J, Gilmour KC, Grandjean L, Mills K, Heywood WE. 'The long tail of Covid-19' - The detection of a prolonged inflammatory response after a SARS-CoV-2 infection in asymptomatic and mildly affected patients. *F1000Research*. 2020:1-9.

176. Albano D, Bertagna F, Bertoli M, et al. Incidental findings suggestive of COVID-19 in asymptomatic patients undergoing nuclear medicine procedures in a high-prevalence region. *J Nucl Med*. 2020;61:632-636.

177. Zuo Y, Yalavarthi S, Shi H, et al. Neutrophil extracellular traps in COVID-19. *JCI Insight*. April 2020.

178. Chen DL, Agapov E, Wu K, et al. Selective imaging of lung macrophages using [^{11}C]PBR28-based Positron Emission Tomography. *Mol Imaging Biol*. 2021;23:905-913.

179. McGonagle D, Sharif K, O'Regan A, Bridgewood C. The role of cytokines including interleukin-6 in COVID-19 induced pneumonia and macrophage activation syndrome-like disease. *Autoimmun Rev*. 2020;19:102537.

180. Zhao E, Xu H, Wang L, et al. Bone marrow and the control of immunity. *Cell Mol Immunol*. 2012;9:11-19.

181. Rojas M, Xu J, Woods CR, et al. Bone marrow–derived mesenchymal stem cells in repair of the injured lung. *Am J Respir Cell Mol Biol*. 2005;33:145-152.

182. Yamada M, Kubo H, Kobayashi S, et al. Bone marrow-derived progenitor cells are important for lung repair after lipopolysaccharide-induced lung injury. *J Immunol*. 2004;172:1266-1272.

183. Sarkar S, Corwin MT, Olson KA, et al. Pilot study to diagnose nonalcoholic steatohepatitis with dynamic ^{18}F-FDG PET. *Am J Roentgenol*. 2019;212:529-537.

184. Liu Y. Clinical significance of diffusely increased splenic uptake on FDG-PET. *Nucl Med Commun*. 2009;30:763-769.

185. Kaneko N, Kuo H-H, Boucau J, et al. Loss of Bcl-6-expressing T follicular helper cells and germinal centers in COVID-19. *Cell*. 2020;183:143-157.e13.

186. Wang Y, Spencer BA, Schmall J, et al. High-temporal-resolution lung kinetic modeling using total-body dynamic PET with time-delay and dispersion corrections. *J Nucl Med*. April 2023:jnumed.122.264810.

187. Kim EJ, Kim S, Seo HS, et al. Novel PET imaging of atherosclerosis with ^{68} Ga-labeled NOTA-neomannosylated human serum albumin. *J Nucl Med*. 2016;57:1792-1797.

188. Antoni G, Lubberink M, Sörensen J, et al. In vivo visualization and quantification of neutrophil elastase in lungs of COVID-19 patients: A first-in-humans PET study with ^{11}C-NES. *J Nucl Med*. 2023;64:145-148.

189. Tian C, Fei L, Zheng W, Xu Y, Zuo W, Lin C-W. Deep learning on image denoising: An overview. *Neural Netw*. 2020;131:251-275.

190. Golla SSV, Adriaanse SM, Yaqub M, et al. Model selection criteria for dynamic brain PET studies. *EJNMMI Phys*. 2017;4:1-10.

191. Sugiura N. Further analysts of the data by akaike' s information criterion and the finite corrections: Further analysts of the data by akaike' s. *Commun Stat - Theory Methods*. 1978;7:13-26.

192. LeCun Y, Bengio Y, Hinton G. Deep learning. *Nature*. 2015;521:436-444.

193. Anderson D, Burnham KP. Information and Likelihood Theory: A Basis for Model Selection and Inference. In: Model Selection and Multi-Model Inference. Vol 2020. 2nd ed. 63. Springer-Verlag; 2004:49-97.

194. Anderson D, Burnham KP. Advanced Issues and Deeper Insights. In: Model Selection and Multi-Model Inference. Vol 2020. 2nd ed. 63. Springer-Verlag; 2004:267-351.

195. Dice LR. Measures of the Amount of Ecologic Association Between Species. *Ecology*. 1945;26:297-302.

196. Grandini M, Bagli E, Visani G. Metrics for Multi-Class Classification: an Overview. August 2020.

197. Wagenmakers E-J, Farrell S. AIC model selection using Akaike weights. *Psychon Bull Rev*. 2004;11:192-196.

198. Zuo Y, López JE, Smith TW, et al. Multiparametric cardiac ^{18} F-FDG PET in humans: pilot comparison of FDG delivery rate with ^{82} Rb myocardial blood flow. *Phys Med Biol*. 2021;66:155015.

199. Tran Q, Lyo V, Matsukuma K, et al. Total-body PET quantification of metabolism in non-alcoholic steatohepatitis using a three-tissue compartment model. *J Nucl Med*. 2023;64:1388.

200. Wang G, Sarkar S, Kim E, Badawi RD. Time-Varying Kinetic Modeling of High Temporal-Resolution Dynamic 18F-FDG PET Data for Multiparametric Imaging. *J Nucl Med*. 2018;59:503.

201. Garbarino S, Vivaldi V, Delbary F, et al. A new compartmental method for the analysis of liver FDG kinetics in small animal models. *EJNMMI Res*. 2015;5:35.

202. Kletting P, Bunjes D, Reske SN, Glatting G. Improving anti-CD45 antibody radioimmunotherapy using a physiologically based pharmacokinetic model. *J Nucl Med*. 2009;50:296-302.

203. Kletting P, Kull T, Maaß C, et al. Optimized peptide amount and activity for ^{90} Y-labeled DOTATATE therapy. *J Nucl Med*. 2016;57:503-508.

204. Kletting P, Thieme A, Eberhardt N, et al. Modeling and predicting tumor response in radioligand therapy. *J Nucl Med*. 2019;60:65-70.

205. Li E. Kinetic modeling methods for the measurement of glucose metabolism and blood flow with total-body PET. University of California, Davis; 2022.

206. Sundar LKS, Yu J, Muzik O, et al. Fully automated, semantic segmentation of whole-body ^{18} F-FDG PET/CT images based on data-centric artificial intelligence. *J Nucl Med*. 2022;63:1941-1948.

207. Selfridge AR, Spencer BA, Abdelhafez YG, Nakagawa K, Tupin JD, Badawi RD. Facial anonymization and privacy concerns in total-body PET/CT. *J Nucl Med*. 2023;64:1304-1309.

208. Wu J, Liu H, Ye Q, et al. Generation of parametric K_{i} images for FDG PET using two 5-min scans. *Med Phys*. 2021;48:5219-5231.

209. Wu Y, Feng T, Zhao Y, et al. Whole-Body parametric imaging of ^{18}F-FDG PET using uEXPLORER with reduced scanning time. *J Nucl Med*. 2022;63:622-628.

210. Kratochwil C, Flechsig P, Lindner T, et al. ^{68} Ga-FAPI PET/CT: Tracer uptake in 28 different kinds of cancer. *J Nucl Med*. 2019;60:801-805.

211. Chen R, Yang X, Ng YL, et al. First total-body kinetic modeling and parametric imaging of dynamic ^{68} Ga-FAPI-04 PET in pancreatic and gastric cancer. *J Nucl Med*. 2023;64:960-967.

212. OpenAI. GPT-4 technical report. 2023.

213. Liu P, Yuan W, Fu J, Jiang Z, Hayashi H, Neubig G. Pre-train, prompt, and predict: A systematic survey of prompting methods in natural language processing. *ACM Comput Surv*. 2023;55:1-35.

214. Liu Z, Zhong A, Li Y, et al. Radiology-GPT: A large language model for radiology. June 2023.